Synchrotron x-ray diffraction studies of phase transitions and mechanical properties of nanocrystalline materials at high pressure

by

Stephen Gerald Prilliman

B.A. (Rice University) 1998

A dissertation submitted in partial satisfaction of the
requirements for the degree of
Doctor of Philosophy

in

Chemistry

in the

GRADUATE DIVISION
of the
UNIVERSITY OF CALIFORNIA, BERKELEY

Committee in charge:
Professor A. Paul Alivisatos, Chair
Professor Gabor Somorjai
Professor Raymond Jeanloz

Fall 2003

The dissertation of Stephen Gerald Prilliman is approved:

_____

Chair   Date

_____

Date

_____

Date

University of California, Berkeley

Fall 2003

Synchrotron x-ray diffraction studies of phase transitions and mechanical properties of nanocrystalline materials at high pressure

Copyright 2003

by

Stephen Gerald Prilliman

Abstract

Synchrotron x-ray diffraction studies of phase transitions and mechanical properties

of nanocrystalline materials at high pressure

by

Stephen Gerald Prilliman

Doctor of Philosophy in Chemistry

University of California, Berkeley

Professor A. Paul Alivisatos, Chair

The behavior of nanocrystals under extreme pressure was investigated using synchrotron x-ray diffraction. A major part of this investigation was the testing of a prototype synchrotron endstation on a bend magnet beamline at the Advanced Light Source for high pressure work using a diamond anvil cell. The experiments conducted and documented here helped to determine issues of efficiency and accuracy that had to be resolved before the construction of a dedicated "super-bend" beamline and endstation. The major conclusions were the need for a cryo-cooled monochromator and a fully remote-controllable pressurization system which would decrease the time to change pressure and greatly reduce the error created by the re-placement of the diamond anvil cell after each pressure change.

Two very different types of nanocrystal systems were studied, colloidal iron oxide (Fe_2O_3) and thin film TiN/BN. Iron oxide nanocrystals were found to have a transition from the γ to the α structure at a pressure strongly dependent on the size of the nanocrystals, ranging from 26 GPa for 7.2 nm nanocrystals to 37 GPa for 3.6 nm nanocrystals. All nanocrystals were found to remain in the α structure even after release of pressure. The transition pressure was also found, for a constant size (5.7 nm) to be strongly dependent on the degree of aggregation of the nanocrystals, increasing from 30 GPa for completely dissolved nanocrystals to 45 GPa for strongly aggregated nanocrystals. Furthermore, the x-ray diffraction pattern of the pressure induced α phase demonstrated a decrease in intensity for certain select peaks. Together, these observations were used to make a complete picture of the phase transition in nanocrystalline systems. The size dependence of the transition was interpreted as resulting from the extremely high surface energy of the α phase which would increase the thermodynamic offset and thereby increase the kinetic barrier to transition that must be overridden with pressure. The anomalous intensities in the x-ray diffraction patterns were interpreted as being the result of stacking faults, indicating that the mechanism of transition proceeds by the sliding of γ (111) planes to form α (001) planes. The increasing transition pressure for more aggregated samples may be due to a positive activation volume, retarding the transition for nanocrystals with less excess (organic) volume available to them. The lack of a reverse transition upon decompression makes this interpretation more difficult because of the lack of an observable hysteresis, and

it is therefore difficult to ascertain kinetic effects for certain.

In the case TiN/BN nanocomposite systems, it was found that the bulk modulus (B_0) of the TiN nanoparticles was not correlated to the observed hardness or Young's modulus of the macroscopic thin film. This indicates that the origin of the observed super-hard nature of these materials is not due to any change in the Ti-N interatomic potential. Rather, the enhanced hardness must be due to nano-structural effects. It was also found that during pressurization the TiN nanoparticles developed a great deal of strain. This strain can be related to defects induced in individual nanoparticles which generates strain in adjacent particles due to the highly coupled nature of the system.

Professor A. Paul Alivisatos
Dissertation Committee Chair

This work is dedicated to my parents, Gerald and Helen. I am who I

am today because of them.

"For He gave me sound knowledge of existing things, that I might know the organizaiton of the universe and the force of its elements."

The Book of Wisdom, 7:17

Contents

List of Figures

List of Tables

Acknowledgments

The completion of a dissertation is the work of many people, not just the author. Here I wish to express my thanks to a few of those people.

I wish to thank my colleagues in the Alivisatos group. Juanita Wickham, C. J. Lee, Keren Jacobs, Kim Hamad and Joerg Rockenberger were my first teachers in graduate school, and answered many stupid questions, often with a straight face. Thanks to my peers Erik Scher and David Zaziski; together we survived courses, quals, and post-qual slumps, while doing some research along the way. Special thanks go to the "Science League", Benjamin Boussert, Christine Micheel, Deborah Aruguete, Delia Milliron, and Steven Robertson (C. B. Harris Lab) for many engaging discussions over coffee about science and life. In my worst times in graduate school, they were my best friends. Can Erdonmez has put up with precious little instruction while trying to solve my most difficult scientific questions. His frequent willingness to take the "Istanbul shift" during beamtime was also greatly appreciated. Jacqueline Kwong was my student and research assistant for several years, and I hope she learned as much from me as I did from her. Erik, Joerg, and Christine also receive thanks for doing TEM. Thanks to Rita Tidwell, our administrative assistant, for making things work and for sorting out many problems, most of my own creation. Of course, I wish to thank my advisor, Paul Alivisatos, for his guidance and advice, and for allowing me to follow my own research path, even when that path was slow and winding.

Thanks go to everyone at the Advanced Light Source who made all the work there

Chapter 1

Introduction: Nanocrystals at high pressure

1.1   Introduction to nanoscience

In everyday experience, the properties of a material do not depend on the size of the material. Gold is yellow and reflective whether it is a gold ring or a gold necklace or a thin gold flake. However, if one were to observe increasingly smaller pieces of gold, this trend would have to end. Ultimately, only a single atom of gold would remain. This single gold atom would be neither yellow nor shinny – it would exhibit sharp, atomic absorption and would not reflect light. But at what point does this breakdown occur? What properties would two gold atoms have, or a hundred, or a thousand?

There is in fact a transition zone, somewhere between 100–10,000 atoms in which gold particles behave neither like single atoms nor quite like macroscopic, bulk gold. Gold particles in this size regime are neither reflective nor yellow in color, but look red or orange in solution as seen in Figure 1.1. Such particles with dimensions on the scale of 1–100 nanometers (nm) are the focus of the study of nanoscience, and these particles are refered to as nanocrystals [1, 2]. For nanocrystals, phenomena become important that are overwhelmed in the bulk by the sheer size of the particle relative to the size of a single atom. In nanocrystal systems, surface atoms constitute a large portion of the total atoms, hence the surface energy makes an important contribution to the thermodynamic properties. Quantum mechanical effects like the "particle in a box" cause the energy of conduction electrons to be elevated, leading to the blue-shifting of absorption in nanoscale semiconductors. Bulk gold has its yellow luster because large numbers of electrons move synchronously when they interact with the electric field of visible light. However, nanometer sized gold particles, due to their finite size, have fewer electrons than would normally interact with the light. This causes the refractive index to be size dependent, and the refractive index determines the color and luster of the sample. The size dependence of the color of nano-scale gold can be seen in Figure 1.1.

The interplay of various nano-scale effects causes the properites of a nanocrystal to depend on the exact nature of the system — its composition, size, shape, crystallographic structure, surface state and surface passivation. Thus, nanocrystals can be
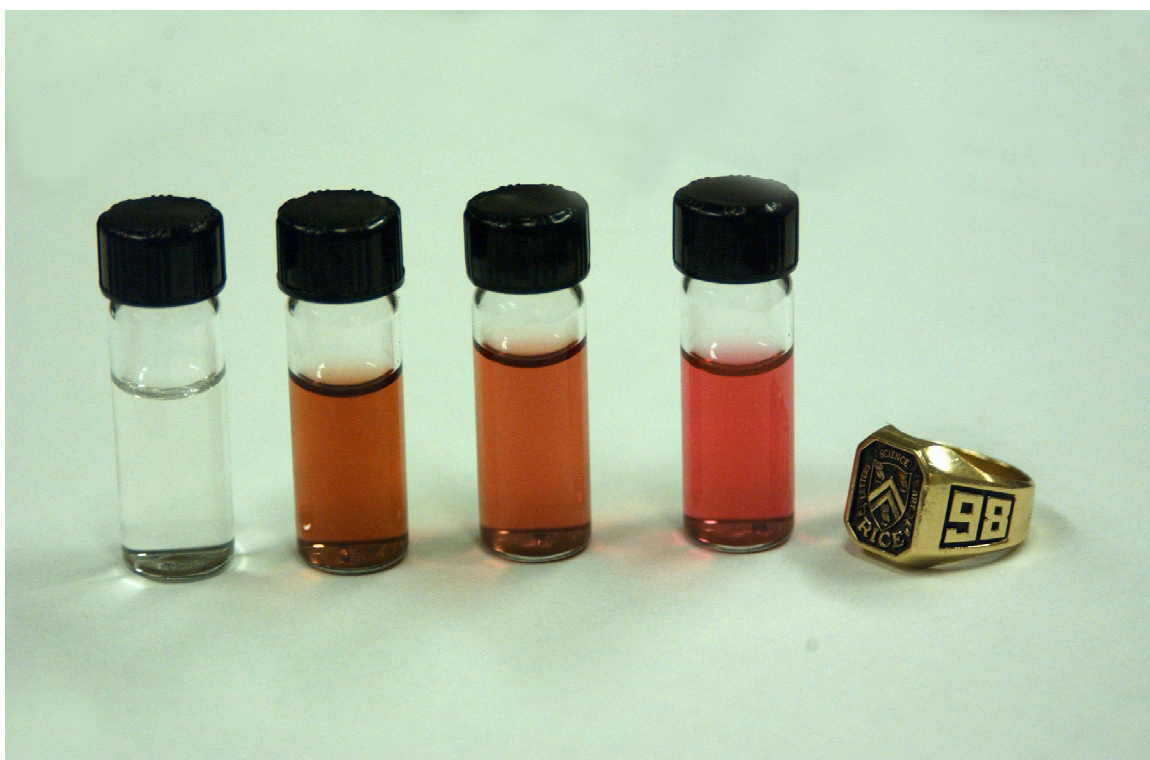
Figure 1.1: A size series of gold nanoparticles. From left to right, 2 nm, 5 nm, 10 nm and 50 nm. At far right is the ultimate end, bulk gold.

created in such a way as to have tunable properties. This is a novelty in chemistry —
the properties of a material no longer depend solely upon the chemical formula. The
underlying chemical nature of the material is still important and sets boundaries on
the possible observed properties, but changing a particle's dimensions on the nanome-
ter scale provides new ways to control and tune the material's properties. The goal of
nanoscience is to understand the forces which produce these properties, and to learn
how to rationally synthesize new materials with novel properties.

1.2   Overview

In order to gain a better understanding of nanoscale materials, one must system-
atically change the conditions under which the material is studied. This work deals
with the properties of nanoscale systems under the influence of a single variable, pres-
sure. The observable properties, structural transitions and mechanical response or
bulk modulus, require extremely high pressures to be observable. In order to generate
sufficiently high pressures, a devise is used called a diamond anvil cell (DAC) in which
opposing diamonds are brought together to create pressures of 10,000 to 1,000,000
times atmospheric pressure or higher. The diamonds themselves, then, must be pen-
etrated to observe the system under pressure. The usual way to do this is to use a
spectroscopic technique involving a wavelength which the diamonds do not absorb.
Because in this case we wish to study structural properties, this requires the use of
x-ray diffraction (XRD). However, diamonds are only partially transparent to very

high energy ("hard") x-rays of energy > 10 keV (wavelength, $\lambda < 1.24$ Å). In order to achieve x-rays of both sufficiently high energy ($h\nu$) and power (number of photons), a synchrotron source is necessary. Synchrotrons are high energy particle accelerator rings which produce high energy x-rays in great quantity.

This work brings together three techniques — nanocrystal synthesis, high pressure, and synchrotron x-ray diffraction — to execute a study of the high pressure properties of nano-scale systems. The first system studied is iron oxide colloidal nanocrystals. When subjected to pressure, these nanocrystals undergo a structural phase transition from the initial γ structure to the α structure. Nanocrystals with diameter between 3.2 and 7.2 nm were observed up to pressures of 50 gigapascals (GPa). The transition pressure was observed to depend on size, with small nanocrystals transforming at a higher pressure. The transition pressure was also found to depend on the aggregation state of the nanocrystals. Increasingly aggregated nanocrystals transformed at higher pressures. The exact structure of the α phase was found to be defective with respect to the ideal structure. The defect seemingly stems from either the displacement of iron atoms within the oxygen lattice or stacking faults of the oxygen layers themselves.

An entirely different type of nano-scale system was also observed, that of titanium nitride/silicon nitride (TiN/Si_3N_4 and TiN/BN) nano-composite materials. These are solid films with nanometer scale TiN particles separated by a thin layer of silicon nitride or boron nitride. They are found to have unusually high hardness, approaching that of diamond. Samples of these nano-composites were observed under hydrostatic

pressures up to 50 GPa in order to determine the bulk modulus independently of other moduli. The bulk modulus of the TiN nanocrystals was found to be nearly that of the bulk TiN. However, a great deal of stress, both isotropic and anisotropic, was also observed in these materials. These observations imply that defects are created within individual nanocrystals. These defects propagate strain throughout the thin film.

The structure of this work is as follows: This chapter seeks to outline the work and provides general background to the scientific motivations and the techniques necessary to execute the experiments. Chapter 2 describes the experimental methods used throughout the work. Chapter 3 describes the work undertaken to craft a beamline at the Advanced Light Source (ALS) which would be designed to study nanocrystals under pressure. Chapters 4, 6 and 7 describe work done at the prototype ALS beamline on structural transitions in iron oxide nanocrystals. Chapter 5 concerns the mechanical properties of titanium nitride/silicon nitride nanocomposites under high pressure.

1.3 Nanocrystals at high pressures

1.3.1 Nanocrystals as model systems for high pressure studies

Basic crystallography is based on the assumption that all atoms lie in their hypothetical lattice positions in all directions for an infinite distance. This is, of course, a gross oversimplification. Many different types of defects, from point defects like missing atoms or atoms in the wrong position, to line defects like grain boundaries, mean that atoms do not occupy the idealized positions. Strains may also be present which makes the idealized lattice less and less applicable as one proceeds away from a reference point. These are not merely abstract considerations. The presence of defects has a real and observable effect on the material's high pressure properties (phase transition pressure, conductivity, compressibility, etc.). The first step in most high pressure studies of bulk materials is to anneal samples so as to make these assumptions more true. However, defects can develop during an experiment. A phase transition nucleates at a point and propagates outward, generating increasingly larger strain at the phase boundary. This strain is relieved by fracture, which generates either a twin defect or a grain boundary. A second pressure cycling of this sample will result in a different observed transition pressure as transitions can more easily nucleate at the newly created defects. The presence of defects in bulk solids makes the study of their high pressure behavior quite difficult.

However, a model system may exist in colloidal nanocrystals. Colloidal nanocrystals have a number of properties which make them superb model systems for the study of high pressure phenomena. The foremost reason is that colloidal nanocrystals can be synthesized nearly defect free. This is true for a number of reasons. First, the nanocrystals are grown under solution conditions which allow for nearly epitaxial growth at the surface. Also, at the very high temperatures ($> 250^{\circ}$C) at which the nanocrystals are grown, individual atoms may bind to the surface and then redissolve. Only the most strongly bound atoms will remain at the surface, virtually guaranteeing each atom will be in its energetically minimum position. Second, if defects do form, they will have a moderately high mobility because of the high thermal energy. More importantly, a defect need not defuse very far to reach the surface of the nanocrystal. Typical diffusion rates in solids are on the order of 1 Å/s [3], and thus all defects will reach the surface of a 10 nm nanocrystal in a 100 second synthesis. Defects in nanocrystals are so "volatile" that it is difficult to produce desirable defects, for example n- or p-doping in semiconductors [4].

Experimental evidence verifies the defect free nature of nanocrystals. The sizes obtained from transmission electron microscopy (TEM) and x-ray diffraction (XRD) are very close for colloidal nanocrystals, indicating that they are single domain particles. Also, simulations of x-ray diffraction data [5] indicate that 4.5 nm CdSe colloidal nanocrystals have on average two stacking faults per nanocrystal. The energy cost for a stacking fault in the wurtzite structure is extremely small, indicative of the near

perfection of crystallinity in colloidal nanocrystals.

In addition, the finite volume of nanocrystals prevents them from fracturing into multiple domains during structural phase transitions (below a critical threshold [6]). The phase boundary reaches the surface of the nanocrystals before sufficient strain is built up to cause a domain fracture. This creates a great simplification in the study of structural transitions. Repeated pressure cycles will yield the same transition pressure each time [7]. Also, the kinetics of the phase transition become first order and can be studied directly [8] [9] to obtain the activation energy and activation volume. These in turn provide information about the transition state and the mechanism of transition.

Colloidally prepared nanocrystals have yet another property making them a model system. These nanocrystals are prepared chemically rather than mechanically (e.g., ball milling) and retain a monolayer of the surfactant in which they are grown. This shell of surfactant serves several useful purposes. It coordinates to the surface atoms, saturating any "dangling" bonds. The surfactant shell, at least partially, reduces oxidation [10]. Most importantly in this case, the surfactant shell, with it's hydrophobic tail pointed outward, confers to the nanocrystal solubility in non-polar solvents (e.g., hexane, toluene). This allows the nanocrystals to be *chemically dissolved* in the pressure medium. These nanocrystals are isolated from one another, first within their surfactant shells, then within the solvation shell of the medium. This isolation prevent the behavior of one nanocrystal from influencing that of neighboring nanocrystals. This proves important, as is seen in the present work (Chapter 6) where the aggre-

gation state of the nanocrystal was found to strongly influence the phase transition pressure.

1.3.2 New physics observed in nanocrystals under pressure

Size dependence of phase transition

In addition to their viability as a model system, nanocrystals provide the opportunity to study phenomena not observed in bulk systems. The most well studied and understood of these phenomena is the size dependence of the structural transition pressure. Nanocrystals of CdSe [11, 12], InP [7], and PbS [13] have demonstrated similar effects. The transition pressure increases strongly as size decreases with a $1/r^2$ dependence. (Nanocrystals of ZnO [14] and Si [15] have been shown to transform at pressures higher than that of bulk but the size depedence has not been established.) This size dependence in transition pressure is due to the surface energy contribution to the relative thermodynamic stability of the two phases. The surface energy of rock-salt CdSe nanocrystals is much higher than that of wurtzite phase nanocrystals. This means that more pressure must be used to overcome the increased thermodynamic offset due to surface energy.

Nanocrystalline compressibility

One of the properties of a system often studied under high pressure is the compressibility, or how easily the volume decreases when a given pressure is applied. The

compressibility is an indication of the strength of the chemical bonds in the materials. The hydrostatic compressibility, κ, is defined by:

$$\kappa = -\frac{1}{V}\left(\frac{dV}{dP}\right)$$

where V is the volume and P is the pressure. Alternatively, the bulk modulus, B $=$ $1/\kappa$, can be calculated, as is more common in the literature [1].

Because the compressibility is a function of pressure, the compressibility at ambient pressure, $\kappa_0 = 1/B_0$, is generally determined by fitting the curve of volume as a function of pressure to the first order Birch-Murnagham [16] equation of state.

$$P = \frac{1.5}{B_0}\left[\left(\frac{V_0}{V}\right)^{\frac{7}{3}} - \left(\frac{V_0}{V}\right)^{\frac{5}{3}}\right]$$

Here P is the pressure at which V will be observed, given the volume at ambient pressure, V_0 , and the bulk modulus at ambient pressure, B_0. Typical values of B_0 are tens to several hundred GPa.

Nanocrystals are observed to have interesting compressibility behavior. While CdSe does not show a measurable difference in compressibility between bulk and nanocrstals [12], studies of metal oxide nanocrystalline systems have shown a drastic difference in compressibility compared to their bulk counterparts. Nanocrystalline Al_2O_3 has shown a size dependent increase in compressibility relative to the bulk [17].

---

[1] The language in these studies can become difficult. Most studies refer to the bulk modulus, B (as distinct from the sheer and Young's modulus). However, this is very confusing when comparing the values of B for nanocrystalline and bulk materials. Throughout this work, I will refer to the compressibility (1/B) of a material, but for ease of comparison with the literature, whenever I wish to quantify it, it will be given as the value of B.

Nanocrystals of γ-Fe$_2$O$_3$ [18], rutile-TiO$_2$ [19], and CeO$_2$ [20] all show a strong decrease in compressibility, up to 100% in the case of γ-Fe$_2$O$_3$. Two other systems, CuO and SiO$_2$ [21] show no observable difference in compressibility between nanocrystals and bulk. No trend or proper explanation has yet been determined in these systems. However, the apparent pervasiveness of the phenomenon means that it deserves further study, both experimentally and theoretically. This work will attempt to shed additional light on the of Fe$_2$O$_3$ system (see Chapter 4). Also, in Chapter 5, the compressibility of TiN nano-composites are investigated to determine if their extreme hardness is due to a change in compressibility or if it is due to some other property of the material.

1.4   High pressure studies

1.4.1   Motivation for high pressure science

Pressure is a variable of interest in a wide variety of scientific inquiries. The full range of pressures a scientist might wish to study is shown in Figure 1.2. Those pressures below atmospheric pressure can be reached using various pumps and vacuum techniques noted on the figure. However, reaching pressures well above atmospheric pressure was very difficult until the advent of the diamond anvil cell which allows coverage of pressures from 10^3 and 1×10^6 bar. With a (relatively) simple technique which could access extremely high pressures, it becomes possible to reproduce
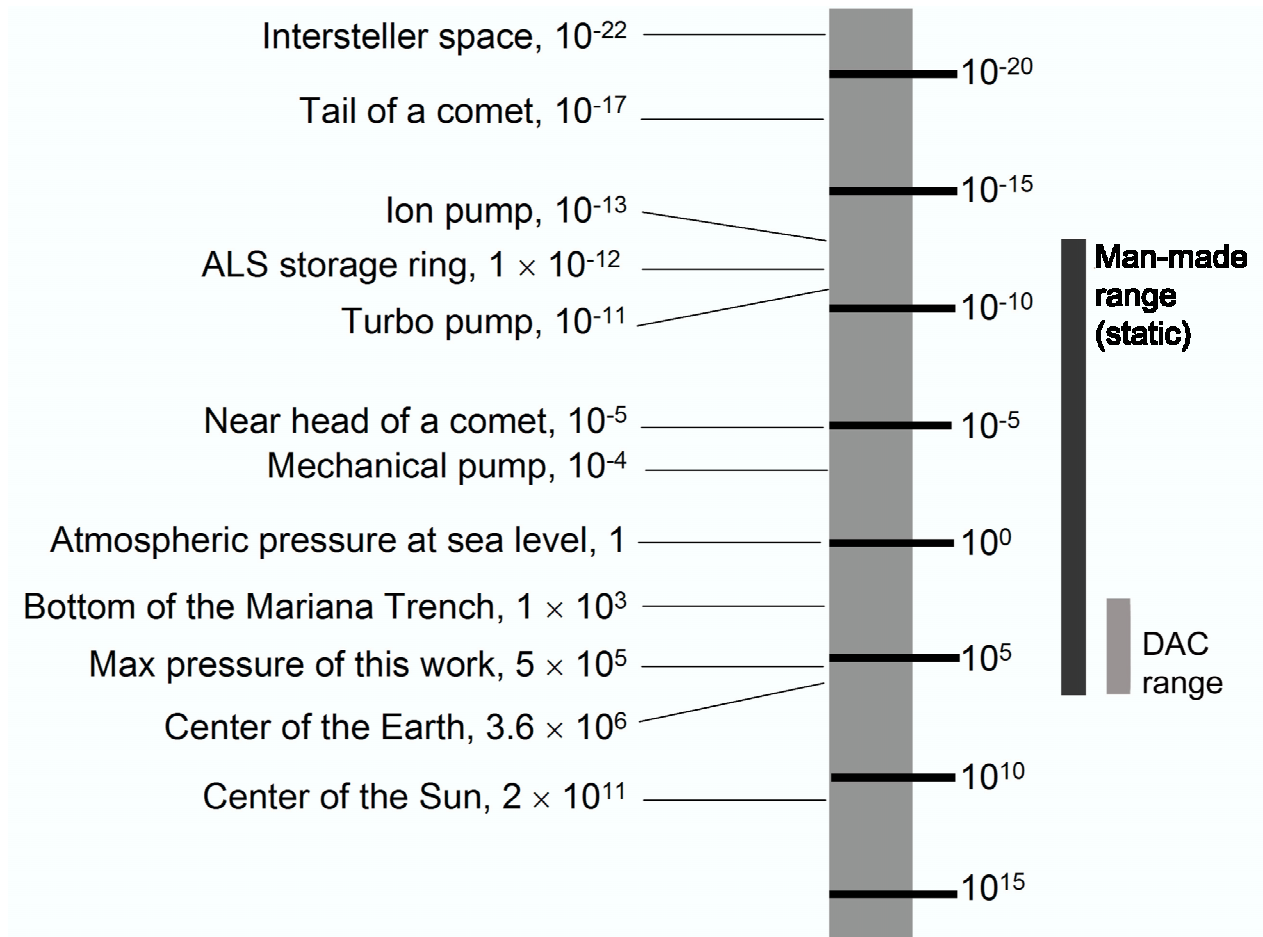
Figure 1.2: Logarithmic line graph of the range of pressures observed in nature and observable by human means. Units are powers of 10 of bar (1 bar = 10,000 Pa, or approximately atmospheric pressure). References: Astronomical, Physics and Chemistry of the Solar System John S. Lewis, Elsevier 1997; Interstellar space, Nicholas A. Pananides and Thomas Arny. Introductory to Astronomy Second Edition. 1979; Advanced Light Source, ALS website: www-als.lbl.gov; Vacuum values, Steven T. Robertson, personal communication.

conditions of the Earth's interior, even to the core, in the laboratory.

The DAC also enabled physical chemists to study molecules under very extreme conditions. This was largely motivated by the prediction [22] that molecular hydrogen would break down and form a metallic solid at 25 GPa. In a similar vein, another basic science motivation for high pressure has been the study of high pressure solid-solid phase transitions, also known as structural transitions. These occur when surfficient pressure is applied to a solid to invert the thermodynamic stability between two phases, leading to a phase transition to a more dense phase. It is this class of high pressure studies which will largely be the focus of this work.

1.4.2 The diamond anvil cell

The instrument of choice for high pressure is the diamond anvil cell (DAC) [23, 24, 25, 26]. A pair of opposing diamond anvils are mounted in a cell which holds the diamonds in place. Enormous pressures are generated not by using large a force but by concentrating a modest force over a small area. Typically, the diamond faces in use (culets) are polished down to sizes of between 250–600 μm. Thus, for the 300 μm diamonds used for this work, a force of about 3500 N is all that is needed to produce 50 GPa of pressure at the culet. Pressures of up to 5 megabar (Mbar) or 500 GPa in diamond anvil cells have been reported [27]. Diamond is an excellent choice of material for the anvils for two reasons. First, diamond is the hardest naturally occurring material. With its strong covalent bonds, it will resist deformation up to extreme

pressures, at which point it will fracture. Second, the diamonds are transparent to much of the electromagnetic spectrum. All of the visible, much of the IR (with Type II diamonds) and the hard x-ray region are weakly absorbed by diamonds. This allows for many types of spectroscopy to be conducted: UV-Vis, visible fluorescence, IR, Raman, x-ray diffraction and x-ray absorption (XAFS, etc.).

1.4.3 High pressure studies

Diamond anvil cell high pressure studies have given many insights into the functioning of the Earth's interior and even that of other planets. One method is to place the likely constituents a given at the pressure and temperature of region and observe the phase that results. In this way it is known that, for example, FeO is in the nickle-arsenide structure at the core mantle boundary (140 GPa) and that it forms because of the reaction between silicates in the mantle and liquid iron from the core [28]. By studying methane gas under high pressure and temperature, Benedetti et al. [29] predicted that diamond would form within planets like Uranus and Nepture.

Extensive experiments have been conducted into the aforementioned metalization transition of hydrogen. Experiments up to 250 GPa have yet to observe the metalization, but transitions between a number of solid phases have been observed [30, 31]. While this remains a sort of "holy grail" for high pressure science, it has spawned investigations into a host of other molecular systems [32, 33] which also exhibit phase transitions. In one of the more striking directions of high pressure, recently ex-

1 GPa	=	10 kbar
1 Mbar	=	100 GPa
1 atm	=	101,325 Pa
1 bar	=	100,000 Pa
1 bar	=	0.98692 atm

Table 1.1: Various units of pressure used in the high pressure literature, Abbreviations: atm = atmospheres; Pa = pascals (N/m^2); kbar = kilobar; GPa = gigapascals; Mbar = megabar

periments have been carried out on biologically relevent systems [34], including the observation of respiration in bacteria up to 1 GPa of pressure [35].

A brief note on units

Like many fields, high pressure research has its own list of units, the use of which can be confusing. A brief list of units and their conversions is given in Table 1.1. The convention in this work will be to use the SI units of gigapascals (GPa).

As an example, the pressure at the center of the Earth is 360 GPa, 3600 kbar, 3.6 Mbar, or about 3.6 million times atmospheric pressure.

1.5 Observing high pressure transitions using x-rays

1.5.1 Synchrotron radiation for high pressure studies

While diamonds are generally considered "transparent" for x-ray energies above 10 keV, this is only partially true. At 10 keV, x-rays have a penetration depth (distance for which the intensity decreases by 1/e) of 1.29 mm, increasing to 7.78 mm at 20 keV. Because each diamonds is 3 mm thick, even at 20 keV the absorption is significant. Additionally, the use of small diamond culets to reach high pressures results in very small sample volumes in the DAC. In this study, the typical sample volume is 1.0 nanoliter. In order to obtain detectable x-ray diffraction signal from such a small volume within 3.0 mm thick partially absorbent windows, an extremely strong x-ray source is necessary. Laboratory sources are far too weak, and a synchrotron radiation source [36] [37] is needed. Synchrotron sources are particle accelerators which bring (generally) electrons to speeds approaching c, the speed of light. At non-relativistic velocities, a charged particle moving in a roughly circular path will produce electromagnetic radiation in both directions perpendicular to the centripetal acceleration (FIG. 1.3). However, in the relativistic regime, the output radiation becomes concentrated in a very intense beam of light projected in the forward direction [38]. Furthermore, depending on the storage ring parameters, output photon energy can be extremely high, reaching energies in excess of 40 keV (0.31 Å).

The Advanced Light Source, the synchrotron at which the data for this work
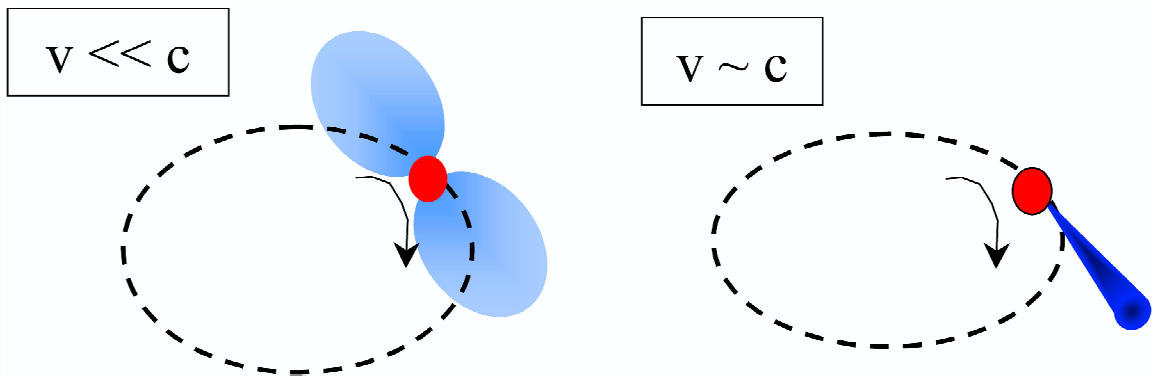
Figure 1.3: Comparison of the non-relativistic and relativistic case of a centripetally accelerated charged particle. In both cases, electromagnetic radiation is given off, but while the non-relativistic case produces diffuse radiation in both tangential directions, the relativistic case produces an intense forward beam.

were collected, is not a high energy source. Primarily designed for soft x-ray work, the energy fall-off for a bend magnet becomes very steep just below the 10 keV threshold for diamond transmission. However, a tightly focused beam is sufficient to do some high pressure work with reasonable data collection times. Recent advances in synchrotron technology, however, have allowed for the construction of much stronger bend magnets ("super-bends") on which it will be possible to operate routinely at 20 keV (0.62 Å). One of the goals of this work from the outset was to utilize a bending magnet at the ALS for high pressure work in preparation for the commissioning of a dedicated high pressure beamline on a super-bend magnet beamline. This beamline dedicated beamline is scheduled to open in early 2004. This work demonstrates the success that can be had on a normal bend-magnet beamline, pointing to a great potential for success on the new beamline.

1.5.2   X-ray diffraction

A number of synchrotron x-ray techniques have been used for the study of nanocrystals. Hamad et al. [39] used near-edge x-ray absorption fine structure spectroscopy (NEXAFS) to study the surface structure of nanocrystals. XAFS, x-ray absorption fine structure, has been used to track the bond length change at high pressure [40]. However, the technique of choice for studying structural phase transitions at high pressure remains x-ray diffraction. This is true for a number of reasons. A change in phase is generally obvious from the appearance of the unique diffraction pattern associated with the new phase and with the disappearance of the pattern of the old phase. The d-spacing information that can be extracted from the peak positions gives the unit cell volume which can then be plotted as a function of pressure. This allows for the determination of the equation of state and compressibility. For nanocrystals, there is the added information that can be obtained from the peakwidths. Nanocrystal peakwidths are broadened due to the finite size of the scattering domain, a phenomenon known as Debye-Scherrer broadening.

The normal derivation of the Bragg condition for x-ray diffraction is as follows (FIG. 1.4). A crystal is imagined as a series of regularly spaced layers of atoms of interval d. X-rays of wavelength λ incident at an angle θ scatter from these layers specularly, that is, as though off a mirror. Each "mirror" is only slightly reflective and most of the x-rays pass through each layer, though they may be reflected at subsequent layers. The pathlength difference for rays between successive layers is
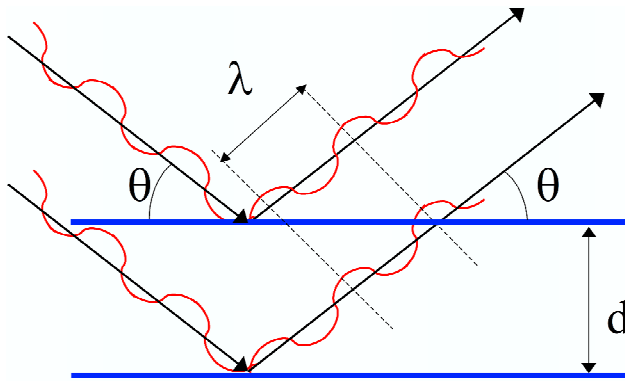
Figure 1.4: Normal construction of x-ray diffraction in the Bragg picture.

$2d \sin \theta$. Interference of these reflected waves will be *perfectly* coherent (for a far away observer) only if this pathlength difference is an integer multiple of the wavelength, that is:

$$n\lambda = 2d \sin \theta$$

which is known as the Bragg equation, where each value of θ which satisfies this equation is refered to as a Bragg angle.

However, there is an implicit assumption in this equation, that the crystal is infinite in extent. This assumption becomes clear from considering what happens for a slightly off-Bragg angle, $(\theta + \epsilon)$. Considering just two sequential layers the coherence of the interference would fall off gradually as the scattering from the two layers become gradually more out of phase with one another. In an infinite crystal, however, any slightly off-Bragg angle reflection is perfectly canceled out because some reflection will happen to be exactly 180° out of phase with that from the first layer.

In the case of nanocrystals, this infinite crystal assumption is not satisfied. Because of this, the intensity falls gradually from the peak value at the Bragg angle. This results in a broadening of the peaks. The broadening will be inversely proportional to the number of crystal layers, N, in nanocrystal. A precise derivation [41] of this effect results in:

$$\Delta\theta = \frac{\lambda}{D\cos\theta}$$

where $\Delta\theta$ is the full-width at half-maximum of the peak and D is the diameter of the nanocrystals (D = N×d).

1.6   Conclusion

The goal of this chapter is to explain the background necessary to understand the research presented in this work. It is meant to place the research presented here in its proper scientific context. However, let us briefly consider the yet broader context.

Nanoscience is often viewed as a bridge between chemistry and solid state physics. Nanocrystals fit neither the chemist's canonical view of molecules nor the physicist's view of (near infinite) solids. From the chemist's perspective, nanocrystal structural transitions are an extreme version of an isomerization. This isomerizaton involves a large number of atomic movements and has a large energetic barrier, but nonetheless the exact location of the atoms (particularly at the surface) are of great importance. For the physicist, nanocrystal transitions are the finite version of a phase transition,

where the periodicity of the truncated lattice shifts suddenly at a given pressure.

While both perspectives can help us understand nanoscience, the true question is whether nanoscience can be used to help us understand physics and chemistry. This work attacks that question by asking (and hopefully answering) specific questions about nano-scale systems that blend concepts both fields. In the case of iron oxide, what happens when structural transitions occur in the absence of defects? By understanding the size trends in nanocrystals systems, can one extrapolate to the (fictitious) "perfect" bulk material? How does the aggregation of nanocrystals change the near perfection of nanocrystals and what does that tell us about the bulk? In the case of TiN, can the right nano-scale design prevent defect propagation that would rip bulk materials apart under the same stress? Do coupled nanocrystal systems behave more like bulk or the classic dissolved, uncoupled CdSe system? Answering these questions are the goals of this work.

Chapter 2

Experimental procedures

2.1 Introduction

This chapter will introduce the experimental details which are general to most of the experiments presented in this work. It is divided into two parts, the first dealing with high pressure diamond anvil cells, the second with colloidal nanocrystal synthesis. Each of these are explained in the literature, and useful reviews and books are cited. However, this chapter is primarily for those who may wish to reproduce the results presented in this work. It is therefore important to document the exact techniques used and to describe any deviations from standard procedures.

2.2 High pressure experimental: diamond anvil cells

2.2.1 High pressure general

The study of high pressure has been largely motivated by interest in geologic processes. The pressure at the Earth's core-mantle boundary is 140 gigapascals (GPa), while at the center of the Earth the pressure is 360 GPa. By choosing the right mixture of materials and pressure/temperature combination, the interior of the Earth [26] or other worlds [29] can be simulated in the lab, allowing for the study of otherwise inaccessible conditions. In addition to geologic interests, high pressure has been applied to simple molecular systems [32] in which even the strong intramolecular bonds of diatomic nitrogen [33] can break down, causing a transition from discrete molecules to an extended solid.

The instrument of choice for high pressure is the diamond anvil cell (DAC) [23, 24, 25, 26]. Utilizing the hardest material possible, a pair of opposing diamond anvils are mounted in a cell which holds the diamonds in place. Enormous pressures are generated not by using large a force but by concentrating a modest force over a small area. Typically, the diamond faces in use (culet) are polished down to sizes of between 250–600 μm. Thus, for the 300 μm diamonds used for this work, a force of about 3500 N is all that is needed to produce 50 GPa of pressure at the culet. Pressures of up to 5 megabar (Mbar) or 500 GPa have been obtained in diamond anvil cells [42].
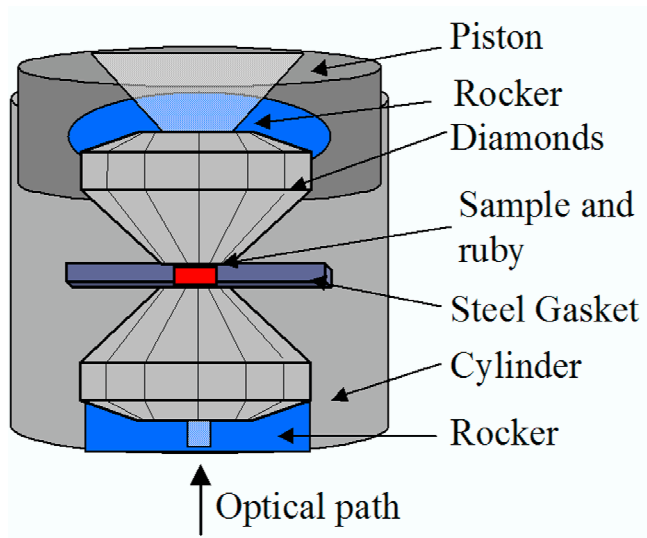
Figure 2.1: General schematic of a diamond anvil cell

All diamond anvil cells share a number of characteristics, for which a schematic is given in Figure 2.1. The opposing diamonds are mounted on rockers, movable plates that allow for accurate diamond alignment. Except in Merril-Basset cells, each rocker is held to either a piston or a cylinder. The sample is held in place between the two diamonds by a metal gasket which has been preindented with the diamonds and had a small hole drilled in it. The gasket also allows for quasi-hydrostatic conditions to be obtained by preventing the sample from flowing outward. The sample may be solid, liquid, or gas, but generally solid samples are loaded in either a liquid or gas medium which creates a hydrostatic pressure environment for the sample. Often, a few chips of ruby are added which allow for the in-situ determination of pressure within the cell. A clear optical path is available along the cylindrical axis of the cell, allowing for the transmission of IR, visible, and x-ray radiation.

2.2.2 Cell design

The diamond anvil cell used in this work is the WCME-DAC from Diacell (United Kingdom). This cell is membrane-driven, i.e., the load is applied by means of gas pressure inflating a small bellows held in contact with the piston. This allows for both precise control of the applied load as well as for the pressure to be controlled remotely. This latter point underlies the design of the x-ray diffraction set-up at the Advanced Light Source used in this study (see Chapter 3.2). The cell also features a hybrid set of backing plates, one tungsten carbide, the other beryllium (Be). Be has an extremely small x-ray scattering cross section (scattering goes as Z^2, where Z is the atomic number, or equivelently, number of electrons) while being quite hard, at least at room temperature. The Be plate is oriented towards the detector, allowing for the transmission of x-rays and the collection of x-ray diffraction patterns over the entire 360º of χ (the polar angle in the plane of the detector). Other cells use tungsten carbide (WC) for both plates with a slit in the rear-facing backing plate which allows only about 20º in χ to be collected. However, nanocrystals scatter more weakly than bulk samples, and the ability to collect the full 360º of χ critically improves the signal-to-noise ratio.

Because the WCME-DAC is piston-cylinder style, it allows for the precise control of the anvil-to-anvil approach. Such control is unneccesary for pressures below 10 GPa, and DACs of the Merril-Basset style will suffice. However, because this study requires reaching much higher pressures (up to 50 GPa), a piston-cylinder DAC is

needed. Precise alignment of the diamonds relative to each other and their stability at high pressure is necessity for pressures above 10 GPa. For this reason, the diamonds are mounted on a lateral translation plate on the piston, while the Be rocker on the cylinder is hemispherical allowing for tilt alignment. These stages are manipulated by tightening and loosening four or three screws for the lateral or tilt alignment, respectively. Having the two degrees of freedom necessary for alignment on separate diamonds simplifies the alignment procedure, though in reality the lateral and tilt alignment are never entirely decoupled. For this reason, proper alignment requires several iterations of lateral and tilt alignment. A full description of the somewhat difficult alignment proceedure is given in Appendix A.

2.2.3 General cell use

Gasket making

The material used for gaskets must be a hardened metal which can hold its shape under pressure, but is not too brittle. The material has to allow a certain amount of plastic flow under a load. Typical materials used are hardened steels such as spring steel or stainless steel and rhenium. Gaskets used in this study were made from 0.25 mm thick spring steel, which contain about 1 % carbon.

Making a gasket is a two step process. The first is preindention, the second is creating a hole. Preindention is necessary to strengthen the steel. The degree of preindentation is very important. Under indenting will lead to a gasket that is too

soft, and the gasket material may flow under pressure, leading to an unstable gasket hole. Over indentation leads to a weak load-pressure response (see Eremets [25] §3.3.4.1). The appropriate level of indentation found for this study, using 300 μm diamonds and using spring steel gaskets to attain 50 GPa, is to indent to 60 μm. This thickness is measured using opposing sharp tips, one of which is at the end of a Mitutoyo depth gauge. The gas pressure load needed to indent to 60 μm is between 35–40 bar, but the thickness of preindented gaskets should be directly checked on a routine basis.

Gaskets were cut to approximately 1 cm $\times$ 0.5 cm. Larger gaskets were found to be difficult to hold in place after indentation because they would bend back away from the diamonds. Gaskets were held in place for indentation using modeling clay. Gaskets were marked with a permanent marker or scratched to indicate the orientation in which they were indented. This is important because the indented gasket must closely match the diamonds on which it is mounted for stability at pressure. Gaskets were only used on that cell with which they were preindented.

Gasket holes can be made by drilling or using an electric-discharge device which erodes the metal. For this study, holes were drilled using a Servo drill press with 0.15 mm diameter drill bits (H. A. M. Technology USA, Anaheim, CA) viewed from an angle using a stereo-zoom microscope. Holes that were judged too close to the edge, with less than about 20 μm of rim between hole and diamond indentation edge, were discarded. With practice and using a new drill bit, a success rate of about one in two
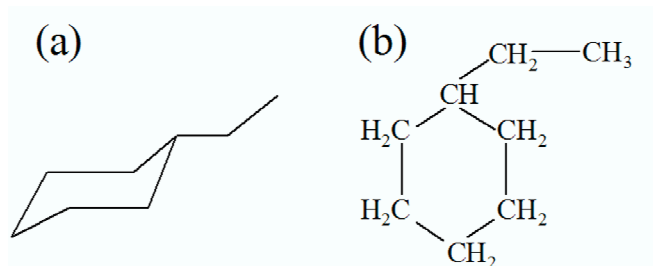
Figure 2.2: (a)Line notation and (b) molecular structure of ethylcyclohexane. The presence of the ethyl group off the cyclohexane ring prevents efficient stacking. This steric hinderance causes ethylcyclohexane to have a high freezing pressure (low freezing temperature) compared to other hydrocarbons.

or three is possible. Drilling has the drawback that it leaves metal burs in the hole. These burs were assiduously removed using a sharp needle tip because of the strong diffraction possible from stray bits of steel in the gasket hole.

Sample medium and sample preparation

In diamond anvil cell use, samples are generally dispersed in some kind of medium. The medium helps to redirect the uniaxial force of the approaching diamonds, leading to quasi-hydrostatic conditions. All samples in this work, except where noted, were loaded in ethylcyclohexane (ECH) (FIG. 2.2). This solvent has proven to be a very good quasi-hydrostatic medium for nanocrystal studies [12] [5] [9]. The primary benefit of ECH over, for example, 4:1 methanol/ethanol, is that colloidal nanocrystals are soluble in ECH as a result of their surfactant surface termination. This leads to the unique situation in high pressure science where each inorganic domain is separated from another, both by surfactant and pressure medium. Using the breadth of the ruby spectra as an indication of hydrostaticity [25], ECH is quite hydrostatic to 10
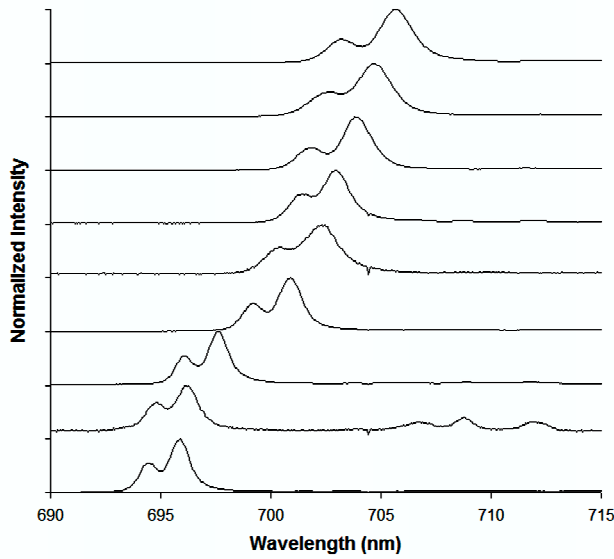
Figure 2.3: Typical ruby spectra

GPa (FIG. 2.3), above which it becomes less so. In spite of this decrease in the hydrostaticity, the trade-off between solubility and hydrostaticity has been consciously made.

For x-ray diffraction studies of colloidal particles, it is necessary to have very high nanocrystal concentrations. Without high concentrations, high quality, high signal-to-noise diffraction data cannot be obtained with reasonable (on the order of 30 minutes) collection times. All samples were dissolved in a small amount ($\sim$0.01 mL) of ECH and agitated with a "vortex device for approximately 30 seconds, generally leading to an optically clear solution. If aggregation or opalescence persisted, a very small amount of the surfactant hexadecylamine ($\sim$ 1 mg) was added and the sample was agitated again. Adding too much hexadecylamine can lead to the solid precipitating under

pressure. When high nanocrystal concentrations were difficult to achieve, solvent was allowed to evaporate during loading as described below.

Loading samples

All work is done under a stereo-zoom microscope with 150× zoom capability. The entire diamond cell is thoroughly cleaned before each use, including using toluene or another hydrocarbon solvent to preclude any possible contamination from previous samples. Diamonds were wiped clean using low dust cotton swabs with a drop of methanol or ethanol. The pre-made gasket was placed back in the cell on the cylinder diamond in the same orientation in which it was made according to the mark on the gasket.

Three or four small ($\sim 10\ \mu$m) ruby chips were placed with a needle onto the piston diamond. The rubies were placed in an area where, by comparison with the exact location of the gasket hole on the cylinder diamond, they were likely to fall close to the center of the gasket hole. This was found to be effective for two reasons. First, rubies placed directly in the gasket hole tended to wash out upon solvent loading. Second, because of the geometery of the cell, ruby spectra are collected from the piston side, but the piston diamond faces upstream in the x-ray beam, minimizing x-ray diffraction peaks from the ruby.

A drop of prepared sample in pressure medium was deposited into the gasket hole. If the sample concentration was not high enough, the solvent was allowed to evaporate

for up to a minute. The close match between indented gasket and diamonds in the cell makes this possible because the sample does not leak. The sample concentration increases during evaporation, often to the point of forming a gel. The piston is then placed in the cell in the proper orientation and quickly pressed down. The piston is held down while the membrane, spacer, and holding bolt are tightened on. The holding bolt may be strongly hand tightened or tightened with a strap wrench/curved plier pair as necessary depending on the response of the cell. Overtightening with the wrench/plier combination can place the cell at 10–15 GPa initially, so if lower pressures are needed hand tightening is advised. However, it is important that the cell be well tightened. The maximum travel of the membrane is 0.25 mm. If any space remains between cell components, no load will actually be applied until this space is taken up by the expanding membrane.

In order for a loading to be successful, an unstrained ruby (as determined from the spectral peak shape) must be found within 20 μm of the center of the gasket hole. If this is not the case, pressure gradients in the cell at low pressure can lead to large underestimates of the cell pressure. This can be seen in Figure 2.4 where the pressure was observed at the center and the edge of the cell. Between the center of the cell to the edge the pressure gradient is about 30% above 20 GPa.
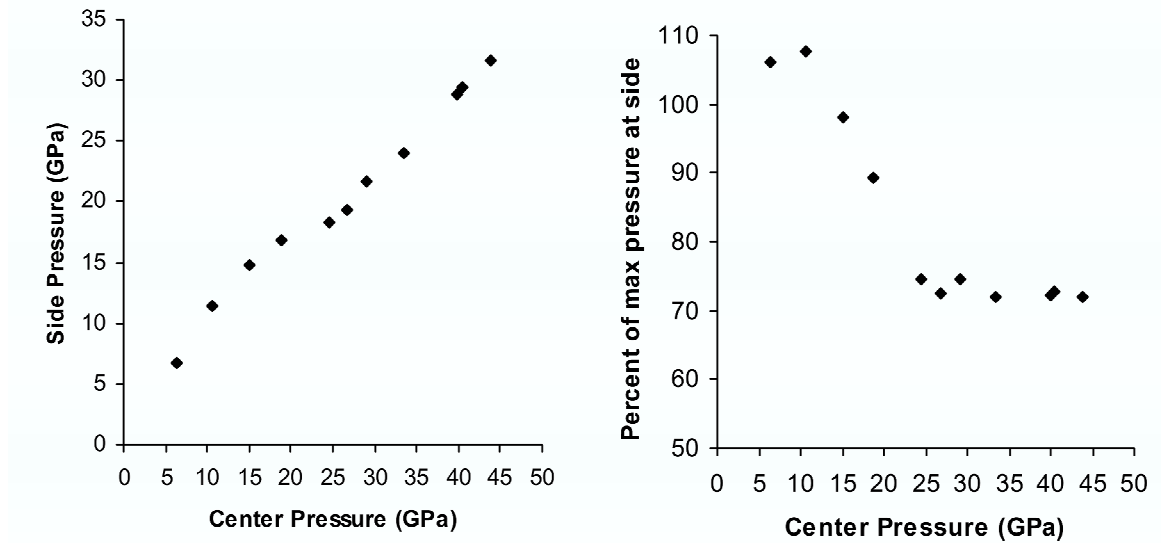
Figure 2.4: Difference in pressure between the center and edge of the gasket hole in a typical experiment. This gives an indication of the amount of pressure gradient across the cell

Cell pressurization

The cell is attached to the pressurizaiton system shown schematically in Figure 2.5. A high gas pressure regulator is attached to a helium gas cylinder with at least 100 bar (1450 psi) of pressure remaining (He is used mainly for historical reason of use in cryogenic environments — any inert gas is suitable). The regulator is attached to the control box with a high pressure hose. The control box is used to accurately measure the gas pressure and to provide cut-off and vent valves for the gas system.

The membrane is attached to the pressure box with a capillary tube with a quick-connect Swaglok piece and a valve to allow the cell and tube to be disconnected from the pressure box. This tube, which is 1/16 inches OD must have wall thickness between 0.012 inches and 0.016 inches and must be 304 low carbon stainless steel in

He

40 bar

Membrane

Piston

300 μm culet
Diamond anvils

Cylinder

Be backing plate

Max disp
.25 mm

Hemispherical
rocker
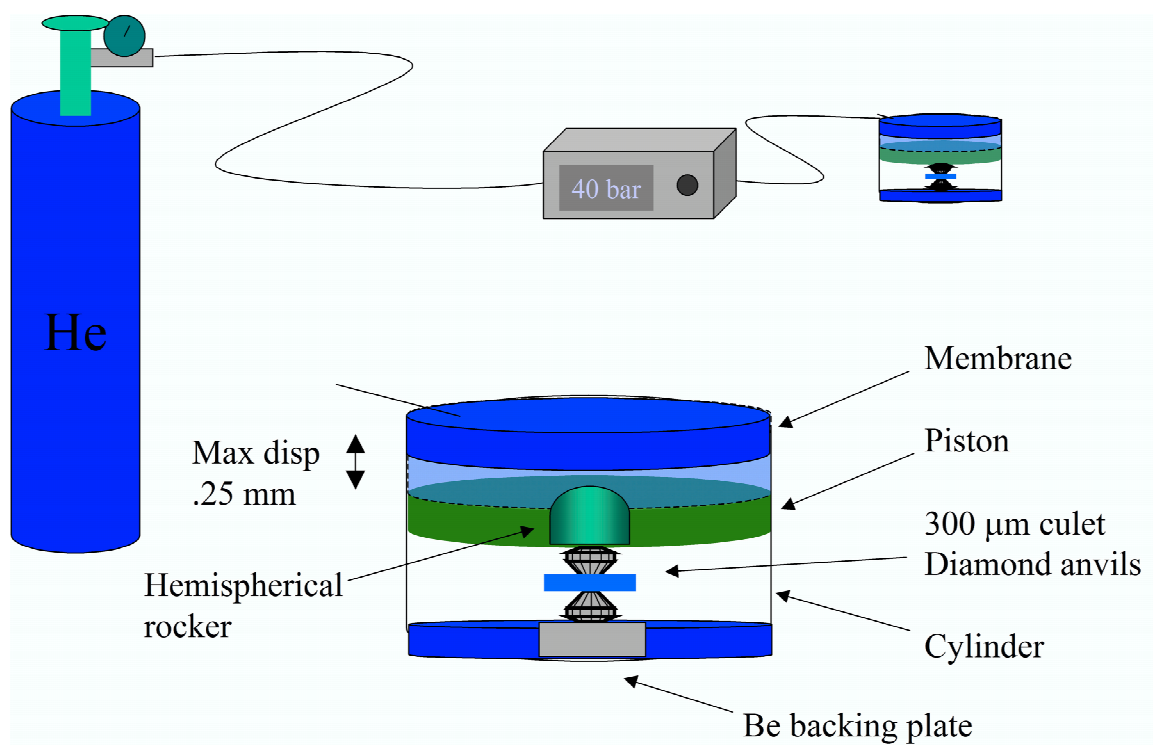
Figure 2.5: Schematic of gas pressurization set-up and membrane cell
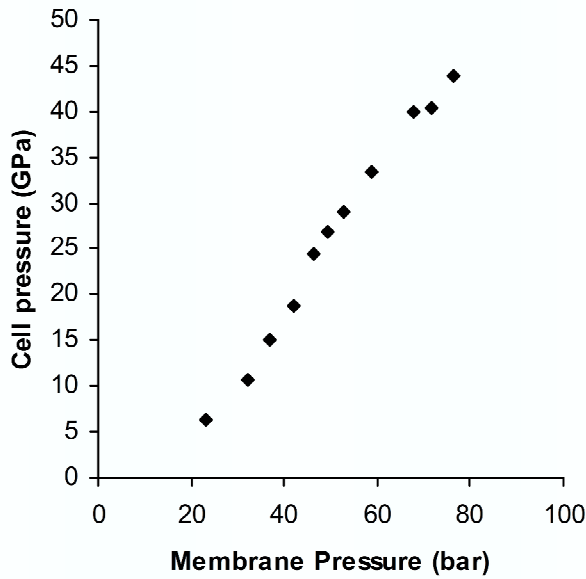
Figure 2.6: Load/pressure response curve for a typical gasket in this work. In the load range used ($<$ 100 bar), the load/pressure response is nearly linear.

order for safe operation [43].

Gas pressure is controlled at the regulator. The in-situ pressure is monitored in the ruby spectroscopy set-up while the gas pressure is increased. The load-pressure response depends very strongly on the gasket pre-indention conditions. A typical load-pressure curve is shown in Figure 2.6. At gas pressures below 10 bar there is a very weak response. However, above 10 bar the response can be quite strong, showing a nearly exponential behavior. At high enough load this curve will sometimes level off, a sign that the gasket is beginning to undergo laterial plastic deformation and about to fail. Any experiment in which this leveling off was observed was terminated.

The unloading response is very weak. A substantial under pressurization from

the gas system is necessary to observe even an initial cell pressure drop. This makes obtaining downstroke data quite difficult. The poor response may be due in part to the piston/cylinder friction which could be reduced with the use of a lubricant. However, the poor downstroke response may be primarily due to plastic deformation of the gasket, making it impossible for the gasket to rebound against the diamonds as pressure is reduced. Gaskets are certainly thinner after pressurization to 50 GPa than before, even when the hole size and shape is maintained. Perhaps an adjustment in the preindention amount or the use of a different gasket material could help in this regard. Another solution might be to use internal springs which would help push diamonds apart upon unloading.

Ruby spectroscopy

In-situ pressure was observed using standard ruby spectroscopy [25]. Cr^{3+} doped α-Al_2O_3 shows a nearly linear shift in the R_1 and R2 fluorescence peaks positions under pressure. Pressure is determined according to

$$P = \frac{R_{1,2}(P) - R_{1,2}(1 \text{ atm})}{0.365 \text{ nm/GPa}}$$

where $R_{1,2}(P)$ is the position of either the R_1 or R_2 peak at a given pressure, and $R_{1,2}(1 \text{ atm})$ is the position of either the R_1 or R_2 peak at atmospheric pressure.

Experimentally, the main difference in this study and previous ones in our research group is the use of fiber optics instead of free laser beams. This was done for two reasons, both with an eye towards the design of a system for use on the x-ray station

at ALS. First, fiber optics are generally safer than free beams, both for the operator and people who come in casual contact with the system. The latter can be frequent at a general use facility like a synchrotron. The use of fiber optics effectively changes the system from a Class IV laser system to a Class IIb. Second, fiber optics can carry both the laser and fluorescence over long distances, in this case between a laser and spectrometer located outside the x-ray hutch, a necessity for a remotely controlled system.

The set-up is shown schematically in Figure 2.7. An Ar-ion laser tuned to 514 nm or 488 nm was used to pump flourescence. The 514 nm line gives much stronger signal at low pressures. However, the 488 nm line was necessary to obtain good signal for P > 20 GPa due to better overlap with the broad ruby absorption band which shifts blue with pressure. The laser beam is coupled into the fiber optic with an air-to-fiber coupler. The coupling depends very strongly on the angle between the beam and the coupler. For this reason, the coupler (and every subsequent coupler) was mounted on a stage with x and y translation and θ and ϕ tilt. The laser fiber optic is a single-mode fiber optic cable (Thorlabs Optics). The laser is coupled into the microscope using another fiber-to-air coupler. The microscope is an Olympus BH-2 with a 0.3 numberical apperture and a 32 mm working distance. The epifluorescent ruby signal is collected and sent out to a bundled fiber optic with a row output at the end. This feeds into the ARC SpectraPro-300i spectrometer which has a 300 mm focal length and an f/4 focal ratio. This in turn feeds into an ARC 128HF SpectruMM
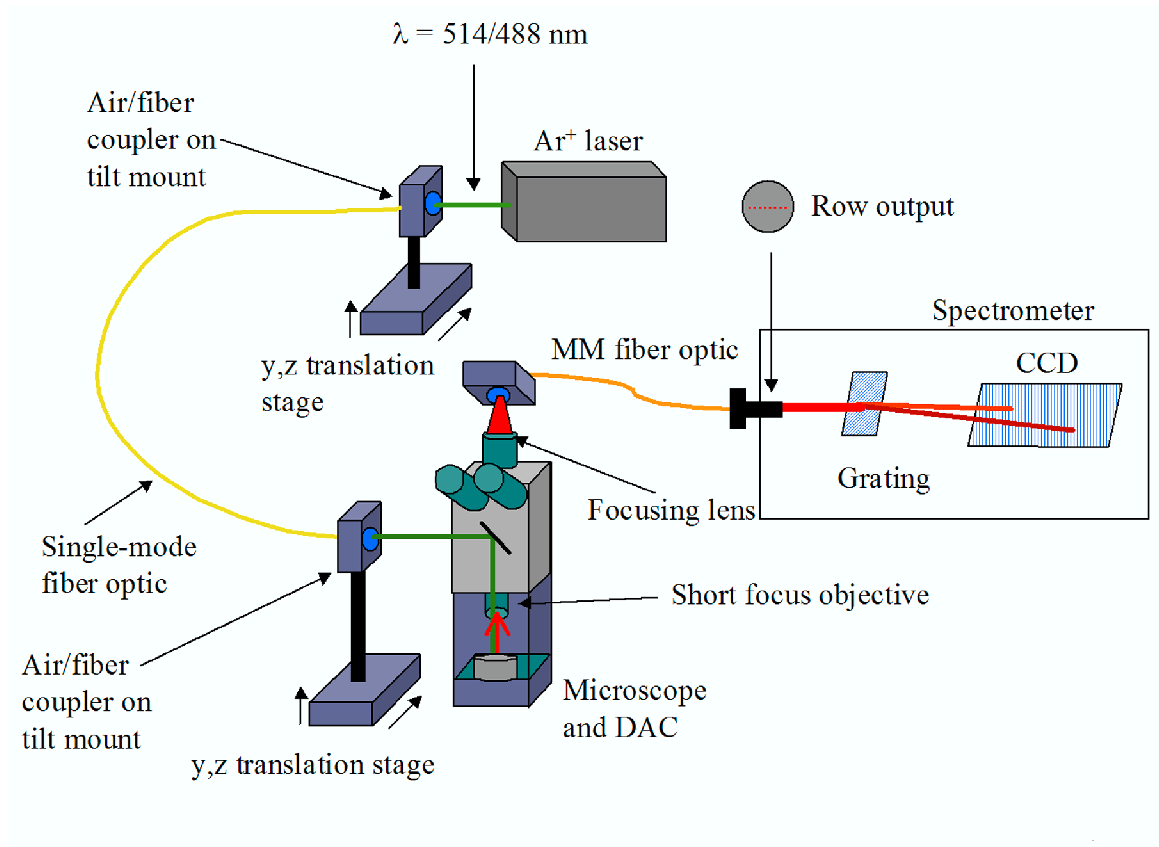
Figure 2.7: Schematic of the experimental set-up used obtain ruby fluorescence in the DAC. The pump laser beam is fed into the microscope using fiber optic cables. Fluorescence is collected by the same objective used to focus the laser beam into the cell (epifluorescence). The light then passes out of the microscope and is focused back into a fiber optic, which in turn feeds into the monochromator/CCD.
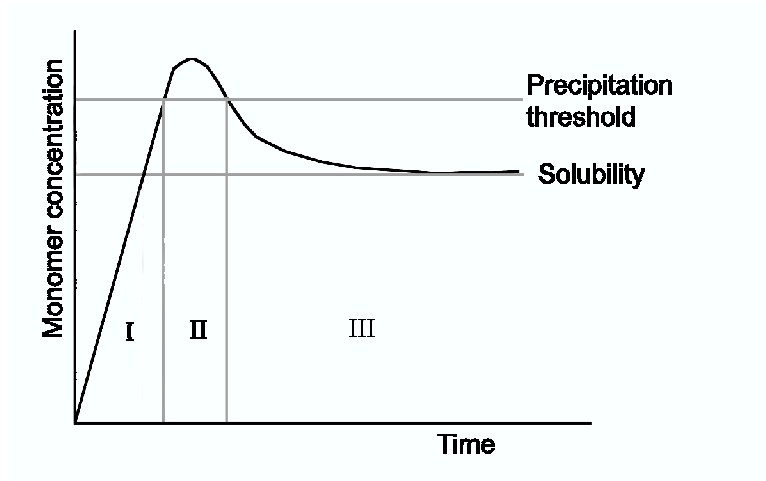
Figure 2.8: Monomer concentration in a colloidal nanocrystal synthesis, after LeMer and Dinegar [44].

thermoelectrically cooled CCD. Resolution is approximately 0.05 nm.

2.3 Iron oxide nanocrystal synthesis

2.3.1 Introduction

Almost all colloidal nanocrystal syntheses follow the same motif — precursors aredecomposed in hot surfactant. Ideally, the decomposition creates a very sudden increase in the concentration of constituent atoms or ions, creating a supersaturated solution (FIG. 2.8 [44] region I). The constituent ions nucleate small clusters of the nanocrystal material (region II) resulting in a sudden decrease in monomer concentration. However, the solution is still supersaturated, and growth continues until the supersaturation is completely relieved (region III). This growth never results in macroscopic crystals because it is slowed by the presence of the surfactant. The
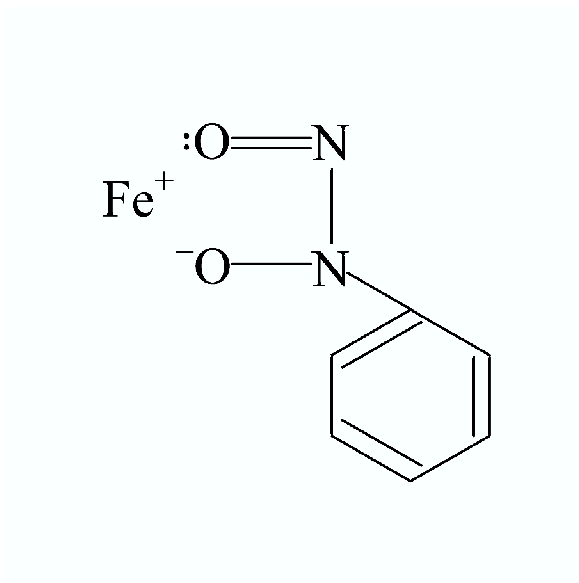
Figure 2.9: Structure of iron cupferronate, the precursor molecule used to generate iron oxide nanocrystals.

nanocrystals are allowed to grow at high temperature, allowing the slow, epitaxial growth of defect free crystals. The size distribution of the nanocrystals depend on the sharpness the nucleation step so that all nanocrystals nucleate and begin growing at precisely the same time.

The varation on this this theme employed here to make iron oxide was developed by J. Rockenberger [45]. The reaction depends on a single molecular precursor, iron cupferronate. Cupferrone, N-Nitrosophenylhydroxylamine Ammonium (CAS 135-20-6), shown in Figure 2.9, is a bi-dentate ligand. The molecule binds well with many transition metals, and the corresponding complexes have a very low equilibrium solvent product, K_{SP}, in water. The complexes ("cupferronates") tend to be thermally unstable. As such, cupferronates were proposed as a general precursor

route to transition metal nanocrystals, and were found to make quality nanocrystals of Fe_2O_3, Cu_2O and Mn_3O_4 [45]. They are generally synthesized in long chain amines, but Deborah Aruguete in our research group has found that phosphine oxides work well also [46], suggesting that the nature of the surfacant may not be of great importance.

2.3.2 Iron oxide nanocrystal synthesis technique

Iron cupferronate preparation

Iron cupferronate was prepared in the same way outlined in Reference [45]. However, the synthesis was scaled up by a factor of two. 2.24 g of $FeCl_3 \cdot 6H_2O$ was dissolved in 280 mL of 1% HCl. To this solution was added 153 mL of concentrated HCl and 525 mL of H_2O (all H_2O used is Millipore purified). These steps are necessary to dissolve the $FeCl_3$ and then to reach an appropriate pH for maximum precipitation in the next step. 6.0 g of cupferrone was dissolved in 200 mL of H_2O, which was then added drop-wise to the stirred $FeCl_3$-HCl solution from a buret. Precipitation of iron cupferronate was immediate. The resulting solution was allowed to sit for ten minutes, then placed in a refridgerator for about 1 hour. The solid was separated with a Buchner funnel and filter paper. The recovered solid was dissolved in chloroform and separated from the water layer in a separatory funnel. This chloroform solution was concentrated in a rotovap to about 10 mL. Hexanes were added, initiating the precipitatation of the iron cupferronate. This solution was allowed to sit overnight in

Schlenk line
(vacuum or Ar) → bubbler

Thermal
controller

180 ºC
270 ºC

Septa

Thermocouple

Heating mantle

IKA Stirplate
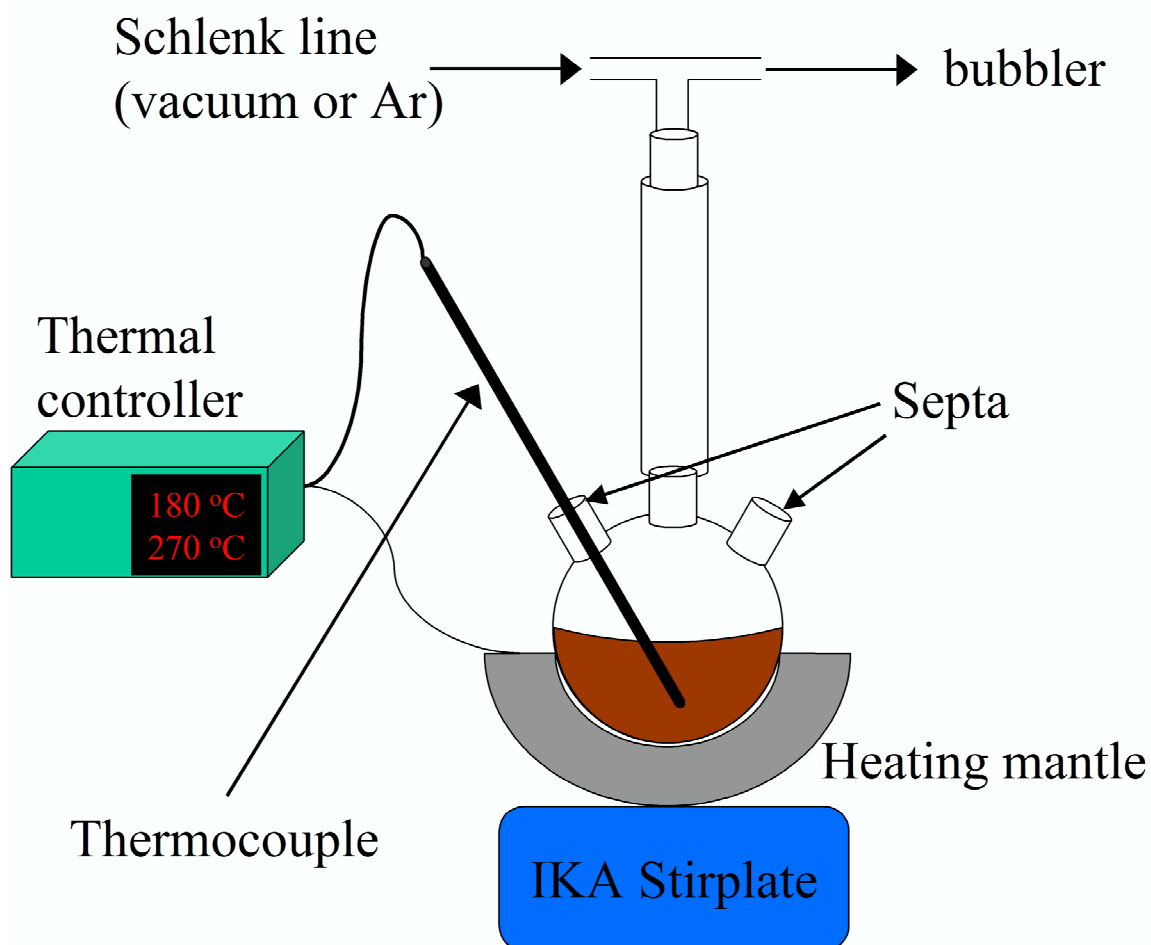
Figure 2.10: Schematic of glassware set-up for nanocrystal synthesis

a refrigerator, after which the supernatant was decanted. Black or dark brown iron cupferronate crystals remained in the flask.

Nanocrystal synthesis

1.00 g of 99% purity hexadecylamine (HDA) and 0.24 g of iron cupferronate were added to a 25 mL three-necked flask with a small (15 × 8 mm) stirbar, and placed in

a standard nanocrystal synthesis set-up (FIG. 2.10). The flask is attached to a reflux condensor, which is attached to a T-piece. The T piece is attached on one side to a bubbler, on the other to a gas/vacuum Schlenk line. The other two necks of the flask were covered with rubber septa, one of which is pierced with a needle and into which a thermocouple is inserted. The thermocouple is attached to a temperature controller which regulates the heating mantle into which the flask is set. The flask and mantle are set on a stirplate, model IKAMAG RET basic from IKA Works. The use of this specific stirplate is *critical* to the success of the synthesis, as it can sustain a very high speeds (1100 rpm) with a large magnet which holds the stirbar in place.

The flask is pumped and purged three or four times at room temperature, then placed under vacuum (approximately 100 mtorr). The temperature controller is set to 50ºC with the stirplate at about the 6 setting. When the HDA melts just below 50ºC the cupferronate dissolves exothermically, causing a sudden temperature increase to about 80ºC. After the temperature stabilizes, the stirplate is turned to full speed and the temperature controller is set to 100ºC. The sample is allowed to de-gas at this temperature for about 1 hour, with occasional pump/purge cycles. During this time some of the reagents will be sprayed up onto the sides of the flask where they can cool and condense, altering the concentration of the reagents in the flask. Using glass wool initially can help alleviate this, keeping the sides above the melting point of the hexadecylamine, or a heat gun can be used to gently heat the sides just before the end of the de-gassing.
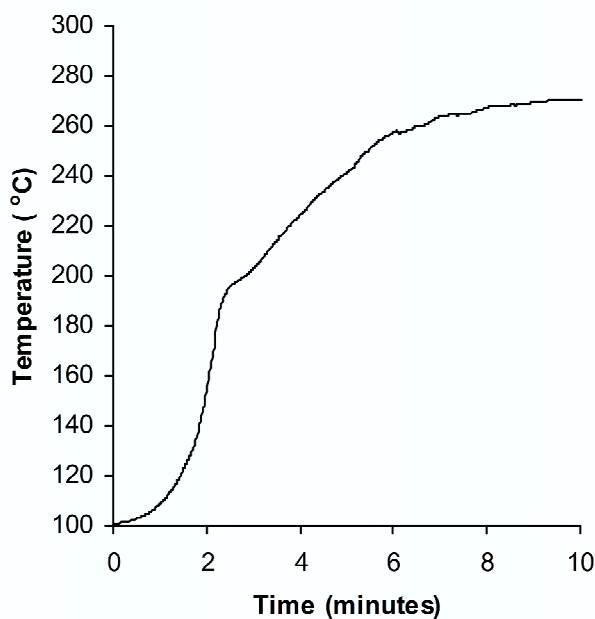
Figure 2.11: In-situ reaction temperature during a synthesis of iron oxide colloidal nanocrystals.

The Schlenk line is then switched over to gas (Ar or N_2) from vacuum. The temperature controller is set to the growth temperature (generally 270°C). The thermal profile can be followed manually or by using a computer output from the controller. Such an output is displayed in Figure 2.11. The temperature increases gradually up to about 130°C, when the cupferronate begins to decompose exothermically. Yellow-brown gas is evoled, strongly resembling NO, accompanied by a subtle change in color of the solution from a red-brown to brown. At about 180°C the solution violently bubbles and the solution changes color from brown to a dark brown resembling the color of chocolate. The steep temperature rise levels off about 190°C , and the nanocrystals stabilize at 270°C about 8 minutes after initially setting the thermal

controller. The nanocrystals are allowed to grow for 5–60 minutes, depending on the final nanocrystal size desired.

At the end of the growth time, the flask is removed from the heating mantle and, especially when smaller nanocrystals are desired, the flask is cooled with forced air. At about 40–50°C, the flask is opened and about 3 mL of toluene is added. This prevents the strong aggregation of nanocrystals in the surfactant solution, particularly in the polymeric byproduct that tends to form at longer growth times. The solution is removed to several vials and centrifuged. The polymeric byproduct settles to the bottom while the nanocrystals primarily remain in the toluene solution phase which is decanted or pipeted away. Some nanocrystals do become trapped in the polymeric phase and can additionally be reclaimed by further addition of toluene and centrifugation. The nanocrystals are precipiated from the toluene solution with addition of a small amount of methanol. The precipitate is redissolved in toluene and the precipitation/dissolution procedure is repeated several times to ensure complete removal of excess surfactant. In the last dissolution cycle, a minimal amount (about $\frac{1}{2}$ mL) of toluene is added and the nanocrystals are preicipitated with acetone rather than methanol. Methanol is immiscible with ethylcyclohexane which is used as a pressure medium, but acetone is miscible with it. The nanocrystals are stored slightly wet which helps preserve their solubility. This is extremely important given the very high nanocrystal concentrations required for good x-ray diffraction signal to noise ratios.
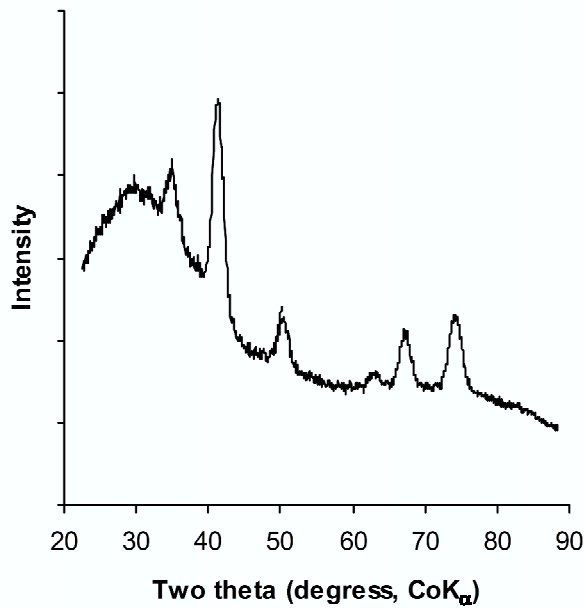
Figure 2.12: Typical x-ray diffraction pattern (XRD) from iron oxide nanocrystals taken on a lab source diffractometer. Broadening of peaks is primarily due to the Debye-Scherrer effect.

2.3.3 Nanocrystal characterization

There are two primary means of post-synthesis characterization of nanocrystals. X-ray diffraction (XRD) is used to assess the crystallinity, structure, and size of the nanocrystals. Transmission electron microscopy (TEM) is used to assess size and size distribution of the nanocrystals.

X-ray Diffraction

A typical XRD pattern is shown in Figure 2.12. This pattern was obtained using a Bruker D8 Discovery equiped with a 2D GADDS detector. This diffractometer has a Co-K_α anode ($\lambda = 1.79026$ Å). Exposure time was 20 minutes for each half of the
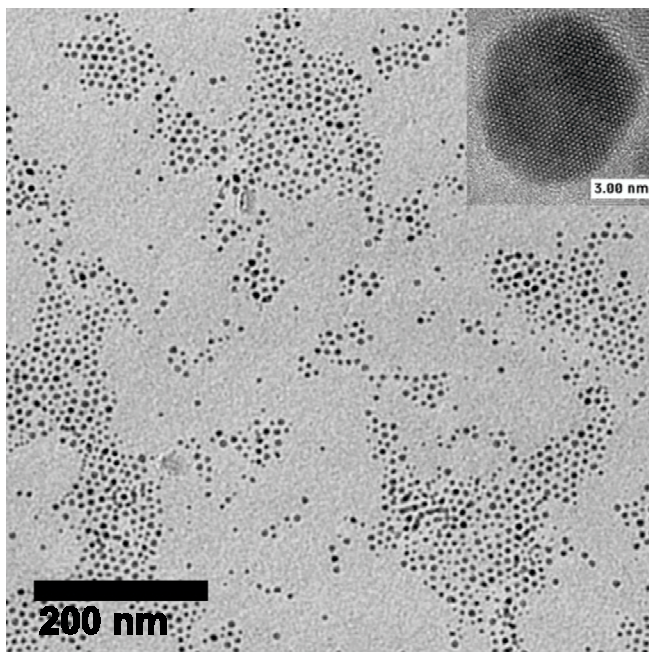
Figure 2.13: Low-resolution transmission electron micrograph (TEM) of iron oxide nanocrystals. This sample is typical of most samples, showing a reasonably narrow size distribution. Inset is a high resolution TEM micrograph of a single iron oxide nanocrystal. No crystalline defects are apparent in the high resolution TEM, indicative of the highly crystalline nature of nanocrystals. HR-TEM courtesy of Erik Scher.

pattern (divided at about 50°). In addition to the instrument function, the diffraction peaks are broadened by the well known Debye-Scherrer broadening phenomenon [41] (see Chapter 1). The pattern is shown without background subtraction to emphasize the difficulty of collecting nanocrystal diffraction data.

Transmission Electron Microscopy

A typical low-resolution TEM of iron oxide nanocrystals is shown in Figure 2.13. As can be seen, the nanocrystals have a moderately narrow size distribution. The size of the nanocrystals determined directly from TEM closely agrees with the size as

determined by the Debye-Scherrer equation applied to the peakwidths of the XRD data. This is substantial evidence that nanocrystals are single-domain structures. The typical nanocrystal has no grain or twin boundaries.

Inset in the figure is a high resolution TEM of a single iron oxide nanocrystal (courtesy of E. C. Scher). While not a routine characterization method, HR-TEM demonstrates the single-crystal nature of the nanocrystals. No grain boundaries or other defects are apparent in the micrograph. The nanocrystals always appear faceted in TEM pictures. It is possible that a careful study of the facet angles might be able to deduce which crystal $\{hkl\}$ planes are exposed at the surface. However, no such analysis has been attempted at the present time.

UV-Visible absorption

Also shown here is the UV-Vis absorption spectrum (Figure 2.14). Such a spectrum would not be taken as a routine characterization step, but is included here for completeness. The sharp increase in absorption above 500 nm gives the solution its brown color. The absorption does not appear to depend on the size of the nanocrystal. This is not particularly surprising since the absorption for iron oxide should be due to localized absorption by the octahdrally and tetrahedrally split Fe^{3+} ions.
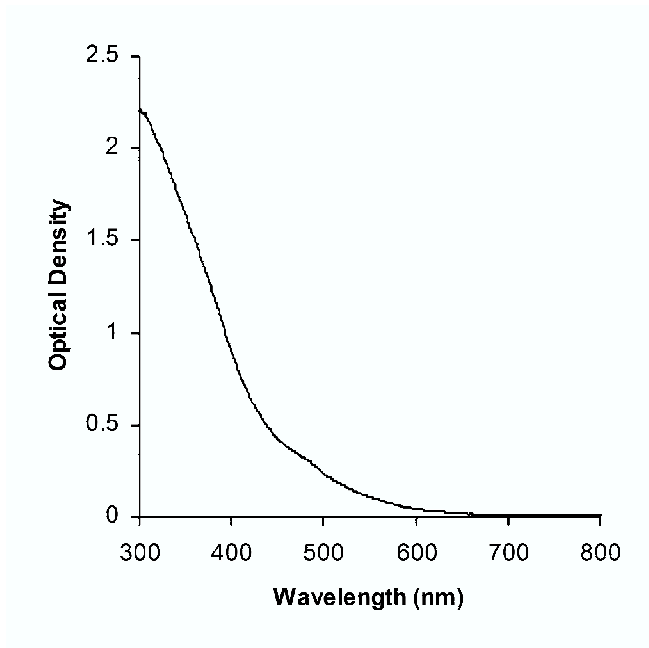
Figure 2.14: UV-Visible absorption spectrum of iron oxide nanocrystals

2.4 Conclusion

This chapter outlines the experimental procedures used to procure the data in this work. Along with the available literature, they should provide the necessary details to reproduce this work. More specific details are given in each chapter, and any deviations from the procedures outlined here are noted therein.

Chapter 3

Development of a dedicated beamline at the Advanced Light Source for high pressure nanocrystal diffraction

The work presented in this chapter is a result of a collaboration with Simon Clark, Kathy Opachich, Rich Celestre, Alastair MacDowell, and Howard Padmore of the Advanced Light Source.

3.1 Introduction

The goal of this work is to study high pressure structural phase transitions in nanocrystals. Such a study requires first the means of producing the enormous pressures necessary for the transitions to occur, and second a means of studying and observing the nanocrystals while under pressure. In the previous chapter the means of obtaining high pressure in the diamond anvil cell (DAC) were discussed. In this chapter, the techniques used to acquire information about the nanocrystals, namely synchrotron x-radiation for diffraction will be discussed.

There are two primary techniques by which high pressure nanocrystal transition have been studied in the past. The first is with visible spectroscopy [11, 12, 9], generally UV-Visible absorption. However, this technique can only be used to determine the extent to which a transition has occurred, or phase percentage, and then only if there is an optical signature for the transition. Such is the case for CdSe nanocrystals, but not necessarily for other, non-semiconductor materials. X-ray diffraction, on the other hand, can generate information not only about the extent of a transition but can also yield structural information and the equation of state. Diffraction data has been used to determine the shape of CdSe nanocrystals in the high pressure phase and, in turn, a mechanism consistent with the shape change of the nanocrystals across the transition [5]. X-ray diffraction has the further advantage that it is generally applicable to any material. Most structural transitions are clear in the diffraction data even if an optical signature does not exist, or is difficult to interpret.

Obtaining x-ray diffraction data at high pressure requires generating sufficient flux through the diamonds which are somewhat absorbent, particularly for x-rays < 20 keV in energy. Also, nanocrystals do not scatter as strongly as bulk materials. For such an application, synchrotron radiation provides an ideal solution. The synchrotron beam is very bright, but it is also tightly focused, and operates at high photon energy. The small beam sizes (generally $\sim$10–100 μm) are about the same size as the sample hole in the gasket of the DAC. The high energy of the synchrotron photons allows one to operate at energies high enough to pass through the diamonds.

Previous work in our group on this project had been conducted at the Stanford Synchrotron Radiation Laboratory (SSRL) on wiggler beamline 10-2. However, that beamline was shared with many diverse users making a permanent endstation for high pressure nanocrystal diffraction impossible. This meant that 1–2 days of beamtime was spent each experiment on set-up. Furthermore, a demand for a permanent high pressure station was deemed to exist because of the large number of high pressure researchers in California.

We therefore set out to prototype a beamline and endstation which could be used for a permanent high pressure endstation at the Advanced Light Source (ALS) at Lawrence Berkeley National Laboratory in Berkeley, California. Recent advances in instrumentation at the ALS have allowed for the construction of "super-bend" magnet beamlines which could produce x-rays of much higher energies than possible on bend magnet beamlines. This chapter will lay out the work done at beamline

7.3.3 to prepare for the installation of a permanent endstation for superbend magnet beamline 12.2.

3.2 Principles of design

The goal of the protype endstation on 7.3.3 was to design an endstation which would allow for the maximum efficiency of data collection when transposed to 12.2. The primary concern was that equal time was spent changing DAC pressure as collecting data, about 20–30 minutes each. For this reason, the design principle for the endstation, as articulated by Simon Clark, was to design a station so that pressure could be changed and monitored remotely. This removed the need to enter and exit the x-ray hutch to get the DAC, find the rubies, change the pressure, re-check the pressure, and re-position and align the DAC in the x-ray beam. Such an "on-line" pressure system would effectively double the amount of beamtime. Furthermore, this would remove the error in sample-to-detector distance created by placement of the DAC on its mount each time the pressure was changed. Finally, such a system would create the possiblity to study kinetics of phase transitions by x-ray diffraction because data could be collected immediately following the pressure change.

Although at the time of this work the on-line system was incomplete, most of the instrumentation and practices were designed around this final goal. This prompted the use of gas-membrane driven DAC's used throughout this work (see Chapter 2) because of the ability to remotely control their pressure.

3.3   Project challenges

A number of challenges present themselves when trying to design a station for high pressure studies. The largest problem is presented by absorption from the diamonds. However, nanocrystal studies at high pressure create additional complications, including weak and diffuse scattering from the nanocrystals. These problems must be born in mind during planning.

3.3.1   Diamond transmission

The first challenge in obtaining diffraction data from within the diamond cell is getting sufficient numbers of x-ray photons through the diamonds. The transmission of x-rays through diamonds, like all materials, increases with energy. Figure 3.1 shows the x-ray transmission though 3.0 mm of diamond (typical pathlength for one diamond) as a function of energy [47]. Generally, diamonds are said to become "transparent" above 10 keV. However, the degree of transparency increases slowly from 10% to 68% between 10 keV and 20 keV. This means that, for 11.1 keV (the typical operating energy on beamline 7.3.3), only 17.5% of the incoming beam passes through the first diamond and 17.5% of the diffracted beam passed through the second diamond.

This large lose, even for relatively high energies of 20 keV, mean that an extremely bright source is needed for high pressure DAC studies. Such a source is available in synchrotron storage rings. The Advanced Light Source has two types of beamlines for
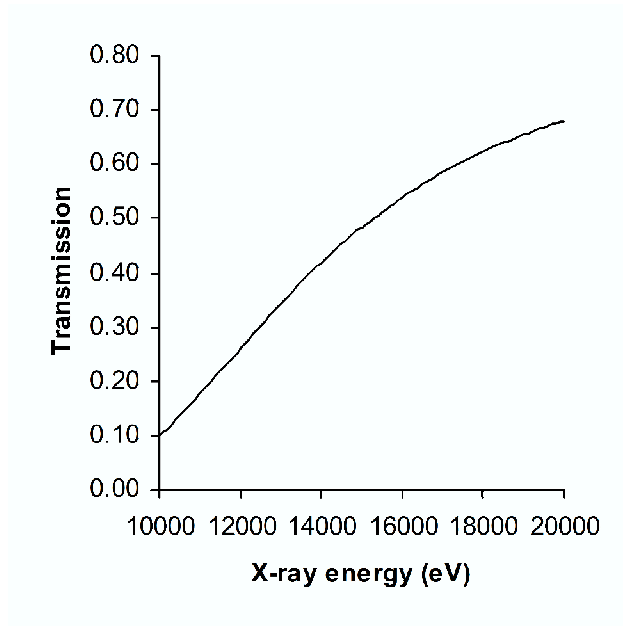
Figure 3.1: Fraction transmission as a function of x-ray energy through 3.0 mm of diamond (density 3.52 g/cm^3). This is a typical pathlength for one diamond. Incoming and as well as diffracted beams will be attenuated to the degree indicated.

this type of work. The first is a 1.4 tesla bend magnet, the other the much stronger 5.0 tesla superbend magnet. The flux for these two magnets is shown in Figure 3.2 [47]. Even for the weaker bend magnet, flux is still several orders of magnitude greater than a laboratory anode source. Because of the combination of the shift to higher energy and the greater initial flux, the superbend magnet at 20 keV can produce 100 times the number of net photons than the bend magnet can produce at 11.1 keV.

3.3.2 Nanocrystal diffraction challenges

Collecting x-ray diffraction on nanocrystals can be difficult. There are two main reasons for this. The first is the small amount of actual inorganic material present in
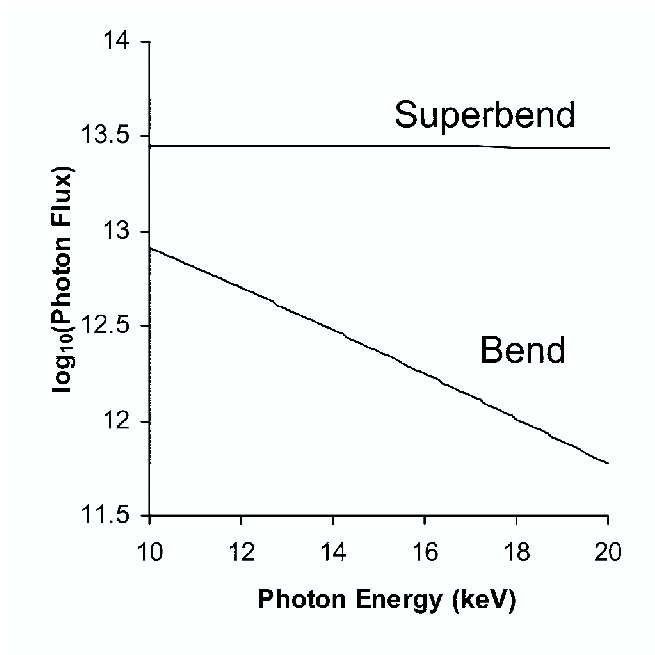
Figure 3.2: Flux as a function of energy for bend and superbend magnet beamlines at the Advanced Light Source. The units of flux are: photons/s/mrad^2/(0.1 % bandwidth)

colloidal nanocrystal samples. As discussed in Chapter 1, nanocrystals are composed of two materials, an inorganic core and an organic surfactant shell which passifies the surface and conveys solubility in organic media to the nanocrystals. Table 3.1 shows the estimated volume percentage of iron oxide in iron oxide nanocrystals. Here the surfactant is hexadecylamine, $NH_2–(n\text{-}C_{16}H_{32})$. Fully extended, as it should be on the surfactant packed surface, this molecule is 35.0 Å long. Assuming a spherical nanocrystal and full surfactant extension, the volume of the annulus of the surfactant is very large compared to that of the nanocrystals, consuming over 97% of the volume of a 3.0 nm diameter nanocrystal.. Furthermore, this is an underestimation of the amount in a real sample because in the DAC the nanocrystals are dissolved in the

NC Diameter (nm)	V/NC (nm³)	V HDA (nm³)	% V Fe₂O₃
3	14.14	510.09	2.77
5	65.45	840.23	7.79
7	179.59	1258.39	14.27

Table 3.1: Table of volume (V) percent of Fe_2O_3 in a single Fe_2O_3 nanocrystal (NC). The remainder of the volume is occupied by the organic surfactant, in this case hexadecylamine. The calculation assumes a spherical Fe_2O_3 particle inside a layer of fully extended (35.0 Å) surfactant.

pressure medium. Even for the extreme case of a nanocrystal-solid this would be an underestimation because the close packed spheres would have some space between them not occupied by either organic or inorganic material.

The second challenge faced in nanocrystal diffraction is the inherent line broadening due to finite size, known as the Debye-Scherrer effect (see Chapter 1, §1.5.2). Debye-Scherrer broadening is both a blessing and a curse. The broadening is inversely proportional to the size of the nanocrystal and can be used to characterize shape and size changes across the transition [5, 6]. However, because this information is important, it is necessary to have a very narrow bandwidth of x-rays. Early in the project, when it became clear that nanocrystals presented a challenge to the available beam intensity, it was proposed that a multilayer crystal be used instead of a double-bounce monochromator. Multilayer crystals increase intensity by about a factor of 10, but at the expense of bandwidth. Thus one of the most useful pieces of data obtained in

this experiment would have been lost, and the idea had to be abandoned.

3.4   The Advanced Light Source and Beamline 7.3.3

The ALS was originally designed for use as a soft x-ray source. As such, unlike the Advanced Photon Source (APS) or the Stanford Synchrotron Radiation Source (SSRL), it is relatively small and operates at a low beam energy. However, with the use of insertion devises (wigglers and undulators) and superbend magnets, the ring can also produce quite high energy photons ($\sim$20 keV). As such, the ALS is able to span the range of infrared to hard x-ray. The characteristic parameters of the ALS are shown in Table 3.2.

Beamline 7.3.3 was originally designed for an ongoing project in microdiffraciton. The biggest requirement was for a very small beam. On any given beamline the beam is smallest closest to the storage ring. As one passes down from the storage ring the beam expands with some characteristic divergence angle. Beamline 7.3.3 was designed to get around this problem by refocusing the beam down to the same size as at the storage ring. Because conventional x-ray optics operate at grazing angles, this ironically requires that the endstation be located far away from storage ring.

A schematic of the beamline is shown in Figure 3.3. The focusing optics consist of a toroidal silicon mirror half way between the storage ring and the endstation.

Beam particle	electrons
Circumference	196.8 m
Radius	31.32 m
Beam energy	1.9 GeV
Beam current	∼200-400 mV
Lowest energy photons	0.002 eV
Highest energy photons	60 keV

Table 3.2: Characteristics of the Advanced Light Source

The position of the focus can be adjusted somewhat within the hutch using the pitch and bend motors. The pitch motor adjusts the angle of the mirror as shown, while the bend motor applies a latteral stress to the Si mirror, increasing the degree of curvature of the torroid.

One drawback for using beamline 7.3.3 for high pressure research is that the Si mirror is coated in platinum to increase its reflectivity. As noted above, for high pressure one would prefer to work at higher energies, but there is a sudden drop in the reflectivity of Pt associated with the L-edge absorption at 11.563 keV [47]. Above this we observe a sudden drop in the intensity of the incoming beam. Thus, the theoretical values for flux given in Figure 3.2 does not match the actual values above 11.563 keV. For this reason, most experiments were done at 11.1 keV ($\lambda = 1.1169$ Å).
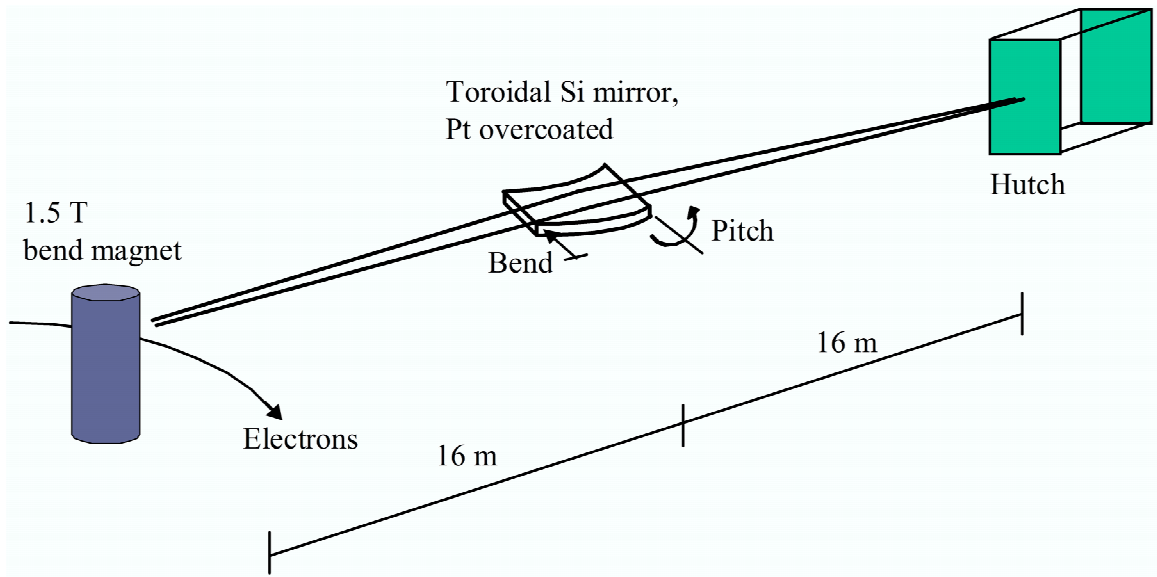
Figure 3.3: Schematic of the design of beamline 7.3.3.

In order to avoid this problem on the new beamline, 12.2 will be installed with a mirror coated with rhodium. Rhodium has no absorption edges, and therefore no decreases in reflectivity, between 10 and 20 keV.

3.5   High pressure endstation

The basic layout of the endstation is shown in Figure 3.4. The entire endstation is contained in the front half of the 7.3.3 x-ray hutch and can be moved aside for microdiffraction experiments taking place in the back of the hutch.

The endstation begins with an x-ray monochromator. Following the monochromator, stray beams and diffuse scattering are mitigated by a series of slits and a collimator. The beam then passes through the DAC. The diffracted beams are col-

To mechanical pump

Turbo pump

x,y slits and
ion chamber

200 µm
Collimator

x,y motor
drives

Shutter

DAC

Image plate
reader

White beam
from ALS

z translation
stage

Double bounce Si crystal
d(111) = 3.135 Å

x,y,z stage

x,y motor
drives

y

x

z
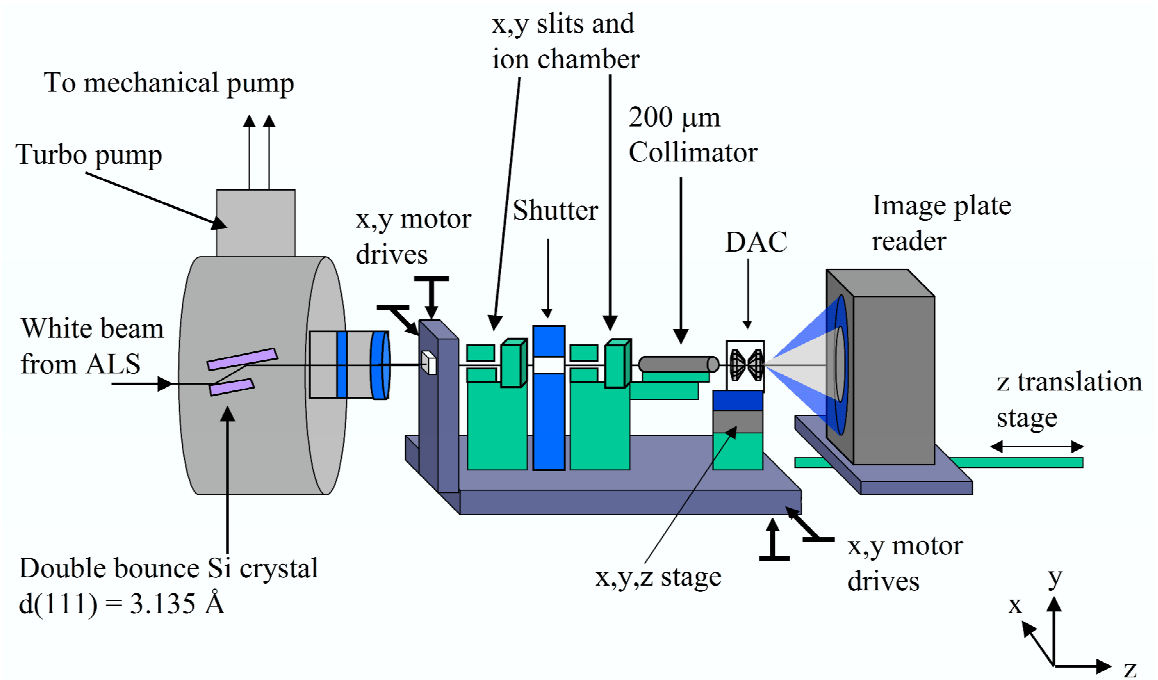
Figure 3.4: Schematic of the dedicated high pressure endstation

lected on a detector, here an image plate reader. From the image plate the data can be read an passed to a computer outside the x-ray hutch. Each portion of the endstation will now be considered in turn.

3.5.1   Monochromator

The endstation begins with the monochromator. Because the refractive index of x-rays in any material is virtually unity for any non-grazing angle, an x-ray monochromator cannot act like a prism. Rather, it is based on Laue diffraction from a single crystal. The best way to consider this is as a variation on the familiar use of the Bragg equation, $n\lambda = 2d\sin\theta$. Usually λ is held constant while d varies as a function of 2θ. In an x-ray monochromator, d is held fixed while λ varies as a function of 2θ. Thus, the angle at which the single crystal monochromator is tilted with respect to the beam will determine the wavelength. Our set-up uses a double bounce Si (111) crystal. This is a dual set of Si (111) crystals mounted parallel to one another. Only one Bragg angle will satisfy both crystals for a given orientation, improving the bandpass ($\Delta\lambda/\lambda$). Also, the outgoing beam will be parallel to the incoming beam but shifted by a distance equal to the separation of the two crystals, which simplifies the set-up.

The Si single crystals are contained within a vacuum chamber. This is for two reasons. The first is that in air the crystals would undergo oxidation under the intense heat generated by the incoming x-rays. The second reason is that, in order to

remove this heat load, the crystals are in contact with a cold finger attached to a close-cycled refrigeration system operating at cryogenic temperatures (the coolant is a proprietary mixture of light hydrocarbons). Without cooling, the bandpass of the monochromator would increase due to the strain create by thermal gradients causing differential expansion of the crystal. Cooling to cryogenic temperatures has the advantage that below between 300 K and 150 K, Si's conductivity increases from 1.48 to 4.09 W/cmK [48] , greatly increasing the amount of heat load that can be conducted away from the crystal surface. In addition, Si's thermal expansion coefficient drops significantly from its room temperature value of 2.49×10^{-6}/K, [48] reaching 0 at 125 K [49].

An experiment was conducted to check the efficiency of cooling in the monochromator. Starting from room temperature, the temperature stabilized at about 123 K after about 3.5 hours, finally reaching 108 K when left to run overnight. The temperature at the crystal always lags behind that of the cold finger by about 10–15 K, but overall there seems to be good thermal conductivity between them. When the beam was turned on for approximately 20 minutes then shut off, the crystal had heated to 117 K. After turning off the x-rays the monochromator cooled back below 108 K within 5 minutes. In the course of normal operations, the beam would typically be on for 20–30 minutes and off for another 20–30 minutes to read data from the image plate and change the pressure. This will also be true on 12.2, though the intervals will be less because of less time needed for data collection and for changing the pressure.

As such, the temperature should be able to maintained between 100–110 K even for the higher heat load on the more intense superbend magnet beamline.

3.5.2 Apertures, DAC and image plate reader

As seen in Figure 3.4 the entire endstation is mounted on a single optics rail except for the monochromator and the image plate. In turn, each component can be aligned independently, but once they are aligned relative to one another, the entire bench can be aligned as a single unit. The optic rail is mounted on a bench which has x and y motors both at the front and back. Note as shown in the figure, the xy plane is that perpendicular to the beam with z lying along the beam, positive in the downstream direction.

The image plate reader used is a Mar345 (Mar Research, Evanston, IL) which has a circular working area with a diameter of 345 mm and a pixel resolution of 100 μm. Because the opening angle in the DAC was 45°, the image plate was generally set approximately 172.5 mm behind from the diamond cell. Thus the image plate was at the furthest distance possible (to minimize solid angle subtended by pixels and thus improve resolution) while still collecting all the available data.

3.6 Calibration

Calibration was a routine part of every experiment, and was often repeated during the course of the experiment. The precision necessary to perform high pressure studies is dictated by the low compressibility of most solids. Values of B_0 often fall between 10–200 GPa. For example, Al_2O_3 has a B_0 of 257 GPa [50], while NaCl has a B_0 of 24.0 GPa [51]. As shown in Chapter 4, the application of 10 GPa of pressure to Fe_2O_3 only reduces the unit cell volume by about 5%. This causes peak shifts of only about $0.32°$. In order to take enough points to determine an accurate equation of state, steps on the order of 1–2 GPa must be taken. In order to beat this step by a factor of ten, a precision of about $0.03°$ is necessary.

There are three pieces of information needed to integrate two dimensional data: wavelength, sample to detector distance and the tilt of the detector with respect to the beam. Outlined below is the procedure for determining each of these.

3.6.1 Wavelength

Wavelength calibration was done by performing x-ray absorption on various foils of metals. The two most often used were copper (K-edge 8.9805 keV), and germanium (K-edge 11.103 keV). The value of the inflection point in the spectrum is reset to the known value of the K-edge. Typically after the calibration with Cu, the Ge edge was within 10 eV of the known value. For most experiments, the wavelength was left at the Ge edge. However, for some experiments where smaller d-spacings were needed,

the calibrated wavelength was then set to 15.000 keV.

3.6.2 Sample to detector distance

The sample to detector distance was determined during each experimental run using a standard sample of Al_2O_3 (NIST) or vacuum annealed LaB_6 (Aldrich). The advantage of LaB_6 was that it scatters more strongly than Al_2O_3 and often produced a diffraction pattern with a higher signal-to-noise ratio. Minimal, non-systematic differences were found between results obtained with either sample. The resulting diffraction patterns were then evaluated using the software package Fit2D [52]. First the detector angle (amount by which the detector is not perpendicular to the direct beam) was accounted for using the TILT routine. The wavelength was fixed at the value obtained from the XAFS calibration discussed above while the sample-to-detector distance was put at some reasonable guess. Once the detector angle was determined, the CALIBRATE routine was used to determine the sample-to-detector distance. In the CALIBRATE routine, all parameters other than the sample-to-detector distance were held fixed, having been previously determined. Once a sample-to-detector distance was determined, the standard pattern was integrated and compared to the theoretical diffraction angle values for that wavelength. If the observed and theoretical values did not coincide within $0.05°$, the calibration was repeated from the TILT procedure. A table of typical calibration parameters is shown in Table 3.3.

hkl	$2\theta_{obs}$	$2\theta_{theory}$	Diff	$(\text{Diff})^2$	%Error
100	15.410	15.418	0.008	0.00006	0.052
110	21.846	21.872	0.026	0.00068	0.119
111	26.885	26.870	-0.015	0.00023	0.056
200	31.137	31.125	-0.012	0.00014	0.039
210	34.945	34.910	-0.035	0.00123	0.100
211	38.366	38.366	0.000	0.00000	0.000

Table 3.3: Typical calibration errors for LaB_6 at 11.100 keV ($\lambda =1.1169$ Å). Shown for each *hkl* reflection are the values observed, values from theory, the difference and difference squared between observed and theory, and the percent error.

3.6.3 Resolution

The term resolution can mean a number of different things. In the case of x-ray diffraction, two types of resolution are important. The first is the ability to distinguish two peaks from one another. This resolution is limited mainly by the bandpass of the monochromator. However, for nanocrystal samples, where the peaks are Debye-Scherrer broadened, this resolution is of less importance (except in determining sizes from peak width, a tricky problem even under the most well characterized conditions). Of greater importance is the accuracy of determination of the location of a given peak. Positional resolution is determined by a number of factors, including the quality of the calibration, the angular resolution of the detector, and the accuracy with which

the DAC is returned to its position after each pressure change.

Error related to DAC placement

It is this later point which leads to the greatest error in our system, (though the limit of the detector is included below for completeness). Following pattern collection the DAC is removed, the pressure is changed, and the DAC is re-placed on the set-up. The DAC is held to the bench by a metal "foot" which fits in a spring-loaded holder on the bench. However, the accuracy of this placement, and therefore the sample-to-detector distance, is likely no better than $\pm$ 25 μm. This error will be random and can be related using the common formula

$$(\sigma_{2\theta})^2 = (\sigma_S)^2 \left(\frac{\partial \tan 2\theta}{\partial S} \right)^2$$

where $\sigma_{2\theta}$ is the uncertainty is 2θ, σ_S is the uncertainty in the sample-to-detector distance, S. The quantities are related by $\tan 2\theta = (l/S)$ where l is the radial distance on the detector of the diffraction peak (see Figure 3.6).

As seen in Figure 3.5, the error in placement is quite large even for small values of uncertainty in S. For 25 μm uncertainty, the uncertainty in 2θ is $0.035°$. In fact, this is approximately the best accuracy we generally observe (see Table 3.3).

Detector resolution

The errors from DAC placement are almost certainly greater than those from the pixel resolution of the detector. The detector resolution may be thought of as a
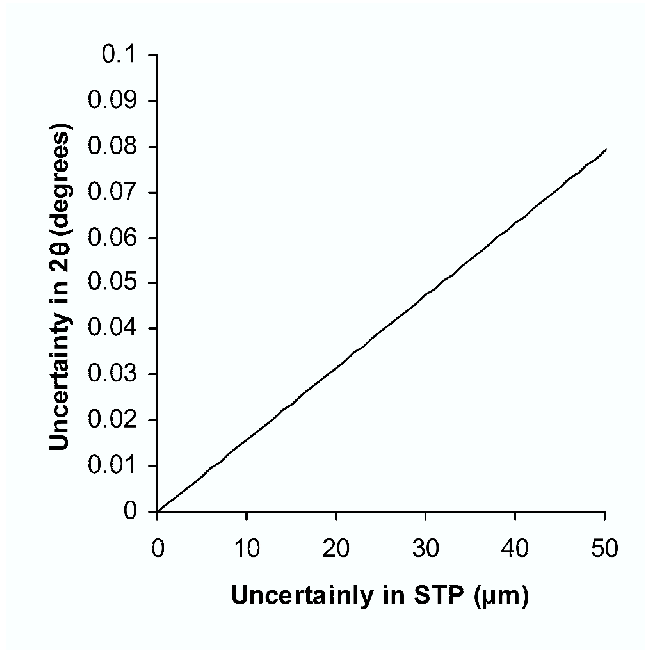
Figure 3.5: Uncertainty in 2θ due to placement error on the set-up. The uncertainty in 2θ is plotted as a function of the uncertainty in the sample-to-detector distance, S. As can be seen, even small error in re-placement of the DAC can lead to large errors in 2θ.
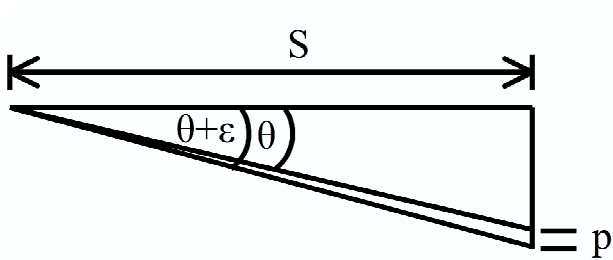
Figure 3.6: Schematic used to determine the angular resolution of one pixel of the detector. The lines diverge from the point of diffraction (the DAC) at the left.

function of the pixel size in the following way (again, see Figure 3.6). For a given S, the angle subtended by a pixel is equal to the difference in angles between a right triangle at a given diffraction angle, θ, and that of a right triangle at that diffraction angle plus a small angle, $\theta + \epsilon$, such that the side opposite is greater in length by one pixel width. Trigonometric considerations lead to the equation relating the angle θ and the detector limited angular resolution (angle subtended by one pixel), ϵ, as:

$$\epsilon = \arctan\left(\frac{S\tan\theta + p}{S}\right) - \theta$$

This function, with typical operation parameters (S = 172.5 mm, p = 0.100 mm), is shown in Figure 3.7. It can be seen that the detector limited resolution at 10° (the lowest angle used in this study) is approximately 0.032°, while at 45° it is approximately half that, 0.017°. No better resolution can be expected at the currently required value of S. These values of resolution agree well with the errors in calibration shown in Table 3.3, indicating that the detector resolution may be a primary source, or at least comparable to other factors, of resolution limit.

Lack of conditioning mirror

A larger S (sample-to-detector distance) could be used by placing the detector further away, but this would also require a higher x-ray energy in order to capture the same range in d-space, which on 7.3.3 is currently an impossibility. This analysis also makes the assumption that all the incoming x-rays are parallel to one another, which may not be true. Most beamlines use a conditioning mirror to assure this
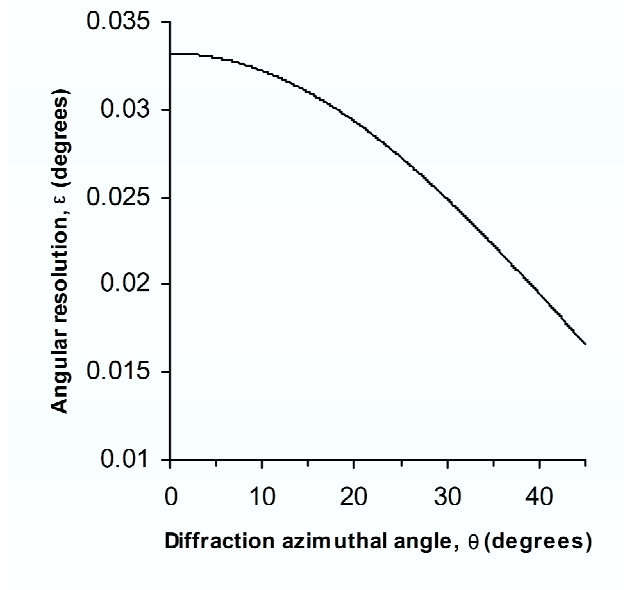
Figure 3.7: Angular resolution of the image plate detector as a function of diffraction angle 2θ. The term "azimuthal" is used here to underscore that this refers to the angle between the diffracted and main x-ray beams.

situation, but 7.3.3 does not have one. Such a mirror is an x-ray optic with an infinite focal length in downstream direction. Because 7.3.3 lacks such a mirror, placing the detector further away may not in fact substantially increase the resolution. This will not be the case on the future beamline 12.2, as its plans include a conditioning mirror in the beamline.

3.7   Nanocrystal x-ray diffraction in the DAC

Figure 3.8 shows three actual diffraction patterns collected at beamline 7.3.3 at high pressure in the DAC. Three different samples are represented, (a) CdSe "nanorods", (b) Co spheres, and (c) post-transition iron oxide (α-Fe$_2$O$_3$) nanocrys-
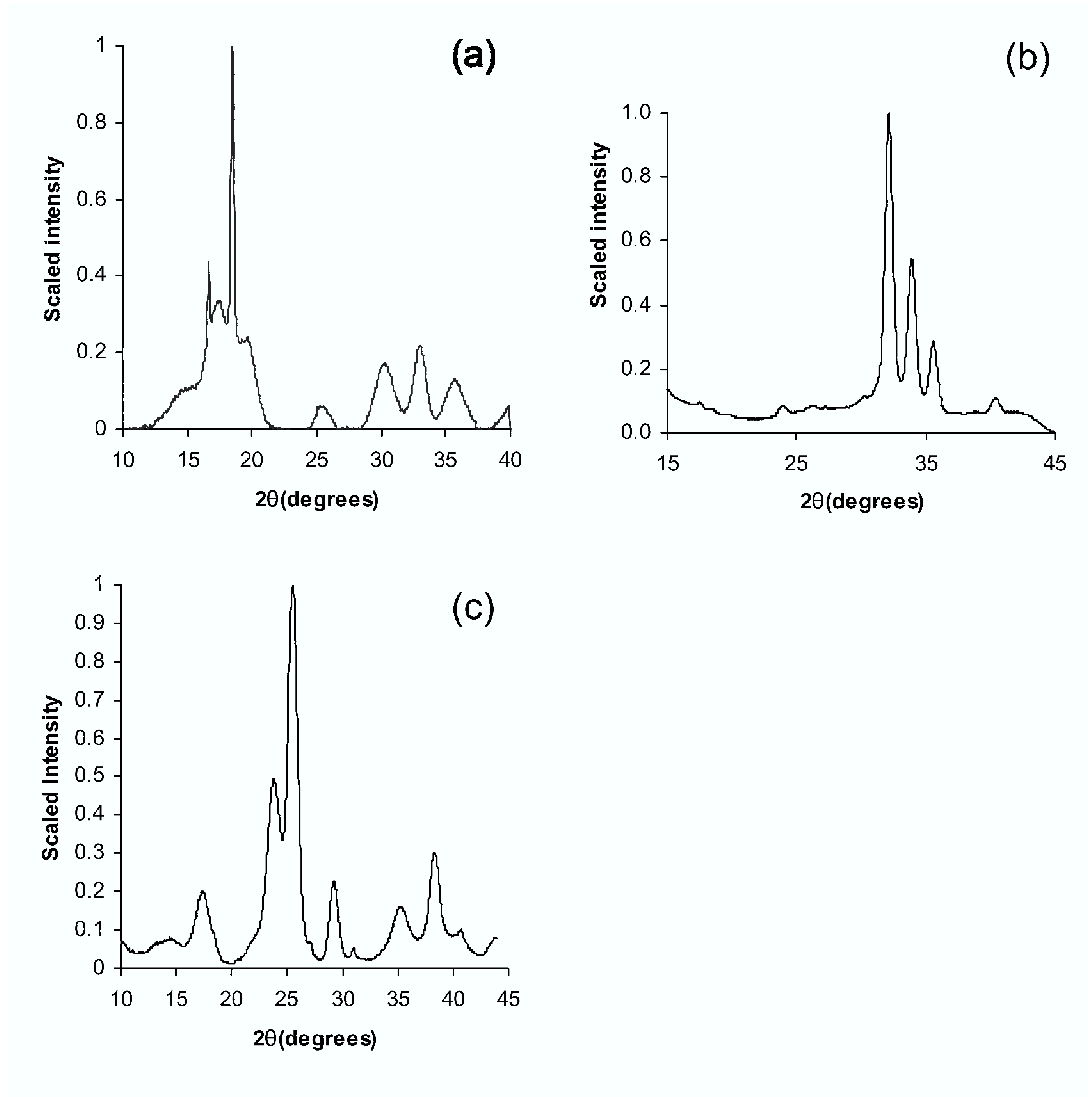
Figure 3.8: Several examples of successful diffraction of nanocrystals in the DAC. Samples of (a) CdSe rods (4 × 40 nm), (b) Co spheres (12 nm) and (c) pressure transformed α-Fe$_2$O$_3$ (7.2 nm). Each of these samples is in the diamond cell and at elevated pressure. These patterns demonstrate the ability to collect high quality data on beamline 7.3.3 in the diamond cell. CdSe samples were provided by Liang-shi Li. Co samples were provided by Victor Puntes.

tals. Each pattern was collected in less than 30 minutes, a reasonable exposure time, and each shows good signal-to-noise. These patterns demonstrate the viability of the current 7.3.3 set-up to collect nanocrystal XRD patterns of high quality in a reasonable time. They also demonstrate the power of XRD is studies of nanocrystal phase transitions. The sharp peak at about 18° in Figure 3.8(a) is the (002) peak of wurtzite CdSe. It is sharper than the rest of the peaks because that it lies along the long axis of the nanorod and so does not show as much Debye-Scherrer broadening. The width of this peak has been used as part of our evidence for nanorod fracture upon transition [6]. The Co spheres in Figure 3.8(b) are in the ϵ-Mn phase. This phase is slightly larger in volume than the usual fcc phase of Co. Attempts to transform ϵ-Co into fcc-Co via pressure and temperature may help elucidate the degree and origin of phase stability of ϵ-Co created by nanoscale effects. Figure 3.8(c) shows the resulting phase of iron oxide from the pressure transformation of γ-Fe_2O_3. Although the peak positions index well to the hexagonal α (corrundum) phase, they do not demonstrate the expected intensities. This gives clues as to the nature of the high pressure phase and the mechanism of transition for $\gamma \rightarrow \alpha$ via pressure (see Chapter 7).

3.8 Conclusion

The x-ray diffraction patterns collected at high presure shown in Figure 3.8 shows, in part, the success of the prototype endstation for 7.3.3. However, that fact alone does not represent true progress since that ability was demonstrated on 7.3.3 in 1998.

The true step forward respresented here is the ability to routinely obtain high precision data quickly with little set-up time and to carry out complete, publication quality experiments. As such, the remaining pages of this work are a more complete testament to the success of this project than these few diffraction patterns alone. The further success of this project will depend on if the leasons learned from the 7.3.3 high pressure endstation have been applied well to the new 12.2 beamline and endstation. However, given the high quality of the data obtained here, and the strong gains from higher energy and flux on a superbend magnet beamline, combined with the leasons from this project, that success seems likely.

Chapter 4

Size dependence of the γ to α structural transition in iron oxide nanocrystals

Much of the content of this chapter has been submitted for publication to *Solid State Communications* [53].

4.1 Introduction

Colloidal nanocrystals may prove to be model systems for the study of pressure-induced structural transitions in solids. Unlike bulk materials, nanocrystals are highly crystalline and lack high-energy defects where transitions may nucleate. Nanocrys-
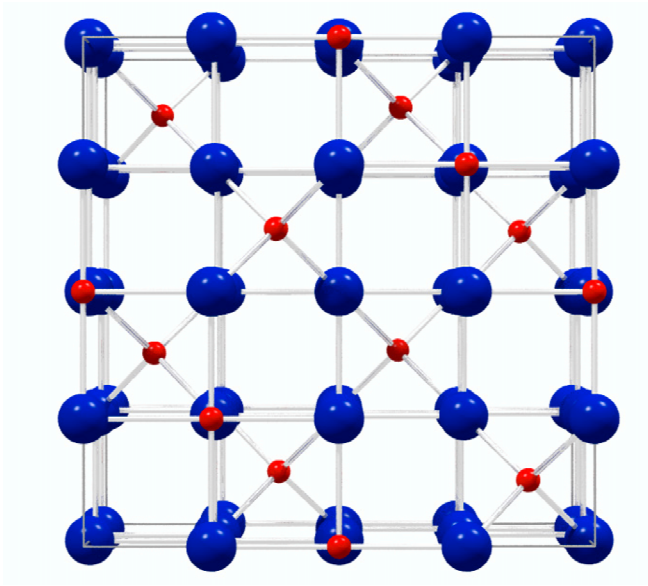
Figure 4.1: Depiction of the γ-Fe_2O_3 structure. It is a cubic inverse spinel stucture (Fd$\overline{3}$m, number 227) with oxygen ions forming a cubic close packed array with Fe^{3+} ions in intersticies. Of the Fe^{3+} ions 2/3 of the are on octahedral sites and 1/3 on tetrahedral sites.

tals of sufficiently small size transform as single domains because each one undergoes a single nucleation event. Chemically synthesized nanocrystals can also be homogeneously dispersed in the pressure medium, reducing aggregation and minimizing particle-particle contact. Early work on pressure-induced nanocrystal transitions was performed on semiconductors [11, 8, 5], while more recent work has turned to the transition metal oxides [20, 54, 18]. These systems are interesting because they tend to be more ionic, they have more complex crystal structures than semiconductors, they can exhibit electronically driven structural rearrangements, and they include many systems relevant to geological studies.

Here we have chosen to study the pressure-induced γ to α transition in size con-
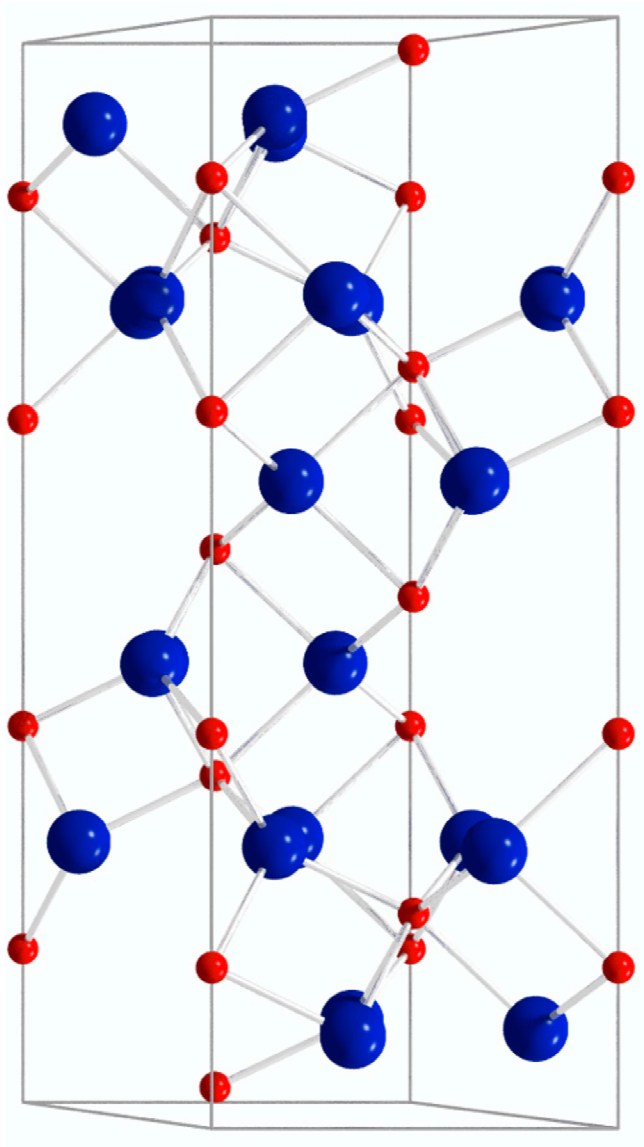
Figure 4.2: Depiction of the stucture of α-Fe$_2$O$_3$. It is a corrundum structure (R$\overline{3}$c, number 167) which, ideally and to first approximation, is a hexagonal close packed array of oxygen ions with iron ions occupying the octadreal intersticies.

trolled Fe_2O_3 nanocrystals. γ-Fe_2O_3 (maghemite) has a cubic inverse spinel structure while α-Fe_2O_3 (hematite) has a hexagonal corundum structure. The two structures are depicted in Figures 4.1 and 4.2. In the bulk Fe_2O_3, α is more thermodynamically stable than γ. High temperature will cause a transition from γ to α [55], and elevated pressure will speed the transformation [56, 57]. Although α is the more stable phase for bulk samples, nanocrystals below 25 nm in diameter form in the γ phase [58]. When heated, γ nanocrystals will transform to α at temperatures between 440 – 550ºC with concurrent particle growth to sizes exceeding 30 nm [59]. These observations are attributed to a higher surface energy for the α phase than for γ. Although the surface energies have not been measured directly, they have for the isostructural Al_2O_3 systems, and the surface energy was in fact found to be 26% higher for α-Al_2O_3 than γ-Al_2O_3 (1.69 J/m^2 versus 1.34 J/m^2) [60].

One would expect the surface energy to also play a dominant role in the pressure-induced γ- to α- Fe_2O_3 transition. Because the α phase is destablilized by high surface energy, the transition pressure would be expected to be higher for nanocrystals than for bulk. The same arguement was made in the case of CdSe nanocrystals to explain the increase in transition pressure as size decreased [12]. In order to assess this arguement, we have choose to study the pressure induced γ- to α-Fe_3O_3 structural transition for a size series of colloidal nanocrystals. Iron oxide nanocrystals have been studied before under pressure [18, 61], but previous experiments have only studied one size of nanoparticle. Such studies do not allow for direct comparison between

nanocrystal systems and may obscure the nano-scale effects at play. This study is made feasible by recent advances in colloidal nanocrystal synthesis which allow for the preparation of nanocrystal with a range of sizes and a narrow size distribution [45].

4.2 Experimental

Nanocrystalline γ-Fe_2O_3 was synthesized in a variation of a published method [45]. Briefly, cupferrone, an oxygen terminated bidentate chealating agent was mixed with $FeCl_3$ in aqueous solution, purified, and then heated along with hexadecylamine under argon. At approximately 200ºC, the iron cupferronate decomposed producing nanocrystalline γ-Fe_2O_3. Samples were maintained at 270ºC for 5 – 40 minutes, during which time the particles grew in size. By quenching the reaction at different times, nanocrystal of 3.2 nm, 5.7 nm and 7.2 nm in diameter were obtained. The final washed particles retained a monolayer coating of the hexadecylamine, making them soluble in non-polar solvents. Samples were evaluated by transmission electron microscopy and x-ray diffraction, both of which yield approximately the same size for each sample, indicating that each nanocrystal is a single crystalline domain. Size distributions for each sample are approximately $\pm$ 15%. Samples of bulk γ-Fe_2O_3 powder (99.9%) were purchased from Aldrich Inc. Three bulk samples were studied, one which was not annealed, a second which was annealed for five days, and a third annealed for two months. Annealing was conducted at 140ºC under vacuum, well below the 300ºC necessary to nucleate α-Fe_2O_3 . Phase purity was confirmed post-

annealing in ambient pressure x-ray diffraction patterns.

High pressure work up to 50 GPa was performed using a diamond anvil cell (DAC) (WCME, Diacell Products Ltd.). Diamonds with 300 mm culet diameter were used with spring steel gaskets with 150 mm holes. Nanocrystalline samples were loaded in the DAC dissolved in ethylcyclohexane and bulk samples were dispersed in the same solvent. Pressure was monitored using ruby fluorescence [25]. All experiments were performed at room temperature.

In-situ x-ray diffraction (XRD) was conducted at the Advanced Light Source, Lawrence Berkeley National Laboratory, Berkeley, CA. Diffraction was collected in the angle dispersive geometry using x-rays of wavelength 1.117 Å calibrated against the Ge K-edge. The beam was focused to a size of 50×120 μm full-width at half-maximum. Two dimensional diffraction patterns were collected using a Mar345 image plate detection system (Mar Research, Evanston, IL). Sample to detector distance was calibrated using LaB_6 and Al_2O_3 standards yielding a system accuracy of approximately 0.03º in 2θ, or 0.005 Å in d spacings. The two dimensional patterns were angle integrated using Fit2D [52] to obtain 1D diffraction patterns. These were fitted with Voigt peak shapes to determine peak position and width. Diffraction patterns were collected at 2–5 GPa increments with typical exposure times of 30 minutes, and were taken at regular intervals of approximately 45 minutes to minimize kinetic effects.
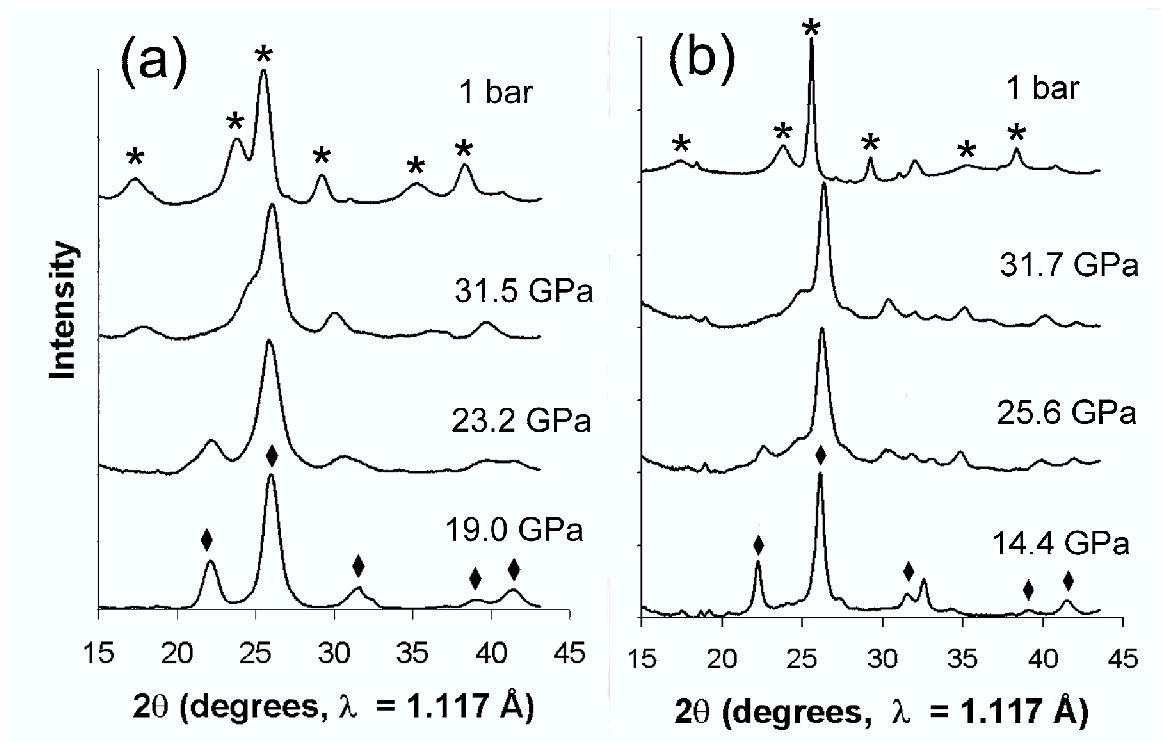
Figure 4.3: X-ray diffraction patterns of briefly annealed bulk (a) and 7.2 nm diameter nanocrystalline (b) γ-Fe_2O_3 at various pressures. Peaks labeled with diamonds are (in order, left to right), the γ (220), (311), (400), (422) and (511). Upon recovery to ambient pressure (topmost patterns), the samples retain the α structure. Labeled with asterisks are (left to right), α (102), (104), (110), (113), (024), and (116).

4.3 Results

Figure 4.3 shows selected diffraction patterns at a number of pressures for 7.2 nm diameter nanocrystals (a) and the briefly annealed bulk γ-Fe_2O_3 (b). The peaks of the nanocrystalline samples are Debye-Scherrer broadened relative to the bulk by the finite size of the diffraction domain presented by nanocrystals [41]. It can be seen that at low pressures only the γ phase was present for both nanocrystalline and bulk samples. As pressure was increased, peaks associated with the α phase began to appear. Finally, at even higher pressures, the pure α phase was obtained. When quenched to atmospheric pressure, both bulk and nanocrystalline samples retained the α structure. The intensity of selected peaks in the α phase was less than expected. These same select peaks were also broader than the other a peaks. This indicates that the a phase obtained by means of pressure is structurally defective as will be discussed in Chapter [**?**]. The peakwidths of the narrowest peaks in quenched bulk α increased from 0.3º to 0.5º across the transition. The peakwidths of the nanocrystalline α are 1.0º, which is the same as those for γ before the transition.

Because some peaks were less intense and broader in the α phase, it was difficult to accurately determine the phase percentages at a given pressure. Following the example of Jiang et al. [18] we quantify the transition progress by plotting the ratio of the integral intensities of the $\gamma(311)$ and $\gamma(220)$ diffraction peaks as a function of pressure. The $\gamma(311)$ coincides closely with the $\alpha(110)$, while the $\gamma(220)$ has no coincident peak in the α phase. As the transition proceeds, the I^{311}/I^{220} ratio increases
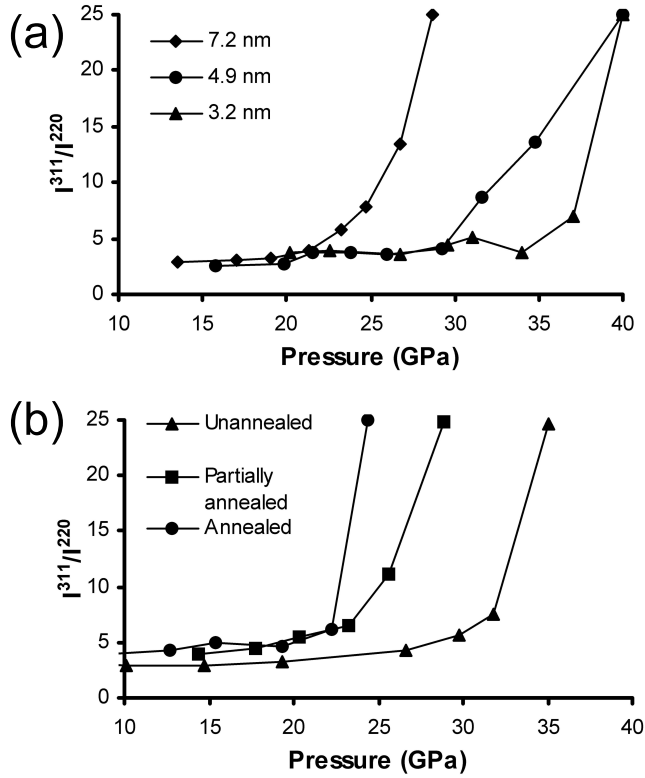
Figure 4.4: The ratio of the integrated intensities of the $\gamma(311)/\ \gamma(220)$ which increases as the transition to α proceeds. The colloidal nanocrystals (a) studied here demonstrate a strong dependence of transition pressure on size. A wide range of transition pressures can be obtained for the bulk (b) depending on how well the samples has been annealed.

from its pure γ value of approximately 3.0.

This analysis is carried out in Fig. 4.4(a) for nanocrystalline samples with diameters of 3.2 nm, 4.9 nm, and 7.2 nm. It can be seen that for decreasing nanocrystal diameters, the rise in the I^{311}/I^{220} ratio associated with the phase transition is shifted to higher pressures. For bulk samples, Fig. 4.4(b), the observed transition pressure decreases as the sample is annealed for longer times.

The unit cell volume for all nanocrystalline (open symbols) and bulk (closed sym-
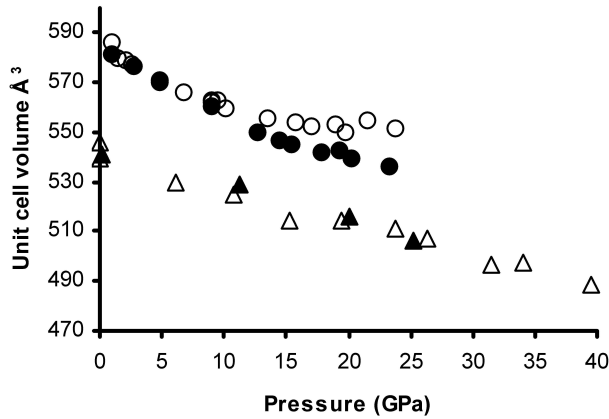
Figure 4.5: The volume as a function of pressure for Fe_2O_3 bulk (closed circles, γ, closed triangles α) and nanocrystals (open circles, γ, open triangles α). Volumes have been scaled to match the number of atoms in the γ unit cell ($53 \frac{1}{3}$).

bols) samples is shown for both γ (circles) and α (triangles) in Fig. 4.5. Nanocrystalline and bulk points have been combined here because no difference has been observed within each sample group. Data are shown only for patterns in which a single phase is present due to the difficulty of determining positions of overlapping γ and a peaks. The approximately 10% decrease in volume associated with the transition can be clearly seen. At low pressures the compressibility of nanocrystals and bulk γ appears to be similar. However, at pressures above approximately 10 GPa their compressibilities diverge. Nanocrystalline samples have a much smaller compressibility than the bulk in this regime. In the α phase, the P-V curves for nanocrystalline and bulk samples appear to be quite similar, although due to experimental difficulties fewer α points are available.

4.4   Discussion

Bulk transitions can be difficult to study because of crystalline defects and domain fracture incurred during a transition. As can be seen in Fig. 4.3(b), the peakwidths for the bulk sample increased across the transition. This presumably indicates that the bulk fractures into smaller domains, introducing grain boundaries into the system. No such domain fracture is evident for the nanocrystals as their peakwidths are virtually unchanged. The importance of sample crystallinity is underscored by the data in Fig. 4.4(b). The transition pressure for the bulk samples is highly dependent on the degree of annealing, and thus the number of defects present. It is interesting that here while grain boundaries generally lead to reduced transition pressures by providing high energy sites for nucleation, they do not do so here. The sample with fewer grain boundaries in fact transforms at the lower pressure. The apparent importance of grain boundaries in determining the transition pressure makes any comparison between bulk and nanocrystal transition pressures tenuous. Nanocrystals lack these grain boundaries, both before and after the transition.

In order to determine the nano-scale effects, one must evaluate a size series of nanocrystals. In Fig. 4.4(a), this comparison is done. It can be seen that as size is decreased from 7.2 to 3.2 nm, the transition pressure increases by more than 10 GPa. This indicates that, when grain boundary effects can be excluded, the effect of reducing the size of iron oxide crystals to the nano-scale is to elevate the transition pressure. It should be noted, however, that the lack of hysteresis data makes any analysis of this

data more difficult. Previous studies involving CdSe nanocrystal [11, 8, 9] have relied heavily upon the hysteresis width, and not merely the upstroke transition pressure, to demonstrate kinetic effects, the lack of grain boundary effects, etc: In this study, however, Fe_2O_3 does not back transform to the γ phase. As such, it is an assumption that the observed transition pressure alone can be used to understand the nanoscale effects in this system, but seemingly not an untenable one.

The γ to α transition is kinetically controlled. At ambient pressure and temperature the free energy change of the transition, ΔG, is -31 kJ/mol or -0.32 eV/formula unit of Fe_2O_3 [55]. In spite of $\Delta G < 0$, the transition is generally not observed without elevated temperature or pressure. A direct energetic calculation is difficult, but, as pointed out by Jiang et al. [18], some insight may be gained by using classical nucleation theory [62]. This theory assesses the stability of a homogeneous spherical nucleus of a daughter phase based on both the difference in free energy and the interfacial energy between the daughter and parent solid phases. From these assumptions, it can be shown that the free energy of formation of a stable nucleus, ΔG^* is

$$\Delta G^* = \frac{16}{3}\pi\frac{\gamma^3}{(\Delta G)^2}$$

where γ is the interfacial energy and ΔG is the free energy difference between the two phases. A transition will be observed when ΔG^* is on the order of the thermal energy, $k_B T$. This can be achieved either by increasing the temperature or by lowering ΔG^*. Because ΔG^* depends on $(\Delta G)^2$, small changes in ΔG may lead to large changes in the observed transition pressure. Therefore, although nucleation
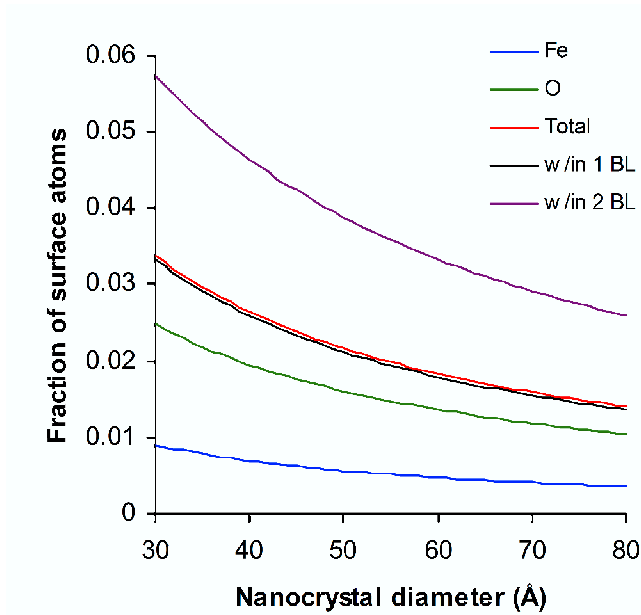
Figure 4.6: The number of atoms as a function of size within one atom (black) and two bond lengths (purple) of the surface for a γ iron oxide nanocrystal. The bond length in γ is 2.0825 Å. Shown also are the number of Fe atoms (blue) and O atoms (green) within one atomic diameter of the surface. The O atomic diameter is 2.70 Å, that of Fe is 1.34 Å. The red line is a summation of the blue and green lines, demonstrating the equivlilence of calculations.

is a kinetic process, it is necessary to consider the thermodynamic free energy.

For nanocrystals, the ΔG becomes influenced by the presence of a significant number of surface atoms. Assuming a spherical nanocrystal, 1.5 – 3.0% of the atoms are within one bond-length of the surface for the sizes studied here (Figure 4.6). Since the nanocrystals are faceted, these values are a lower bound to the number of surface atoms. As discussed earlier, the surface energy should be much higher for α than for γ. If this is true, then as particle size is decreased ΔG would become smaller in magnitude (less negative). This in turn would lead to an increase in ΔG* and an

increase of observed transition pressure.

The nanocrystals studied here demonstrated a similar decrease in compressibility to that observed previously [18]. As can be seen in Fig. 4.5, the bulk and nanocrystalline systems show very different P-V behavior in the γ phase with the nanocrystals having a much reduced compressibility above 10 GPa. This effect may have a number of sources, including a transition to a closely related and unresolvable structure which is much less compressible. However, ionic effects or the effects of transition medium, which becomes less hydrostatic above 10 GPa, may also be the cause.

This decrease in nanocrystalline compressibility was used by Jiang et al. [18] to argue that nanocrystals should transform at pressures lower than bulk. The decreased compressibility results in a larger change in volume across the transition for nanocrystals relative to bulk. Since $\Delta G = \Delta U + P\Delta V - T\Delta S$, the magnitude of ΔG would be increased because $\Delta V < 0$. This argument is difficult to assess because, as we have shown, it is difficult to compare nanocrystals to bulk. Furthermore, we observe that the transition pressure decreases with increasing size. This implies that it is the surface energy effect and not the volume effect which predominates.

In the future, the role these two forces play in determining the transition pressure might be better elucidated by studying larger nanocrystals. It may be that for some larger sizes the compressibility effect will become more important than the surface effect. At that point the transition pressure would in fact decrease as size decreases as predicted by Jiang et al. [18] It would also be interesting to study nanocrystals larger

than the critical size necessary to form multiple domain upon transformation. The transition pressure for nanocrystals above this critical size might be very different than for those below it, giving insight into the role of defect formation in determining the transition pressure.

4.5   Conclusion

In this study we have demonstrated that, in spite of the increased transition volume change for iron oxide nanocrystals, the transition pressure is shifted to higher pressure for increasingly smaller nanocrystal sizes. This trend is best explained by the increasing importance of the positive surface free energy change for smaller nanocrystals. This highlights the importance of studying a size series of nanocrystals in order to understand nano-scale effects.

Chapter 5

Nanocrystalline TiN based ultra-hard composites under hydrostatic pressure

5.1 Introduction

Diamond is the hardest substance known. Diamond has an extreme resistance to deformation, and, by definition of the Mohs scale of hardness, will scratch any other material. Its hardness is due to the three-dimensional support structure provided by its tetrahedral bonding geometry and to the strength of the carbon-carbon bond. Because of their hardness and thermal stability, diamonds are used for such applications as tips for petroleum exploration drill-bits and, as seen in this work, for the

production of megabar pressures in diamond anvil cells.

However, diamonds have a number of drawbacks. They are costly and difficult to deposit as thin film coatings. Also, because carbon alloys with iron at high temperature, it is impossible to use diamond for the machining of steel. For these and other reasons, much attention has been focused on trying to discover new so-called "ultra-hard" coatings which would have hardnesses on the order of diamond [63]. Considerable attention has been paid to thin films of titanium nitride (TiN). Even though TiN assumes the cubic rocksalt structure, usually associated with strongly ionic compounds, the bonding is in fact highly covalent, just as in diamond. [1]

While thin films of TiN and other metal-nitrides and metal-carbides have proven to be quite hard, their hardness can be greatly enhanced by preparing the films in such a way as to precipitate nano-scale domains of TiN [64, 65, 66]. Systems of TiN nanocrystallites separated by thin layers of Si_3N_4 or BN have been shown to have Vicker's (diamond indentation) hardness values from 40 to 100 gigapascals (GPa), comparable to that of diamond, 70–100 GPa [66]. However, the exact origin of high hardness in these materials is not fully understood. The tests performed to determine hardness are essentially empirical techniques, measuring indentation depth as a function of load with a diamond tip. The results of these measurements are a convolution of many different properties of the material. Observed hardness values

---

[1]As in other metal-nitrides and carbides, the Ti atoms remain close packed with N atoms found in intersticies. Bonding is through overlap of Ti d-orbitals and N p-orbitals. The Ti–N bond is comparable to the C–C bond in strength (Ti–N is 476 kJ/mol, C–C is 347 kJ/mol, though the bondlength is longer for Ti–N, 1.84 Å versus 1.54 Å for C–C).

are often the result of defect propagation in the material. Seemingly, such defects would be hindered from propagating in a nano-structured material, as is the case for cold-worked steel (Hall-Petch effect) [67]. But in the case of cold-worked steel, the domains themselves become unstable to slippage at grain boundaries below a certain size ($\sim$10 nm). For TiN based nanocomposites this is not the case. Hardness is still very high for even the smallest domains of 3.5 nm [65].

One way to begin to unravel the origin of high hardness in these materials would be to independently measure the constiuent moduli — bulk, Youngs, and sheer. A strong enhancement in one might help explain the nano-scale effects which are causing the high observed hardness. One possibility is an increase in bulk modulus as has been observed for some metal oxide nanocrystalline materials [18, 20]. Alternatively, orientational effects may enhance the Young's modulus, or the nano-scale structure may prevent defect migration. Another phenomenon with poorly understood effects on the hardness is the nature of strain in the crystallites. Unlike the nanocrystals studied elsewhere in this work, the TiN nanocrystals are strongly connected to one another and changes in one crystallite will affect those around it.

In this study, we have measured the bulk modulus of TiN nanocrystals in composite thin films. Experiments were conducted in a diamond anvil cell (DAC) up to 50 GPa under quasi-hydrostatic conditions using synchtron x-ray diffraction to for a series of samples of TiN/Si$_3$N$_4$ and TiN/BN nano-composites. Samples were supplied by our collaborators in the research group of Stan Vepřek of Technical University Mu-

nich. These materials are nanocrystalline TiN separated from one another by a few atomic layers of Si_3N_4 or BN (FIG. 5.1). They are made by chemical vapor deposition (CVD) in which precursor molecules are flowed over a hot sample stage. The precurors break down at the hot stage and phase segregatation occurs through spinodal decomposition. This process is diffusion limited and leads to TiN crystallites of sizes from 3–30 nm. (An excellent source for the kinetics of diffusion and their relation to spinodal decomposition can be found in the book by Schmalzried [68].)

Two experiments were conducted on different sample sets. Experiment I was designed to determine the equation of state of the TiN nanocrystals in the nanocomposites in order to see if the compressibility of nanocrystalline TiN was different from that of bulk TiN. Experiment II sought to further investigate the role of strain in these films while under hydrostatic pressure.

5.2   Experimental

Details applicable to these experiments are given in Chapter 2. Only a brief outline of the procedure is given here.

All samples were studied up to 50 GPa at ambient temperature in a DAC (WCME, Diacell Products Ltd.) mounted with diamonds of 300 μm culet. Gaskets of spring steel were pre-indented then drilled with a 150 μm hole. Flakes ($\sim$30 μm in size) of samples (previously removed from their substrates) were loaded in the gasket hole along with a few chips of ruby to be used for in-situ pressure calibration [25]. Ethylcy-
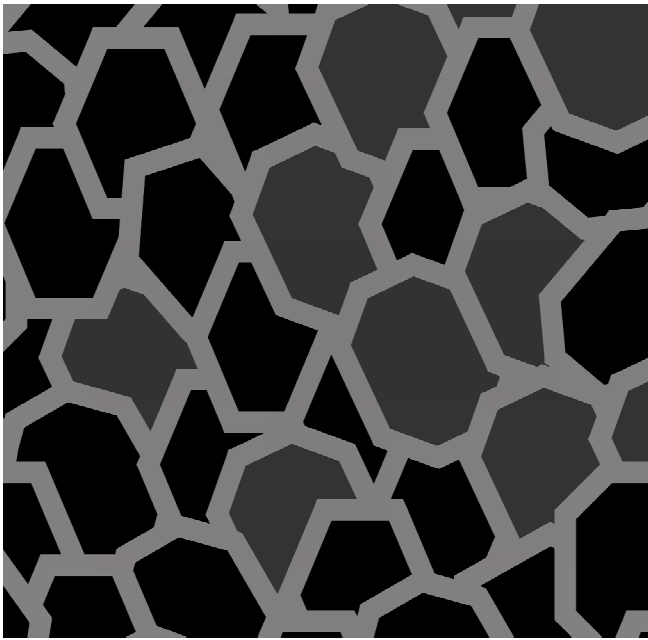
Figure 5.1: Schematic diagram of the structure of TiN-Si$_3$N$_4$ nano-composite materials. Nanocrystals (5–30 nm)of TiN are formed by phase segregation brought on by spinodal decomposition. Dark portions represent TiN, the lighter portions Si$_3$N$_4$ or BN.
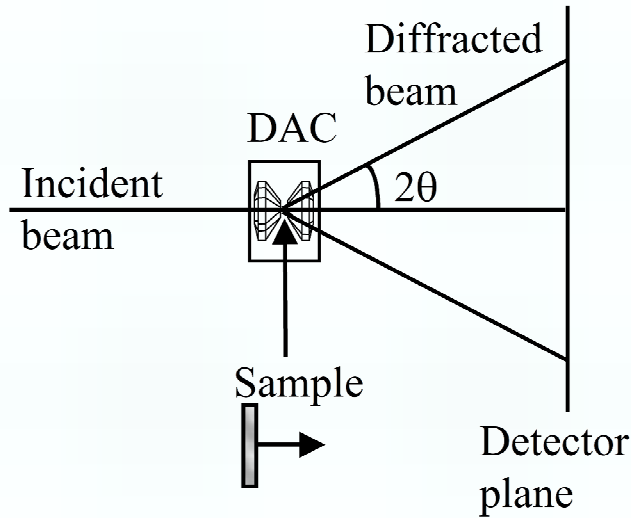
Figure 5.2: Geometry of x-ray diffraction collection. The diamond anvil cell is placed with anvils perpendicular to the incident beam. Upon compression the sample films line up with the anvil faces so that the surface normal is roughly parallel to the incident beam. As such, the angle between the surface normal and the diffracted beam, ψ, is equal to the scattering angle, 2θ.

clohexane was used as a pressure medium, which we have found to have hydrostaticity similar to that of 4:1 methanol/ethanol. A drop of ethylcyclohexane was placed in the gasket hole, then the cell was sealed and pressurized. Upon sealing, the sample flakes would generally pack such that their surfaces were parallel to the culet face of the diamonds. In our geometry, this placed the surface normal of the films parallel to the incoming x-ray beam.

In-situ x-ray diffraction was conducted at the Advanced Light Source (Lawerence Berkeley National Laboratory, Berkeley, California), on bend-magnet beamline 7.3.3. Diffraction was collected in the angle-dispersive geometry (FIG. 5.2). Monochromatic x-rays were obtained from a double-bounce Si(111) monochromator. The x-ray wavelength was calibrated by conducting x-ray absorption on copper and germanium foils

and then set to 0.8266 Å. Two dimensional diffraction patterns were collected using a Mar345 image plate (Mar Research, Evanston, Illinois). The sample-to-detector distance was calibrated with LaB_6 and Al_2O_3 standards. Detector resolution was $0.03°$ in 2θ. Typical collection times were 20–30 minutes per pattern.

Diffraction patterns were angle integrated using Fit2D [52] and fit with Voigt peak shapes. Peaks were assigned to the rocksalt structure, the usual phase of TiN. Individual peak positions were converted to d-spacings using the Bragg equation, and then converted to lattice constants using the following relationship, valid for cubic structures [69],

$$a_\circ^{hkl} = d(\sqrt{h^2 + k^2 + l^2})$$

Unit cell volumes were calculated by simply taking the average of the cube of the lattice constants ($V = \langle (a_\circ^{hkl})^3 \rangle$).

The samples used in Experiment I are listed in Table 5.1. These were synthesized on a thin steel substrate which facilitated their removal, but made diamond indention results difficult. For this same experiment, a sample of bulk TiN powder (99%, Aldrich) was used for comparison with the nano-composite materials. This powder was annealed for 100 hours under vacuum at 250°C in order to relieve any strain present.

Samples used for Experiment II are listed in Table 5.2. The harndess of these samples had been better characterized because of improved methods of separating the samples from thick substrates. For Experiment II an annealing experiment was

Sample	Vickers Hardness (GPa)	Young's modulus (GPa)	Crystallite size (from XRD, nm)
021000	40	200-400	23
261000	30	150-250	5
251000	30	150-250	5

Table 5.1: Samples used in Experiment I. Indentation characterization was difficult on these samples due to the need to produce on a substrate from which the samples could be readily removed. The values for 261000 and 251000 are only estimates from analogy with previous samples, not measured values. Values for size are determined from XRD line-widths using the Debye-Scherrer formula.

Sample	Vickers Hardness (GPa)	Young's modulus (GPa)	Crystallite size (from XRD, nm)
HF140502	25.7 ± 2.3	200-400	21.1
HF220702	30.4 ± 1.9	150-250	10.8
HF230702	42.0 ± 2.9	150-250	8.0
Pro210302	26.8 ± 1.9	249	17.7

Table 5.2: Samples used in Experiment II. Values for hardness and Young's modulus are from diamond indentation measurements. Crystallite size here are determined using the Warren-Averbach method.

also conducted on one sample, HF140502. After pressurization to 50 GPa the cell was quenched to ambient pressure. The sample was found to adhere strongly to the gasket after pressurization. Gasket and sample were removed from the DAC and placed in a tube oven under flowing argon at 700°C for two hours. Diffraction was collected on the post-annealed sample using the same diffraction set-up as before.

5.3   Experiment I: Comressibility comparison

The results presented in this section were submitted for publication to *Material Science Engineering A* [70].

5.3.1   Results and Discussion

Figure 5.3 shows the experimental pressure and volume points obtained on three nano-crystalline samples and on a powder sample of bulk TiN. The nano-crystalline and bulk samples all show remarkably similar compressibility, certainly nothing of the order that would explain the extremely high hardness of these materials relative to bulk. In fact, if anything, the nanocrystalline samples may be slightly more compressible than bulk (smaller value of B_0).

The bulk modulus at zero pressure, B_0 was obtained by a fit to the first order ($B_0' = 4$) Birch-Murnagham [16] equation of state (see § 1.3.2) using the program EOSFit [71, 72]. The results are shown in Table 5.3. All samples have the same
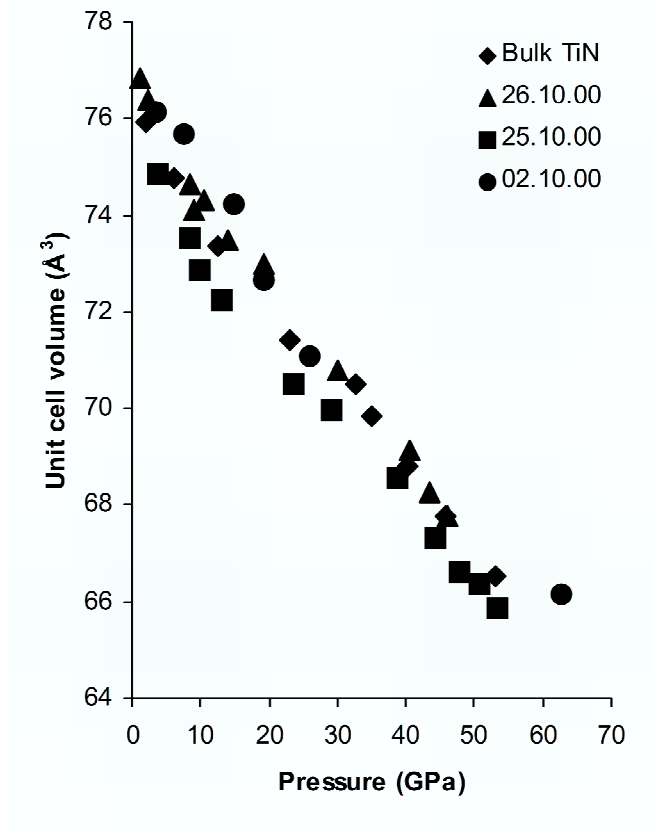
Figure 5.3: Volume as a function of pressure of the TiN unit cell for three nanocrystalline samples and a bulk powder sample. The small compressibility differences between the samples is not sufficient to account for the greatly enhanced hardness of the nanocrystalline samples.

Sample	B_0 (GPa)	$V_0(\text{Å})$
261000	285 ± 7	77.15 ± 0.04
251000	281 ± 14	75.75 ± 0.13
021000	299 ± 33	77.14 ± 0.20
Bulk powder	302 ± 9	76.42 ± 0.04

Table 5.3: Values obtained by fitting to the Birch-Murnagham equation of state.

compressibility within the limit of error, though the nano-structured samples tend to be clustered at smaller values, ignoring 021000 which has a very large error. However, the numerical differences may be partially an artifact of the fitting routine. The program places a larger weight on the lower pressure points, because for these points the pressure is known more accurately (estimated pressure error of $\pm$ 5%). It is at these lower pressures where the samples display the largest dispersion in values. At higher pressures, where the values seem more convergent, the points are weighted less in the fitting.

Experiments conducted by other researchers determined independently the Young's modulus (E) and the sheer modulus (G). Both were determined using surface Brillioun scattering [73], and the Young's modulus was additionally verifed using the vibrating reed technique [74]. The values obtained were E = 445 ± 20 GPa and G = 195 ± 15 GPa. These materials are generally evaluated using diamond indenta-

tion which yields hardness and elastic modulus calculated from the unloading portion of the load-indentation depth curve near maximum load. The value of the elastic modulus determined in this way, E_{ind}, was 242 ± 25 GPa. The discrepancy is due to the manner in which E_{ind} is determined. It is generally assumed to be a linear extrapolation from the high load portion of the load-indentation curve However, at this point the response is a convolution of the hardness of the composite/diamond pair and the distribution of stress under the diamond tip for materials whose hardness approaches that of the diamond indentation tip.

What remains is the question of why the hardness of these materials is so enhanced. Our experiments show clearly that it is not due to a pronounced decrease in the compressibility of the material. This implies that the inter-atomic potential is not being modified by some nano-scale effect. Rather, it seems that the nano-scale structure of the material is responsible, in one way or another, for the extremely high hardness values observed.

5.4 Experiment II: Strain in TiN/BN nano-composites

The results presented in this section will be the subject of a paper in preparation [75].
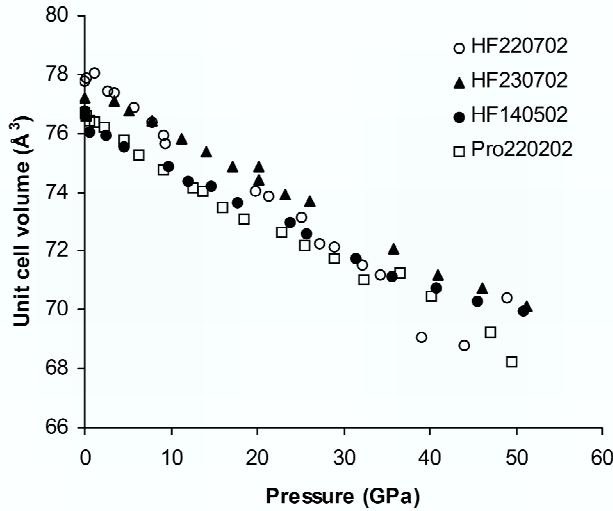
Figure 5.4: Volume as a function of pressure for three nanocrystalline samples and one sample of pure TiN prepared by CVD as listed in Table 5.2. The compressibility differences between the samples cannot account for the elevated hardness of these materials.

5.4.1 Results and discussion

Compressibility revisisted

A similar experiment to that carried out in Experiment I to compare the compressibility of nano-structured samples with that of bulk was also carried out for the new samples. Figure 5.4 shows the volume as a function of pressure for all samples studied. For the most part, these samples show the same behavior as those in the previous experiment. Again, no phase transition was observed and the samples all retained their cubic structure. The compressibility of the nano-structured and bulk samples are relatively similar. Samples HF220702 and HF230702 appear to have a larger V_0 than HF140502 or the bulk sample, but the two V(P) curves parallel

one another very well up to about 20 GPa. Above 20 GPa, the compressibility of HF220702 seems to increase, but that of the other samples remains essentially the same as before.

However, in light of the results presented below, these values should be regarded with some circumspection. Here, the unit cell volume is calculated as the average of the volumes, and hence the lattice constant, obtained from all five (hkl) peaks. Because there is a wide dispersion in the values of a_0^{hkl}, the deviations in $V(P)$ for the nanocrystal samples may be due in part to strain.

Bi-axial strain:Experimental

The value of the lattice constant was found to have a much greater spread than the resolution of the system. The lattice constants derived from each (hkl) reflection by solving the Bragg equation are presented in Figure 5.5 for all four samples studied. The dispersion between the values are quite large. While this phenomenon has been observed before in films at ambient pressure, dispersions of 0.01 Å are more typical. Only the least strained sample in this study, HF140502, has a comparable dispersion between these peaks, and then only at 2.5 GPa (FIG. 5.5). Sample HF230702 has a dispersion covering approximately 0.06 Å at similar pressures. The amount of dispersion increases as pressure is applied.

This type of dispersion has been observed before for TiN thin films [76, 77, 78] and has been interpreted as the result of tensile stress in the plane of the film. Generally,
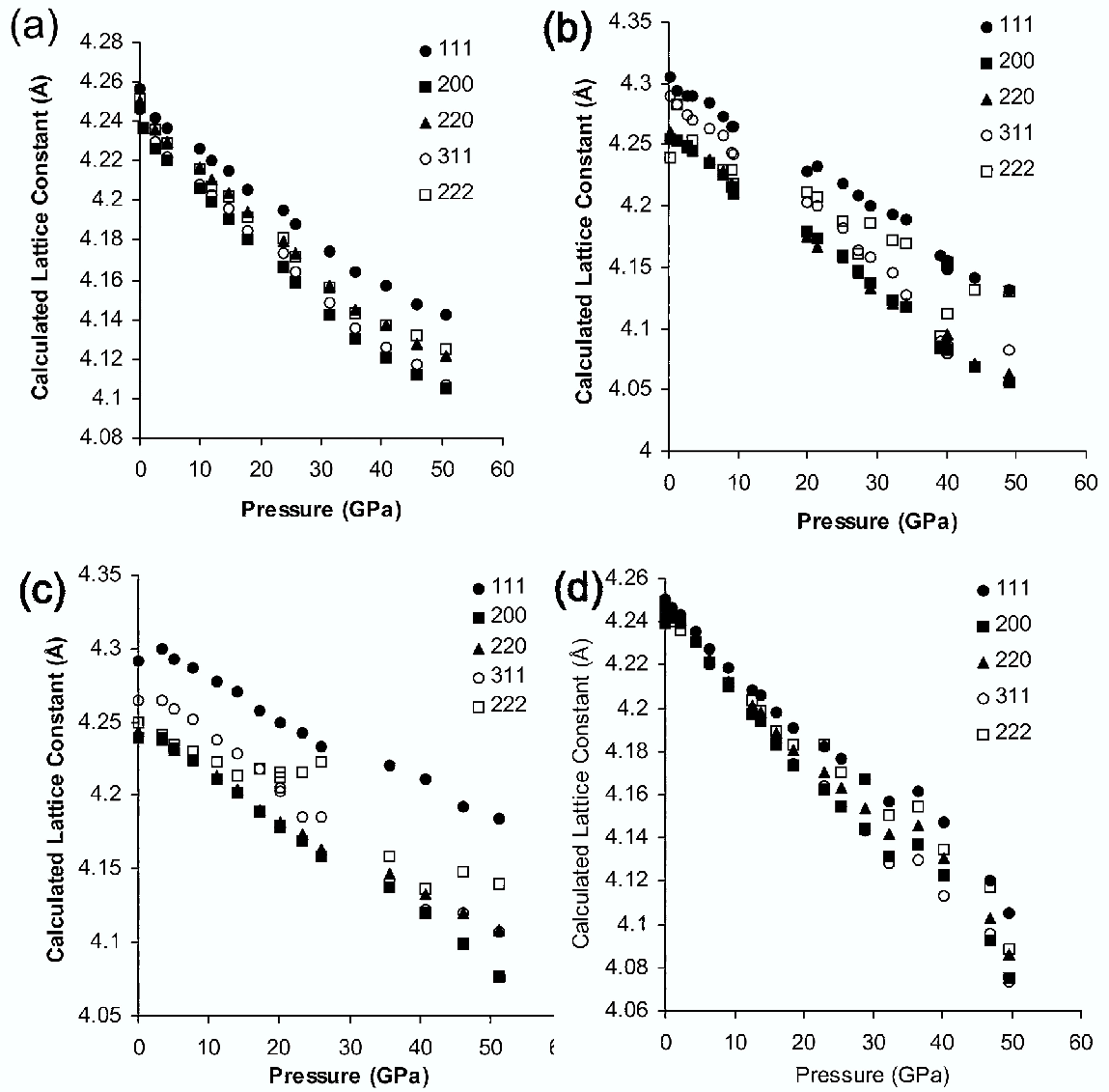
Figure 5.5: Lattice constants derived from each *hkl* peak as a function of pressure for four samples, (a) HF140502, (b)HF230702, (c) HF220702, and (d) Pro210302 (bulk).

the strain is analyzed by taking diffraction patterns at different values of ψ, the angle between the diffracted x-ray beam and the surface normal. However, our geometry is restricted to $\psi = 2\theta$.

5.4.2 Bi-axial strain: Fit to model

In order to better understand the strain present in the film, the data for the least strained nano-composite system, HF140502, were fitted using the model of Rafaja et al. [78]. The Rafaja model allows for the restricted relaxation of the lattice in the plane of the film and takes into account that TiN is most easily deformable in the $\langle 111 \rangle$ direction (see below). This then gives the magnitude of the lateral strain and the strain free lattice constant.

A brief aside on the compliance (Young's modulus, E) of cubic crystals here is required. E is the ratio of the stress to the strain in the direction of a stress. It is found to depend on crystallographic orientation [79] according to:

$$\frac{1}{E} = s_{11} - 2(s_{11} - s_{12} - \frac{1}{2}s_{44})(l_1^2 l_2^2 + l_1^2 l_3^2 + l_2^2 l_3^2)$$

where $\hat{l} = (l_1, l_2, l_3)$ is a unit vector in the direction of the stress and l_1, l_2 and l_3 lie along the (a,b,c) axes of the crystal. For $\langle 100 \rangle$, $\hat{l} = (1, 0, 0)$, and the term in the second parentheses is equal to 0. However, for $\langle 111 \rangle$, $\hat{l} = (\frac{1}{\sqrt{3}}, \frac{1}{\sqrt{3}}, \frac{1}{\sqrt{3}})$ and the term in the second parenteses is equal to 1/3, its maximum value. Thus, the value observed for E will depend on the crystallographic orientation with the $\langle 100 \rangle$ and $\langle 111 \rangle$ directions always the minima or maxima, depending on the sign of $(s_{11} - s_{12} - \frac{1}{2}s_{44})$. For
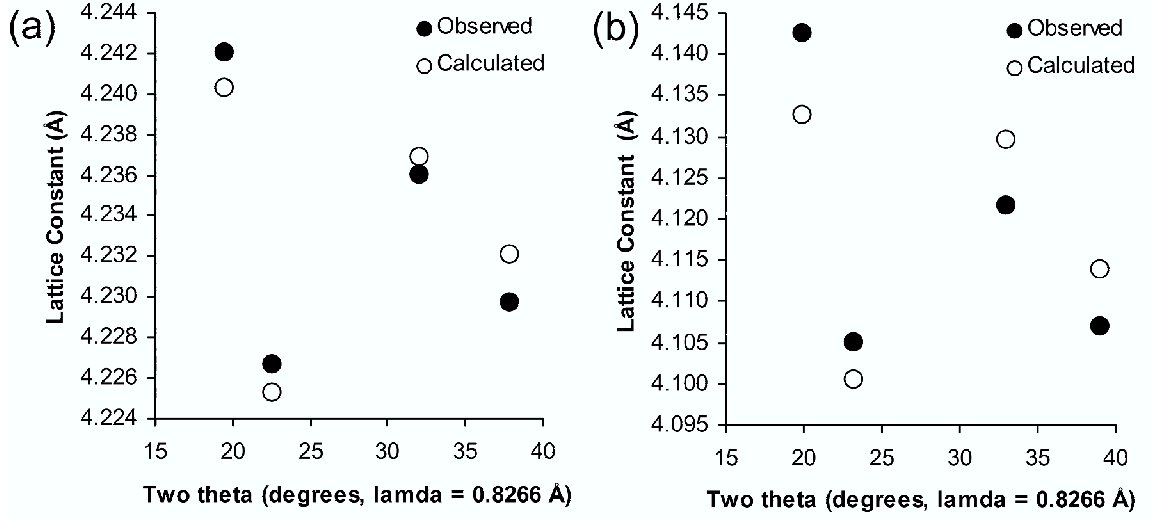
Figure 5.6: Comparison of observed (closed circles) and calculated (open circles) lattice constants for patterns taken at (a) 2.5 GPa and (b) 50.8 GPa.

TiN [80], $s_{11} = 2.17 \times 10^{-3}$ GPa, $s_{12} = -0.38 \times 10^{-3}$ GPa and $s_{44} = 5.95 \times 10^{-3}$ GPa. Thus, the term is negative (-0.425×10^{-3} GPa) and $E_{111} < E_{100}$. For this reason, $\langle 111 \rangle$ is often refered to in the TiN literature as the direction of easy deformation.

The results of the fits to the Rafaja model are presented in Figures 5.6 and 5.7. Figure 5.6 shows the difference between observed and calculated values of the lattice constants as a function of 2θ for two pressures, 2.5 GPa (FIG. 5.6(a)) and 50.8 GPa (FIG. 5.6(b)). The agreement is reasonable and reproduces the trend of (hkl) peaks.

Figure 5.7(a) shows the lateral strain as a function of pressure. Figure 5.7(b) shows the values of the unit cell volume $= \langle (a_0^{strainfree})^3 \rangle$. It can be seen that the strain increases markedly between the first pressure (0.1 GPa) and the second (2.5 GPa). Above this pressure the strain increases more or less monotonically up to the
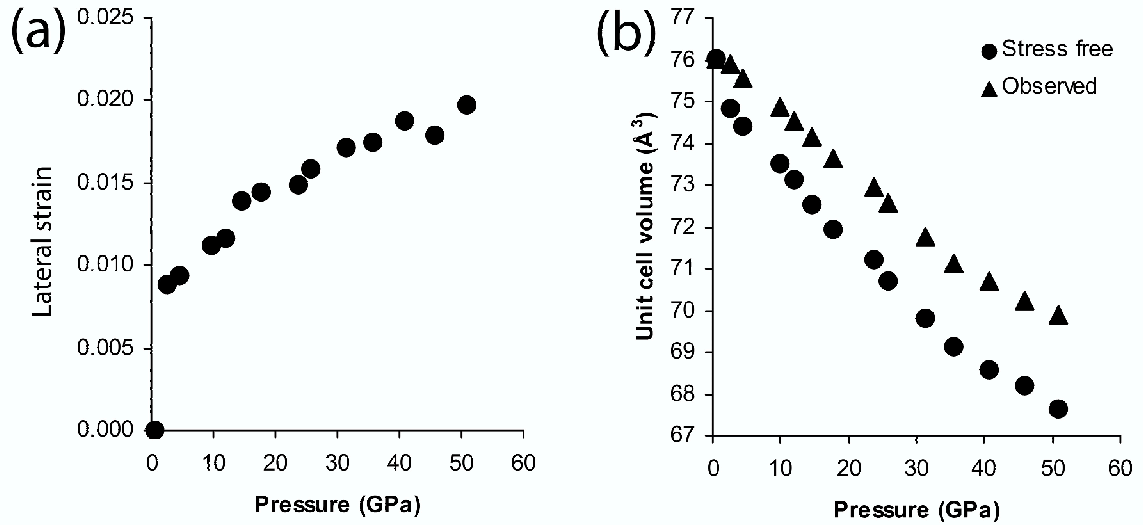
Figure 5.7: Results of model analysis. The lateral strain, Δp, (a), and the zero-strain unit cell volume, (b), are shown as a function of pressure.

highest pressure obtained.

That the model of Rafaja soundly fits the data implies that the model takes into account the major phenomena present in these systems, a strong biaxial strain coupled with deformation strongest in the $\langle 111 \rangle$ direction. The large amount of dispersion between lattice constants from each *hkl* is indicative of the large role played by the easy deformation direction of the material in the amount of bi-axial strain observed. The strain in the films increases with pressure. This implies that the internal strain of the material is converting the hydrostatic pressure in the cell into directional stress within the film.

The tensile strain in these films effects the observed V(P). As can be seen in Figure 5.7(a), the presence of strain has the effect of making the materials less com-

pressible. Rather than all of the PV work going into the reduction of the volume, some is being redirected into producing strain in the film.

This effect may also play a role in the observed hardness of the films. Even though in the indentation case the load is not hydrostatic, the same forces are still present — the strain response of the crystallites is still coupled, and therefore the strain remains tensile.

Isotropic strain

All samples showed increases in peakwidth after quenching to ambient pressure. Table 5.4 shows the results of an analysis using the Warren-Averbach method [81]. The analysis was conducted using the program MudMaster from the U. S. Geological Society [82]. The results show that all samples have an increase in random strain after pressurization. Strain has been observed in these systems before and can generally be relieved by heating to $\sim 600°$C. A sample of HF140502 was recovered in its gasket from the DAC after pressurization and heated to 700°C for 2 hours. X-ray diffracton was then collected on this annealed sample. Figure 5.8 shows the results of this experiment. The diffraction patterns of the post-pressurization and the subsequently annealed samples are nearly identical in peakwidth and intensity.

Samples which have been pressurized to 50 GPa and quenched to ambient pressure demonstrate significantly greater random (isotropic) strain than unpressurized samples. Furthermore, this isotropic strain is resistant to annealing up to 700°C as
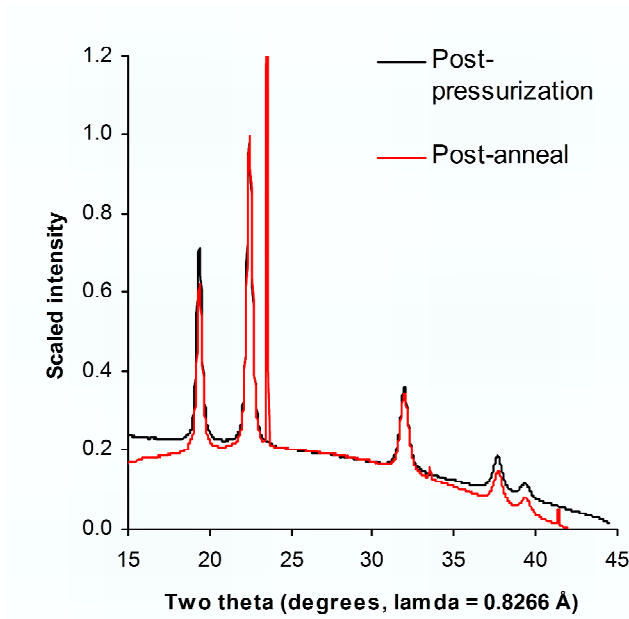
Figure 5.8: X-ray diffraction of HF140502 samples, both post-pressurization and quenched to ambient pressure. The red pattern corresponds to a sample which has been annealed for two hours at 700°C. The near-exact overlap of samples implies that strain has not been relieved by annealing.

Sample	Random strain, pre (%)	Random strain, post (%)
HF140502	3.4	7.7
HF220702	3.3	6.3
HF230702	9.3	10.2
Pro210302	2.9	6.5

Table 5.4: Results of Warren-Averbach analysis of line-broadening for samples before and after pressurization. All samples demonstrate significant increases in strain post-pressurization.

seen in Figure 5.8. That the strain persists to 700°C (973 K or 3.25 times the thermal energy at ambient temperature) makes it seem that some bonds were broken and others formed, implying some type of plastic deformation.

We have shown that the compressibility of the TiN nanocomposite materials is not drastically different from that of bulk TiN. This implies that the nanocomposite materials derive their strength from their structure rather than from an alteration of the interatomic potential. Cold-worked metals show the same sort of hardening as the size of domains within the metal are reduced (Hall-Petch effect). Defects which might otherwise cause failure cannot migrate any further than the edge of the domain in which they form. The same is likely true for TiN nanocomposites. It may be, then, that defects are formed during pressurization and that these defects manifest themselves by producing strain. Although the defects could not migrate, they could cause the movement of atoms within each crystallite. Because the crystallites are bound together by the layers of BN, atomic rearrangement in one grain might create a stress on adjacent grains. This would give rise to isotropic strain as well as the biaxial strain discussed above because of the directional depedence of deformation. This sort of deformation induced strain is supported by the annealing experiment. The strain would be "locked in" by the atomic rearrangement and subsequent formation of new bonds. As such, it could not be easily relieved by annealing, as has been observed.

5.5 Conclusion

We have determined the bulk modulus of a number of TiN based nanocomposite materials and shown them to have values of B_0 very close to or slightly less than the bulk values. This shows that the primary factor causing the observation of ultra-harness is not an enhancement of the bulk modulus. Rather, the hardness is likely due to the resistence to the creation and propogation of defects in the material. This is not to say that the material is in fact defect free. At pressure, a very strong bi-axial strain is present. After pressurization, random, isotropic strain is present which persists even after annealing to 700°C. This indicates that the crystallites undergo some kind of permanant (plastic) deformation at high pressure.

Chapter 6

Observation of an increased transition pressure for aggregated iron oxide nanocrystals

This chapter and the next are the results of two intriguing, though as yet not wholly understood experiments. Although the conclusions drawn are somewhat speculative, they are included for completeness and in the hope that someone will find them interesting and pursue them further.

6.1 Introduction

Nanocrystals have for many years been proposed as a model system for the study of high pressure structural phase transitions [11, 12, 9, 5]. One aspect which makes them model systems is their near perfect crystallographic structure [5, 83]. Another aspect is that each nanocrystal can be viewed as a discrete unit unable to influence the behavior of neighboring nanocrystals. This latter quality is due to their encasement in a surfactant coating and the nanocrystals being dissolved in a pressure medium in which they are soluble. This prevents the nanocrystals from behaving like bulk samples in which grain boundaries and other crystalline defects play a major role in determining the kinetics of the transition.

In spite of the frequency with which this point is cited, the effect of aggregation on the transition pressure of structural transitions has never been systematically studied. Here is presented the results of an experiment conducted on three samples of iron oxide colloidal nanocrystals, each of the same size but in different states of aggregation. The transition pressure is found to depend very strongly on the aggregation state of the material. However, aggregation is found to have the suprising effect of increasing the transition pressure.
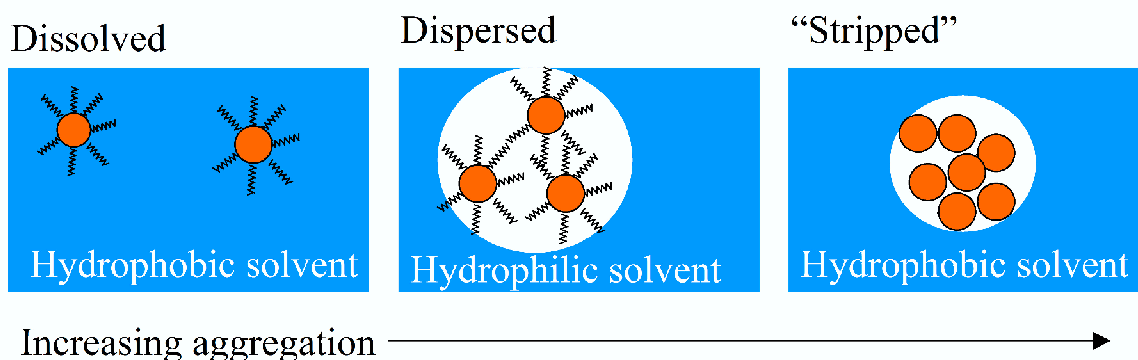
Figure 6.1: Schematic representation of the three samples used in this experiment. In these pictures the inorganic, Fe_2O_3 core is represented by a brown circle, while surfactant molecules are representated by squigley lines.

6.2 Experimental

The details of DAC use and standard sample synthesis can be found in Chapter 2. Details on the collection and analysis of x-ray diffraction data can also be found in Chapter 3.

For this investigation, three different experiments were conducted, shown schematically in Figure 6.1. The first was the standard experiment as discussed in Chapter 4, considered to be dissolved in the pressure medium. The second was with the standard sample but instead of being dissolved in ethylcyclohexane, the sample was dispersed in 4:1 methanol:ethanol, a standard pressure medium in which the nanocrystals are insoluble. This sample is mildly aggregated.

The third and most aggregated sample was synthesized in the standard manner, then refluxed three time in pyridine over the course of five days. This treatment has been previously shown to remove the surfactant coating from CdSe nanocrystals,

replacing the surfactant molecules with pyridine molecules through mass action (even dissolving CdSe nanocrystals in pyridine at room temperature will displace much of the surfactant [10]). After the first reflux, the samples were still somewhat soluble in toluene, indicating that the nanocrystals still retained some of the original hexadecylamine surfactant coating. Following the second reflux step, the nanocrystals were completely insoluble in toluene and formed optically clear solutions in pyridine at room temperature. A third reflux step was conducted to ensure maximal surfactant removal. These "stripped" samples were dispersed as a powder in the DAC in ethylcyclohexane in which they were insoluble.

6.3   Results

The results of the three separate experiments are shown in Figure 6.2. This figure uses the same convention as Figure 4.4, plotting the ratio of the intensities of the γ (311) to the γ (200). The least aggregated sample, the standard dissolved sample used in every other experiment in this work, transforms first at around 30 GPa (a pressure consistent with the size dependence of transition pressures observed in Chapter 4). The next highest transition pressure is observed for the dispersed sample, approximately 35 GPa. Finally, the most aggregated sample transforms at the highest presure, between 42 and 45 GPa, nearly 15 GPa higher than that of the fully dissolved sample.
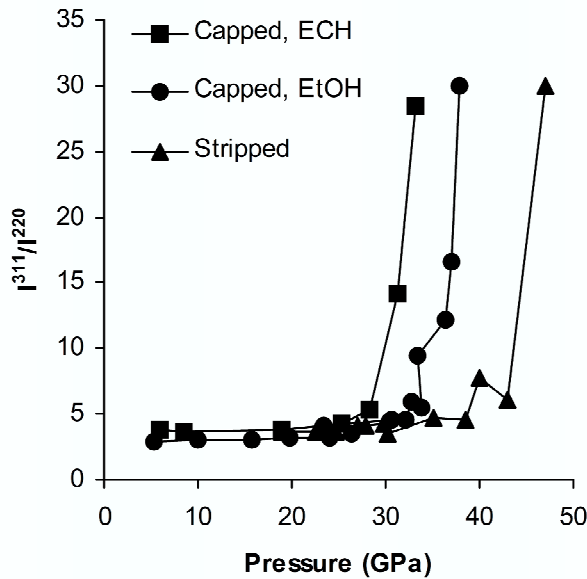
Figure 6.2: The ratio of the intensity of γ (311) to (220). The ratio tracks the progress of the phase transition. The transition pressure is found to depend strongly on the aggregation state.

6.4 Discussion

In bulk systems, the interconnectedness of grains causes high pressure transitions to occur at lower pressures. This is due first to high energy defects present at grain boundaries, and second to the strain created by differential response to pressure between differently oriented grains (see the discussion in Chapter 5 concerning nano-scale domains in TiN thin films). It should be noted, as it was in Chapter 4, however, that the role of defects is more accurately described as decreasing the hysteresis width of the transition. As there is no hysteresis because there is no reverse transition upon decompression, we must assume that the observed transition pressure alone is adequate to make this arguement.

In this experiment, one might expect aggregation to lead to greater strain communication between nanocrystals, and for defects to be generated at the interface of the stripped sample, leading to a depressed transition pressure. Instead, both aggregated samples display an elevated transition pressure, with a greater elevation for the most aggregated sample. This suprising result may be due to a number of effects. First, inter-nanocrystal strain may play a different role for nanocrystals than for bulk. It may be that strain stabilizes the γ with respect to α phase. Distortions in γ may affect the crystal energy to a lesser degree than for α.

An alternate reason may lie in the nature of the transition state between γ and α. If the transition state is of a larger volume than the γ structure, the transition would be said to have a positive activation volume, $\Delta V^{\ddagger}$ [9]. The activation volume is the volumetric analogue of the activation energy. If the activation volume were positive, each nanocrystal (or, more precisely, each transition volume) would have to expand in order to go through the transition. Thus, the addition of pressure, while making the transition more thermodynamically favored, would make the transition more kinetically hindered. This situation would persist until some new pathway becomes low enough in energy to complete the transition. This is the case in spinodal decomposition [68].

A positive activation volume would be consistent with the observed trend for transition pressure with aggregation. The more aggregated samples would have less excess volume, that is, volume not taken up by inorganic material. The organic

material in the system, surfactant and pressure medium, would be mechanically softer and therefore more easily allow the transforming nanocrystal to expand. Also, a positive activation volume is expected if one considers the oxygen as packed hard spheres, an often reasonable assumption for mostly ionic substances like iron oxide. The spheres become smaller in the new alpha stucture, but during the intermidary transition state the crystal stabilization energy necessary to compress them would not be present. The sliding of one layer of hard packed spheres over one another requires a volume expansion of about 12% for a 5.0 nm nanocrystal[1].

A positive activation volume, while reasonable, cannot be proved to be the origin of this effect. The activation volume could be determined independently through a kinetics experiment [9]. The activation volume, $\Delta V^{\ddagger}$, is given by:

$$\frac{\Delta V^{\ddagger}}{k_B T} = -\frac{d \log k}{dt}$$

where k_B is Boltzmann's constant, and $\log k$, is the natural logarithm of the rate constant of the reaction, k. The activation volume has been determined for CdSe nanocrystals as a function of size [9], but in that case a simple optical signature was

---

[1]The difference in volume is calculated in this way. Two closed-packed planes are separated by a distance equal to the height of a tetradedron with sides of length equal to the bondlength, l. Tetrahedrons have height, $h = \frac{\sqrt{6}}{3}l$. The maximum height as planes slide across one another occurs when the atoms of the top plane form an equilateral triangle with two atoms in the lower layer. At this point the distance separating planes is $\frac{\sqrt{3}}{2}l$. The difference is $0.5445l$. The increase in volume is equal to the volume of an ellipsoid with one direction lengthened by $0.5445l$. This percent then is

$$\frac{\frac{4}{3}\pi r^2(r + 0.5445l)}{\frac{4}{3}\pi r^3} = \frac{r + 0.5445l}{r}$$

The O–O bond length in γ is 2.945 Å. For a 5 nm nanocrystal, r = 25 Å. Plugging this value into the above equation gives a percent volume increase of 11.8%.

present due to the conversion of CdSe from the direct-gap wurtzite to the indirect-gap rocksalt structure. Such a signiture expedites the experiment because of the short time scales necessary for a proper kinetics expeirment. In the case of CdSe, visible absorption spectra could be collected in less than 1 second.

In iron oxide, no such simple signiture has been found. David Zaziski in our research group made extensively attempts to use Raman spectroscopy to observe this transition. However, the γ structure showed no strong Raman peaks, and the α structure never showed any strong Raman peaks upon transition (even for long exposures of 20 minutes or more), in spite of the very strong signal peaks in bulk α. This lack of strong peaks may be due to the defective nature of the α structure obtained via pressure (see Chapter 7). Whatever its origin, the lack of an obvious change in the Raman pattern across the transition made phase assignment extremely difficult, and the determination of the kinetics of the transition impossible.

One possible solution to this problem may come with the advent of the new high pressure beamline 12.2 (CALIPSO) at the ALS. Because of the increased brightness provided by that station, exposure times of 30 – 60 s will give XRD patterns with reasonable signal-to-noise ratios. With such time scales a kinetics experiment may become reasonable. Also, because pressure will be able to be controlled remotely while the DAC is in the x-ray hutch, XRD data of the critical moments after the pressure is changed will be available.

6.5 Conclusion

It has been shown that aggregation state of a sample of iron oxide nanocrystals can strongly effect the observed transition pressure of that sample. The greater the degree of aggregation, the higher the observed transition pressure becomes. This is unexpected, as aggregation should lead to defects which would serve as high energy nucleation centers for the transition. This suprising and perhaps rather important result cannot be explained at the present time. However, if the transition were to have a positive activation volume, it may be that aggregation decreases the amount of excess volume available for expansion. This would lead to slower kinetics of the transition at higher pressures, forcing even higher pressures to be reached before a new pathway could become available for the transition. Subsequent kinetics experiments, conducted using higher temporal resolution XRD, could be conducted to determine the validity of this hypothesis.

Chapter 7

Defects in the hexagonal phase of nanocrystalline Fe_2O_3 obtained by pressure and its implications for the mechanism of the $\gamma \rightarrow \alpha$ transition

The work presented in this chapter is part of an ongoing collaboration with Can K. Erdonmez and Simon M. Clark.

7.1   Introduction

Nanocrystals studies have previously demonstrated the ability to provide an excellent picture of the transition state and mechanism of solid-solid structural phase transitions [5, 8]. This fact stems from the fact that nanocrystal studies can exclude the influences of strain and defects in the initial samples. The effects of particle size and shape on the transition, as well as the kinetics of the phase transition, have provided valuable information that has lead to the formulation of mechanisms consistent with this data. In previous chapters, it has been shown that the thermodynamics of the $\gamma \rightarrow \alpha$-$Fe_2O_3$ transition in nanocrystals is strongly influenced by the surface energy of the alpha phase (Chapter 4) and that the kinetics may be governed in part by a positive activation volume (Chapter 6). In this chapter, a more complete picture of the mechanism of the phase transition is gleaned from examination of the x-ray diffraction patterns of the high pressure α phase.

The x-ray diffraction pattern of hexagonal α-Fe_2O_3 has been the subject of much study in particular because of a phenomenon known in the literature as anomalous line broadening [84, 85, 86]. The anomalous broadening of selected x-ray diffraction peaks has been noted for α-Fe_2O_3 derived from goethite (α-Fe_2OOH). Yamaguchi and Takahashi [84] attributed this observation to structural defects in the α-Fe_2O_3, while da Costa et al. [85, 86] attributed it to a tabular shape of the α-Fe_2O_3 crystallites. However, in each case, the integrated intensities of the peaks were equal to those for samples of α-Fe_2O_3 obtained in other ways. In this chapter we report the observation
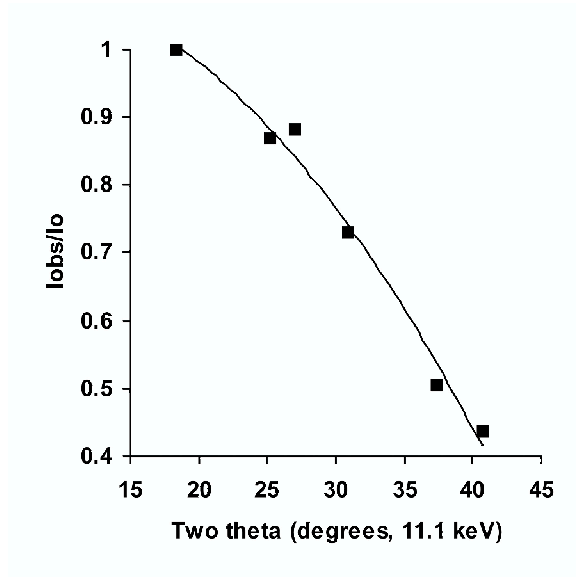
Figure 7.1: Ratio of observed to absolute intensity (I_{obs}/I_0) as a function of 2θ for the ALS 7.3.3 set-up using Al_2O_3 from NIST as a standard. The solid line is the curve of best fit ($I_{obs}/I_0 = -0.0005(2\theta)^2 + 0.0057(2\theta) + 1.0852$), which is used to correct diffraction patterns for the lose of intensity at higher values of 2θ

of anomalous *intensities* and discuss how this observation may help improve the understanding of the nature of the $\gamma \rightarrow \alpha$-$Fe_2O_3$ transition under pressure.

7.2 Experimental

The procedures employed for the collection of high pressure x-ray diffraction data are described in detail in Chapters 2 and 3.

Because this experiment relies in part on accurate intensity data, a careful calibration of the x-ray diffraction intensity was conducted using an α-Al_2O_3 (alumina) standard purchased from the National Institute of Standards and Technology (NIST). The x-ray diffraction intensities of the reflections of this standard are determined by

NIST [87]. A diffraction pattern of the alumina in the DAC was conducted in the standard configuration at ALS 7.3.3 (see Chapter 3 §3.4). The resulting data was fit for peak position and intensity. The intensities, normalized to the (110) peak intensity, were divided by the intensities that should result according to NIST. A calibration curve was thus constructed as a function of diffraction angle. This calibration curve is shown in Figure 7.1. In this way, any intensity losses due to the system can be accounted for by dividing the observed intensity by the value of the calibration curve at a given value of 2θ. These losses are in part due to the additional pathlength for scattered diffraction beams through diamond and air at higher angles and in part to the exact way that Fit2D integrates the two-dimensional data [52].

7.3   Results

The intensity calibrated diffraction pattern of the high pressure α phase for nanocrystals is shown in Figure 7.2. Overlapping the observed diffraction pattern is the theoretical diffraction pattern assuming the corundum structure, space group $R\overline{3}c$ (number 167). The observed diffraction pattern indexes well to the corundum phase. No similarity has been found between this diffraction pattern and that of the ultra-high pressure phase of Fe_2O_3 (see for example Reference [88]).

The intensity for some select peaks is considerably less in the observed pattern than the theoretical ones, while others are equal or nearly equal to what is predicted. In particular, the (110), (113) and (116) peaks are close to their expected values, while
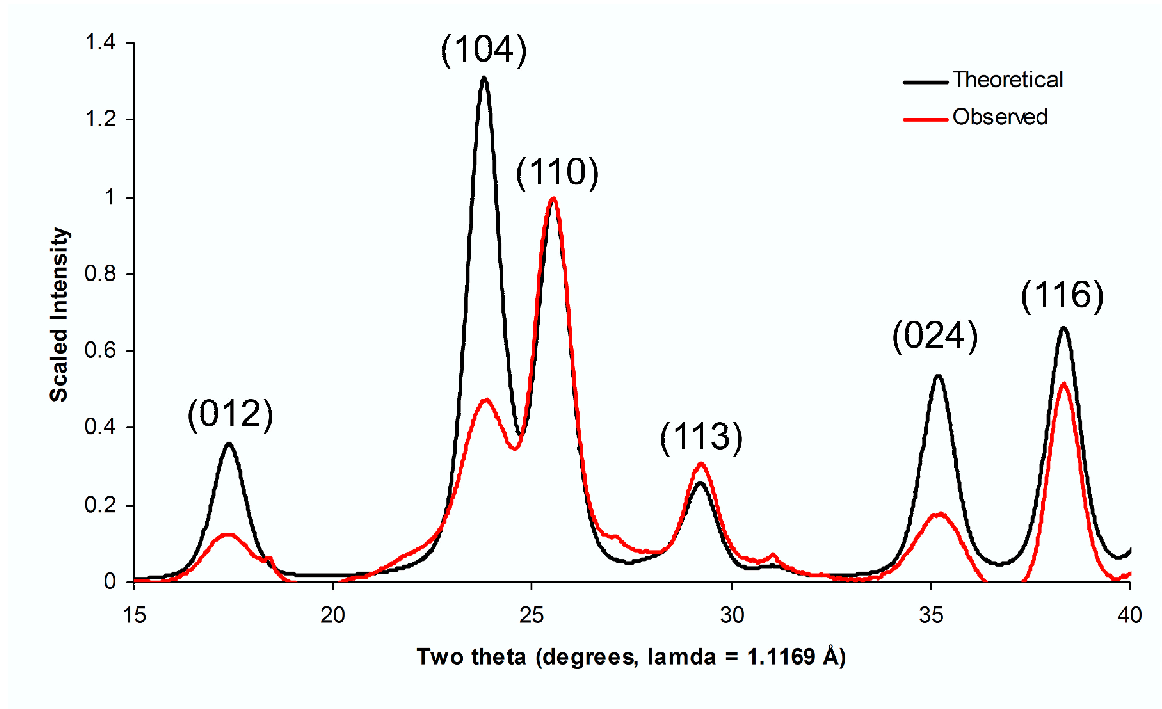
Figure 7.2: The observed (red) and theoretical (black) diffraction patterns of 7.2 nm α-Fe$_2$O$_3$ nanocrystals. The intensity of the observed diffraction pattern has been corrected from the original to account for system losses using the calibration curve in Figure 7.1.

the (012), (104), and (024) peaks are reduced in intensity relative to the theoretical intensity. This decrease in intensity for these selected peaks has been observed in every high pressure α-Fe$_2$O$_3$ sample observed in the course of this work, whether bulk or nanocrystalline in origin.

An analysis of several samples of hexagonal α-Fe$_2$O$_3$ was conducted to investigate if anomalous broadening was present. The results of this analysis are shown in Table 7.1. Included are two sizes of nanocrystals as well as bulk converted by pressure and by gentle application of heat (the latter from reference [86]). The peakwidths of the (104) and (110) peak are given as well as the ratio of intensity between the two peaks.

	$\Delta\theta$ (104)	$\Delta\theta$ (110)	I^{104}/I^{110}
5.7 nm	1.58	1.35	0.73
7.2 nm	1.68	1.15	0.14
bulk (P)	0.88	0.23	0.66
bulk (T)	1.0	0.32	1.9

Table 7.1: Peak width and intensity ratios of α (104) and (110) for nanocrystalline and bulk samples obtained by pressure. The values, from Ref. [86], for the bulk transformation by temperature is shown for comparison. The two nanocrystalline samples are the same samples used in Chapter 4

.

These two peaks were chosen because they are close together, negating the need to make the intensity correction used in Figure 7.2. It can be seen that the peakwidth of the (104) peak is in fact greater than the (110) for all pressure-transformed samples. However, the ratio of intensities, I^{104}/I^{110} is always less than zero, as should not be the case for the corundum structure. The hexagonal structure obtained by temperature shows a very large difference in peakwidths, but also shows a I^{104}/I^{110} ratio of 1.9, closer to that expected.

7.4 Discussion

Several studies of α-Fe_2O_3 obtained by high temperature conversion of goethite have shown certain peaks in the diffraction pattern to be anomalously broadened [84,

85, 86]. As shown in Table 7.1 we observe some broadening of the (104) peak but we also observe an anomalous decrease in intensity. This anomalous intensity is observed to affect only certain peaks listed above. These are the same peaks as those affected by anomalous broadening in thermal studies [84, 85, 86]. These peaks fit the criterion given by Guinier for peak broadening induced by (001) stacking faults in an ideal hexagonally closed pack structure [41]. The criterion arises from the fact that the displacement of (001) planes does not affect the structure factor of certain reflections. The criterion is that (hkl) diffraction peaks which obey

$$\frac{h-k}{3} = 0, 1, 2 \dots$$

will not be broadened by the presence of (001) stacking faults.

However, what is observed is not only broadening but an anomalous decrease in intensity. Furthermore, α-Fe_2O_3 is neither perfectly hexagonal nor monatomic as assumed in the derivation of the above formula. The distortion from this oversimplified picture is shown in Figure 7.3. An ideal lattice is shown with oxygens occupying an hexagonally closed packed (hcp) structure and iron atoms occupying octahedral interstices. Deviations from the ideal are shown by the direction of the arrows away from the ideal position. Oxygen atoms are shifted from ideal within the (001) plane by $0.0275a_0$ in the $\langle 100 \rangle$, $\langle 010 \rangle$ or $\langle 110 \rangle$ directions. Iron atoms are shifted in the $\langle 001 \rangle$ direction by $0.022c_0$. Here a_0 and c_0 are the ambient pressure lattice constants of the unit cell.

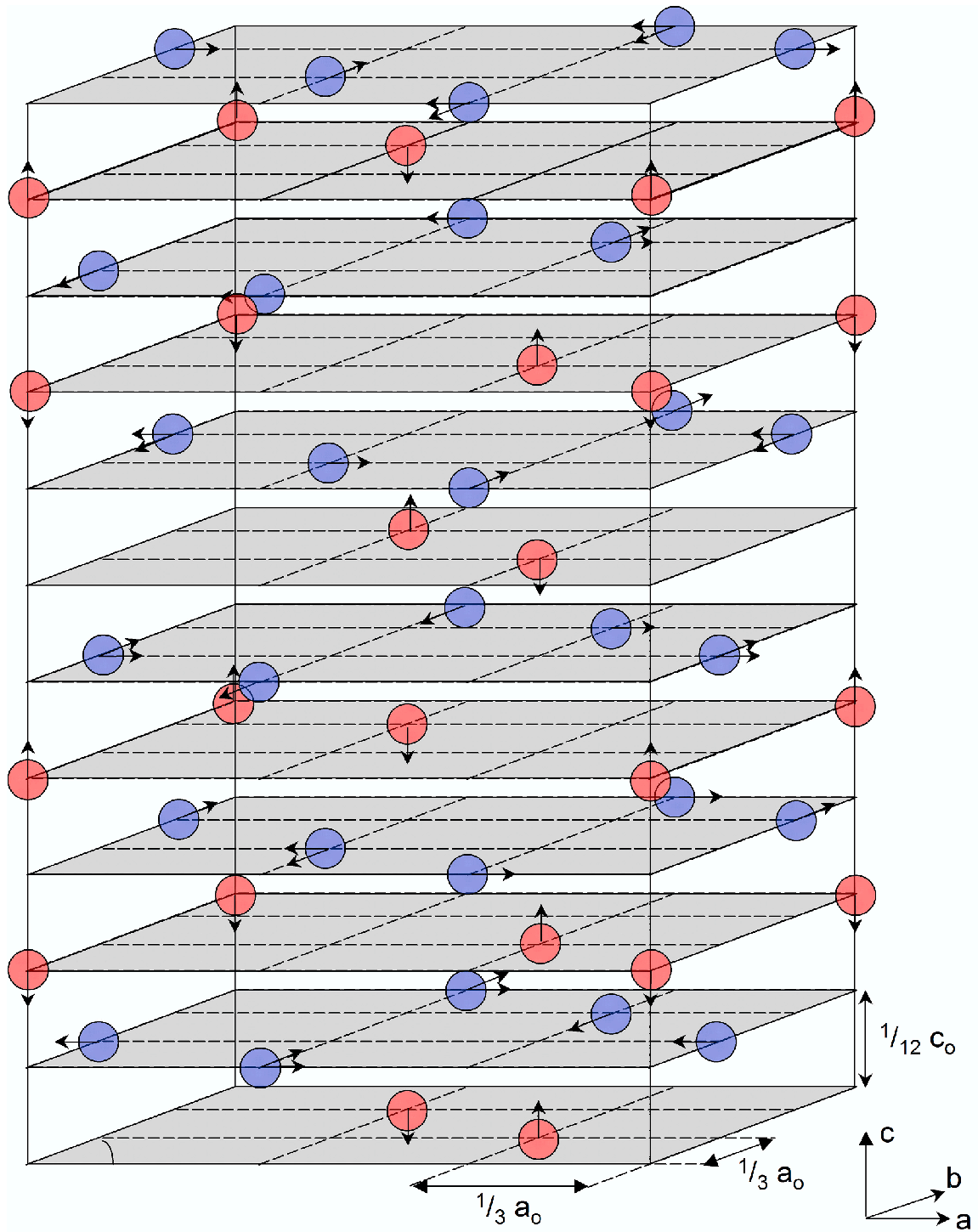Two plausible explanations exist for the observed anomalous intensities. The first,

Figure 7.3: Depiction of the structure of α-Fe$_2$O$_3$ and its deviation from the idealized structure. Red circles are iron atoms, blue are oxygen. Deviations from the ideal hcp oxygen lattice with iron occupying octahedral vacancies are shown by arrows away from those ideal positions.

as has been previously observed for CdSe nanocrystals, is that the shape of the high pressure phase nanocrystal produces more planes of one type [5]. The second is that the high pressure phase contains structural defects. In CdSe, the former explaination was used to account for the small ($<15\%$) selective intensity increase. This same explanation was applied by da Costa et al. [85, 86] to account for anomalous line broadening in α-Fe$_2$O$_3$. In this case very large differences in intensities of multiple peaks are present. Though it cannot be ruled out, it seems unlikely that such large intensity anomalies could be due to a shape change.

If crystalline defects cause the anomalous intensities, it could be either stacking faults, displacement of iron atoms from their equilibrium positions, or a combination of the two. In canonical α-Fe$_2$O$_3$ the iron atoms occupy the distorted octahedral interstices of the oxygen lattice. The peaks displaying decreased intensities are due more to scattering from iron atoms than from oxygen atoms, as has been previously noted [84]. However, attempts in our group using various crystallographic software have been unsuccessful in reproducing the observed intensities by iron displacement alone. Thus stacking faults may play an important role. The effects of stacking faults on even an ideal hexagonal system can be quite complex [89], and can depend on the exact ordering of planes and the contributions from each type of stacking sequence. Work is ongoing by Can Erdonmez to simulate this data as well as to rule out nanocrystalline shape change as the origin of anomalous intensities.

Whether stacking faults or iron atomic displacement, the anomalous intensities

might point to a mechanism in which planes of γ of shift to form α. The shifting of planes might lead to some iron atoms being caught in non-equilibrium positions, or it might lead to a somewhat random sequence of plane stacking. Such a mechanism has been proposed for the γ to α transition before based on the topotactic relationship of the two systems [90]. In cubic structures, atoms are close packed in the (111) direction with a stacking sequence of ABCABC. The shifting of the γ (111) plane in the $\langle 112 \rangle$ direction would lead to the hexagonal (ABAB) plane stacking sequence of α (001) planes (see Figure 7.4). Such plane shifting could lead to a more energetically favorable (compared to γ) but not energetically minimized state. Furthermore, it could result in iron displacement because in the γ structure iron atoms occupy both tetrahedral and octahedral positions. When adjacent planes shift relative to one another, if iron atoms are left behind, the tetrahedral interstices become octahedral and vice-versa as shown in Figure 7.4.

The question remains why this anomalous intensities are only observed for pressure induced and not temperature induced transitions. One way to conceptualize this is by considering the defective, pressure induced structure as a separate phase, α'. In this picture, the α' phase is lower in energy than γ but not quite as low as canonical α. The relative energies, and hence the energetic barriers between phases, is dependent upon pressure. At ambient pressure, the barrier between γ and α is $\sim k_B T$ at 600°C, the temperature above which γ is found to transform into α. If the barrier between α' and α is less than this, α will be observed but the intermediate α' will not. The
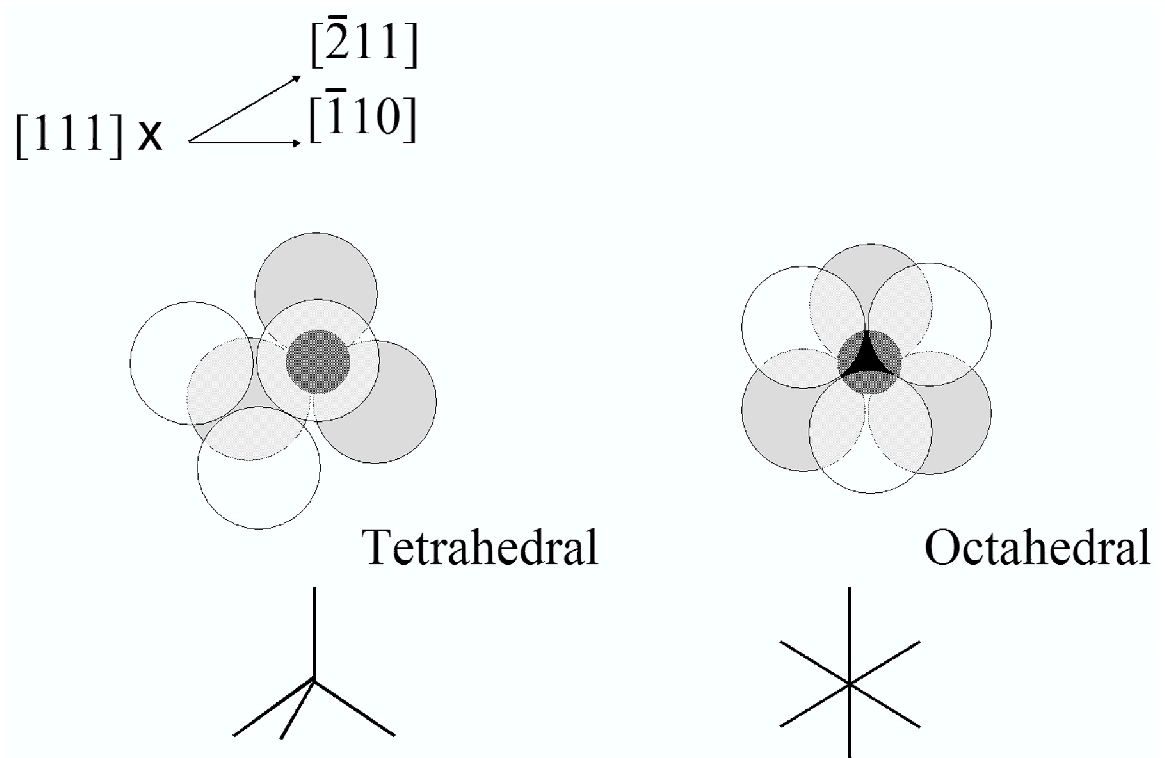
Figure 7.4: Tetrahedral and octahedral vacancies and their switch across the $\gamma \rightarrow \alpha$ transition. The movement of one layer of oxygen atoms over another in the $\langle 211 \rangle$ direction causes the stacking to shift from ABCABC to ABAB, simultaneously flipping tetrahedral and octahedral vacancies
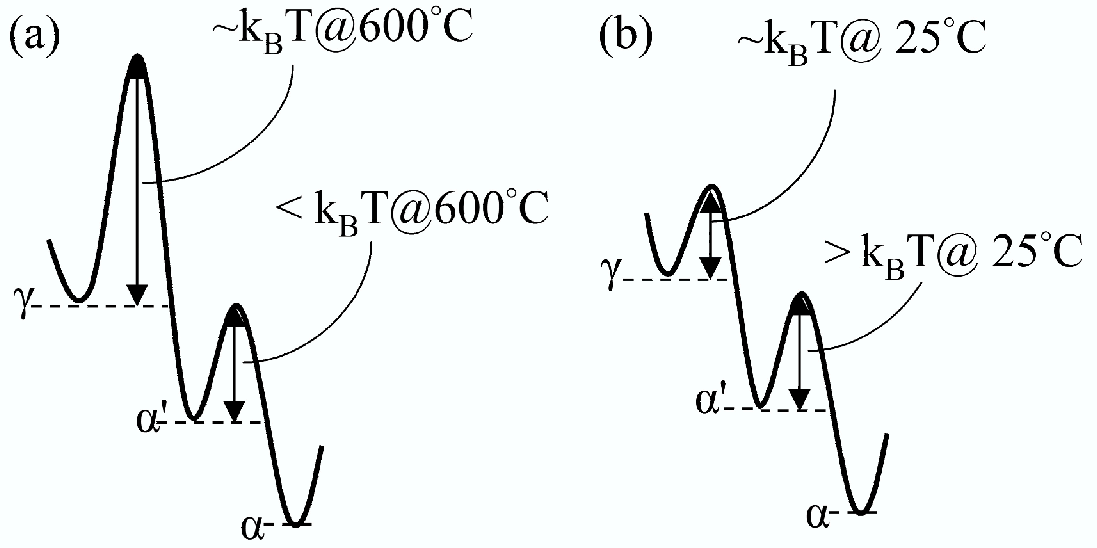
Figure 7.5: Potential energy surface of the phases of Fe_2O_3] at ambient (a) and high pressure (> 30 GPa), (b).

$\alpha' \to \alpha$ transition will be facile.

However, at 30 GPa, the $\gamma \to \alpha$ barrier is much less than at ambient, so that the transition occurs at room temperature. If then the barrier for $\alpha' \to \alpha$ is $> k_BT$ at 25°C, the transition will not proceed beyond the α' phase. This barrier remains greater than k_BT at 25°C even at ambient pressure, leading to the observed stability of α' even after the release of pressure. The potential energy surfaces displayed in Figure 7.5 are then consistent with the observed data.

7.5 Conclusion

The diffraction pattern of pressure induced α-Fe_2O_3 is found to have select peaks of lower intensity than predicted, while others are unaffected. This anomalous intensity

is most likely due to structural defects in the α-Fe_2O_3 phase. These defects give clues as to the nature of the mechanism of the transition for $\gamma \rightarrow \alpha$. This defect phase may be an artifact of a mechanism by which the γ (111) planes shift to form the (001) planes of the hexagonal α phase. In the process, some oxygen planes and iron atoms might not find their equilibrium crystallographic positions, especially at ambient temperatures where the pressure induced transition is observed.

In the future, the experiment might be repeated but at various elevated temperatures to see if the canonical, defect free α phase might be observed. However, for nanocrystals, this may never be the case. Given the higher energy of the nanocrystalline α phase due to surface energy, it may be that the added entropy from defects is necessary to make the phase stable (see Reference [91] for a discussion of the importance of entropy in the thermodynamics of the Fe_2O_3 system). This might explain why the application of pressure is the only means of observing α nanocrystals of sizes less than 25 nm. In thermal studies, the nanocrystals coalesce during the $\gamma \rightarrow \alpha$ transition. This could prove to be a part of the phase diagram, considering size here as a thermodynamic variable, accessible only via pressure and not temperature.

Chapter 8

Conclusion

This work has focused on the behavior of nanocrystalline materials at high pressure, studied by synchrotron x-ray diffraction. Much of this effort has focused on the iron oxide system. That system has demonstrated some of the classic behavior of nanocrystalline studies, in particular a size dependent phase transition pressure. This dependence is due to the higher surface energy of the α phase relative to the γ phase, decreasing the stability of smaller α nanocrystals.

Although the size dependence result has been seen previously in CdSe nanocrystals and explained in much the same way, the iron oxide system has also shown some surprising results that challenge some of the assumptions held about nanocrystalline systems. In iron oxide, aggregation actually causes the transition pressure to increase. This runs contrary to the conventional wisdom that defects decrease the observed transition pressure. The simplest explanation for this result is that for the transition

the activation volume is positive. Due to the decreased free volume in aggregated samples, it becomes very difficult for nanocrsytals to expand as they proceed across the transition. However, effects due to strain cannot be ruled out. Future kinetics experiments may help answer this question.

The stress response in nanocrystals has been found to be complex when nanocrystals are interconnected in another system, that of TiN/BN nanocomposite materials. In this system, strain in one nanocrystal induces strain in those around them. This strain, and its retention even after pressure release and thermal annealing, reveals that the strain is due to atom displacement and the formation of new bonds. In other words, the individual nanocrystals have had defects created within them under pressure. Those defects cannot propagate across nanocrystalline domains, but only manifest themselves as strain apparent in the x-ray diffraction pattern. Taken with the fact that the nanocomposites have the same compressibility as the bulk, this implies that the high strength of these materials comes from their ability to dissipate the work done on them internally and microscopically. The atomic displacement within a nanocrystalline domain does not lead to a macroscopic yielding, but a nanoscopic one which does not decrease the overall material strength — it simply results in a strain set up within the entire thin film.

The displacement of atoms is also important in the iron oxide system. The best current explanation for the anomalous intensities in the high pressure α x-ray diffraction pattern is that the phase is highly defective. These defects are either stacking

faults or displacement of iron atoms. The thermal energy present at room temperature where the high pressure experiments are conducted is insufficient to move the atoms into their equilibrium crystallographic positions. This then implies that the $\gamma \to \alpha$ transition is accomplished by means the sliding of cubic planes to form the hexagonal phase. While this may be the lowest pathway available, it would seem to have a local minimum, the defective phase that is observed at room temperature.

This dissertation distinguishes itself from previous dissertations on this subject in two ways. The first, discussed in Chapter 3, is in the development of a superior means of collecting x-ray diffraction data on nanocrystals at high pressure. The second way is in the choice of samples studied. While many of the ideas used by previous authors to explain the CdSe nanocrystal system have been applied here to the iron oxide system, the iron oxide system has proven itself to be too complex for a simple one-to-one comparison with CdSe. The complexities of its crystal structure, as well as the more complex nature of its bonding (more ionic than covalent) make it a very rich system for the understanding of nanoscale physics. As the aggregation and structural defect experiments show, there are still many open-ended questions remaining with this system which point to the need for further study not only of this system but other metal-oxide systems as well.

Bibliography

[1] A. Paul Alivisatos. *Science*, 271:933–937, 1996.

[2] A. Paul Alivisatos. *J. Phys. Chem.*, 100:13226–13239, 1996.

[3] N. B. Hannay. *Solid State Chemistry*. Prentice Hall, Eaglewood Cliffs, NJ, 1967.

[4] M. S. Shim and P. G. Guyot-Sionnest. *Nature*, 407:981–983, 2000.

[5] J. N. Wickham, A. B. Herhold, and A. P. Alivisatos. *Phys. Rev. Lett.*, 84:923–926, 2000.

[6] David Zaziski, Stephen Prilliman, Erik Scher, Maria Casula, Juanita Wickham, Simon M. Clark, and A. Paul Alivisatos. Critical size for fracture during solid-solid transformations. *submitted to Science*, 2003.

[7] Amy Herhold. *Kinetics of solid-solid phase transitions in semiconductor nanocrystals*. PhD thesis, University of California, Berkeley, 1997.

[8] C.-C. Chen, A.B. Herhold, C. S. Johnson, and A. P. Alivisatos. *Science*, 276:398–401, 1997.

[9] K. Jacobs, D. Zaziski, E. C. Scher, A.B. Herhold, and A. P. Alivisatos. *Science*, 293:1803–1806, 2001.

[10] Janet E. Bowen Katari, Vicki L. Colvin, and A. Paul Alivisatos. *Journal of Physical Chemistry*, 98:4109, 1994.

[11] S. H. Tolbert and A. P. Alivisatos. *Science*, 265:373–376, 1994.

[12] S. H. Tolbert and A. P. Alivisatos. *J. Chem. Phys.*, 102:4642 – 4656, 1995.

[13] S. B. Qadri, J. Yang, B. R. Ratna, E. F. Skelton, and J. Z. Hu. *Appl. Phys. Lett.*, 69:2205–2207, 1996.

[14] J. Z. Jiang, J. S. Olsen, L. Gerward, D. Frost, D. Rubie, and J. Yetronneau. *Europhys. Lett.*, 50:48–53, 2000.

[15] Sarah H. Tolbert, Amy B. Herhold, Louis E. Brus, and A. P. Alivisatos. *Phys. Rev. Lett.*, 76:4384–4387, 1996.

[16] F. Birch. *Phys. Rev.*, 71:809–824, 1947.

[17] B. Chen B, D. Penwell, L. R. Benedetti, R. Jeanloz, and M. B. Kruger. *Phys. Rev. B*, 66:144101, 2002.

[18] J. Z. Jiang, J. S. Olson, L. Gerward, and S. Morup. *Europhys. Lett.*, 44:620–626, 1998.

[19] Varghese Swamy, Leonid S. Dubrovinsky, Natalia A. Dubrovinskaia, Alexandre S. Simionovici, Michael Drakopoulos, Vladimir Dmitriev, and Hans-Peter Weber. *Solid State Commun.*, 125:111–115, 2003.

[20] Zhongwu Wang, S. K. Saxena, V. Pischedda, H. P. Liermann, and C. S. Zha. *Phys. Rev. B.*, 64:012102, 2001.

[21] Jane Bertone, Stephen Prilliman, Simon Clark, A. Paul Alivisatos, and Vicki Colvin. *In preparation*, 2003.

[22] E. Wigner and H. B. Huntington. *J. Chem. Phys.*, 3:764, 1935.

[23] D. J. Dunston and I. L. Spain. *Journal of Physics E: Scientific Instruments*, 22:913–923, 1989.

[24] I. L. Spain and D. J. Dunston. *Journal of Physics E: Scientific Instruments*, 22:923–933, 1989.

[25] M. Eremets. *High Pressure Experimetal Methods*. Oxford University Press, Oxford, 1996.

[26] Russell J. Hemley, editor. *Ultrahigh-Pressure Mineralogy: Physics and Chemistry of the Earth's Deep Interior*, volume 37 of *Reviews in Mineralogy*. Mineralogical Society of America, 1998.

[27] A. L. Ruoff, H. Xia, and Q. Xia. *Rev. Sci. Instrum.*, 63:4342, 1992.

[28] R. Jeanloz and Q. Williams. The core-mantle boundary region. In *Ultrahigh-Pressure Mineralogy: Physics and Chemistry of the Earth's Deep Interior*, chapter 7. Mineralogical Society of America, 1998.

[29] L. R. Benedetti, J. H. Nguyen, W. A. Caldwell, H. J. Liu, M. Kruger, and R. Jeanloz. Dissociation of ch4 at high pressures and temperatures: Diamond formation in giant planet interiors? *Science*, 286:100–102, 1999.

[30] H-K Mao and R. J. Hemley. *Reviews of Modern Physics*, 66:671–692, 1994.

[31] J. Kohanoff. *J. Low Temp. Phys.*, 122:297–311, 2001.

[32] Russell J. Hemley. *Annu. Rev. Phys. Chem.*, 51:763–800, 2000.

[33] A. F. Goncharov, E. Gregoryanz, and R. J. Hemley H. K. Mao, Z. X. Liu. *Phys. Rev. Lett.*, 85:1262–1265, 2000.

[34] Robert M. Hazen, Nabil Boctor, Jay A. Brandes, George D. Cody, Russell J. Hemley, Anurag Sharma, and Hatten S. Yoder Jr. High pressure and the origin of life. *J. Phys. Condens. Matter*, 14:11489–11494, 2002.

[35] Anurag Sharma, James H. Scott, George D. Cody, Marilyn L. Fogel, Robert M. Hazen, Russell J. Hemley, and Wesley T. Huntress. *Science*, 295:1514–1516, 2002.

[36] H. Winick, editor. *Synchrotron Radiation Sources, A Primer*, volume 1 of *Series of Synchrotron Radiation Techniques and Applications*. World Scientific, 1994.

[37] David T. Attwood. *Soft X-Rays and Extreme Ultraviolet Radiation: Principles and Applications.* Cambridge University Press, 1999.

[38] J. D. Jackson. *Classical Electrodynamics, Third Edition.* John Wiley and Sons, New York, 1998.

[39] K. S. Hamad, R. Roth, J. Rockenberger, T. van Buuren, and A. P. Alivisatos. *Phys. Rev. Lett.*, 83:3474–3477, 1999.

[40] Sarah Tolbert. *High pressure studies on nanometer sized clusters : structural, optical, and cooperative properties.* PhD thesis, University of California, Berkeley, 1995.

[41] A. Guinier. *X-ray Diffraction in Crystals, Imprefect Crystals and Amorphous Bodies.* Dover, New York, 1963.

[42] J. Xu, H. K. Mao, and P. M. Bell. *Science*, 232:1404–1406, 1986.

[43] David Adams. Private communication.

[44] Victor K. LaMer and Robert H. Dinegar. *J. Am. Chem. Soc.*, 72:4847–4854, 1950.

[45] J. Rockenberger, E. C. Scher, and A. P. Alivisatos. *J. Am. Chem. Soc.*, 121:11595–11596, 1999.

[46] Deborah Aruguete. Private communication.

[47] Eric Gullikson. X-ray interactions with matter. Data from B.L. Henke, E.M. Gullikson, and J.C. Davis, Atomic Data and Nuclear Data Tables Vol. 54 (no.2), 181-342 (July 1993).

[48] David R. Lide. *CRC Handbook of Physics and Chemistry*, pages 12–221. CRC Press, 84 edition, 2003.

[49] Advanced photon source experimental facilities divison progress report (section 4.3.2). Technical Report ANL/APS/TB-30, Advanced Photon Source, Argonne National Laboratory, 1997.

[50] R. G. Munro. *Journal of the American Ceramic Society*, 80:1919–1928, 1997.

[51] Charles Kittel. *Introduction to Solid State Physics*. John Wiley & Sons, New York, seventh edition, 1996.

[52] A. P Hammersley, S. O. Svensson, M. Hanfland, A. N. Fitch, and D. Husermann. *High Pressure Research*, 14:235–248, 1996.

[53] Stephen G. Prilliman, Simon M. Clark, Can K. Erdonmez, David J. Zaziski, Jacqueline Kwong, and A. Paul Alivisatos. *Solid State Communications*, 2003. (in preparation).

[54] Zhongwu Wang, S. K. Saxena, V. Pischedda, H. P. Liermann, and C. S. Zha. *J. Phys. Condens. Matter*, 13:8317–8323, 2001.

[55] R. M. Cornell and U. Schwertmann. *The Iron Oxides: Structure, Properties, Reactions, Occurrence and Uses.* VCH, New York, 1996.

[56] Yasumasa Goto. *Japn. J. Appl. Phys.*, 12:739–744, 1964.

[57] J. Adnan and W. O'Reilly. *Phys. Earth Planet. Interiors*, 110:43–50, 1999.

[58] V. R. Palkar Pushan Ayyub, Soma Chattopadhyay, and Manu Multani. *Phys. Rev. B*, 51:6135–6138, 1995.

[59] Xisheng Ye, Dongsheng Lin, Zhengkuan Jiao, and Lide Zhang. *J. Phys. D*, 31:2739–2744, 1998.

[60] J. M. McHale, A. Navrotsky, and A. J. Perrotta. *J. Phys. Chem.*, 101:603–613, 1997.

[61] Zhongwu Wang and S. K Saxena. *Solid State Commun.*, 123:195–200, 2002.

[62] J. Burke. *The Kinetics of Phase Transformations in Metals.* Pergamon Press, Oxford, 1965.

[63] J. J. Gilman. *Mat. Sci. Eng. A*, A209:74–81, 1996.

[64] J. Musil. *Surf. Coat. Tech.*, 125:322–330, 2000.

[65] S. Veprek, S. Reiprich, and Li Shizhi. *Appl. Phys. Lett.*, 66:2640–2642, 1995.

[66] Stan Veprek. *J. Vac. Sci. Technol.*, 17:2401–2420, 1999.

[67] William F. Smith. *Principles of Materials Science and Engineering.* McGraw-Hill Companies, New York, 1995.

[68] Hermann Schmalzried. *Chemical Kinetics of Solids.* VCH Publishers, New York, 1995.

[69] Harold P. Klug and Leroy E. Alexander. *X-Ray Diffraction Procedures For Polycrystaline and Amorphous Materials.* John Wiley & Sons, New York, 1954.

[70] S. Veprek, S. Mukherjee, P Karvankova, H.-D. Mannling, J. L. He, J. Xu, J. Prochazka, A. S Argon, A. S. Li, Q. F. Fang, S. Z. Li, M. H. Manghnani, S. Tkachev, P Zinin, S. G. Prilliman, D. J. Zaziski, S. M Clark, A. P Alivisatos, and H. P Strunk. *Mater. Sci. Eng. A*, 2003. (Submitted for publication).

[71] R. J. Angel. *Comparitive Crystal Chemistry*, chapter Equations of state. Number 39 in MSA Reviews in Mineralogy.

[72] R. J. Angel. High pressure powder diffraction. http://ccp14.semo.edu/ccp/web-mirrors/ross-angel/departments/crystal/EOSFIT/esofit4/manual.pdf.

[73] M. H. Manghani, S. Tkachev, P. Zinin, P. Karvanokva, S Veprek, and C. Glorieoux. In *Int. Conf. Metal. Coatings and Thin Films, San Diego 2003*, 2003. (to be published).

[74] L. S. Li, Q. F. Fang andS. Z. Li, and S. Veprek. *Mater. Sci Eng. A*, 2003. (in press).

[75] Stephen G. Prilliman, Can K. Erdonmez, Simon M. Clark, A. Paul Alivisatos, Pavla Karvankova, and Stan Veprek. 2003. (To be submitted for publication).

[76] V. Valvoda. *J. Alloys Comp.*, 219:83, 1995.

[77] R. Kuzel, R Cerny, V. Valvoda, M. Blomberg, M Merisal, and S. Kadlec. *Thin Solid Films*, 268:72, 1995.

[78] D. Rafaja, V. Valvoda, R. Kuzel, A. J. Perry, and J. R. Treglio. Xrd characterization of ion-implanted tin coatings. *Surface and Coatings Technology*, 86-87:302–308, 1996.

[79] J. F. Nye. *Physical properties of crystals, Their representation by tensors and matrices.* Oxford University Press, Oxford, 1985.

[80] R. Kuzel, R. Cerny, V. Valvoda, M. Bloomberg, M. Merisalo, and S. Kadlec. *Thin Solid Films*, 268:72–82, 1995.

[81] B. E. Warren and B. L. Averbach. *Journal of Applied Physics*, 21:595–599, June 1950.

[82] D. D. Eberl, V. A. Drits, J. Srodon, and R. Nuesch. Mudmaster: A program for calculating crystallite size distributions and strain from the sahpes of x-ray diffraction peaks. Open-File Report 96-171, U. S. Geological Society, 1996.

[83] C. B. Murray, D. J. Norris, and M. G. Bawendi. *Journal of the American Chemical Society*, 115:8706–8715, 1993.

[84] T. Yamaguchi and T. Takahashi. *Journal of the American Ceramic Society*, 65(6):C–83, 1982.

[85] G. M. da Costa and M. F. de Jesus Filho. *Journal of Materials Science*, 27:6116–6122, 1992.

[86] K. Nielson J. Z. Jiang, K. Stahl and G. M. da Costa. *Journal of Physics: Condensed Matter*, 12:4893–4898, 2000.

[87] J. P. Cline. Standard reference material 676, certificate of analysis, Alumina internal stanardar for quantitative analysis by x-ray powder diffraction. Technical report, 1992.

[88] J. Straun Olsen, C. S. Cousins, L. Gerwald, H. Jhans, and B. J. Sheldon. *Physica Scripta*, 43:327–330, 1991.

[89] A. I. Ustinov. Effects of planar defects in crystals on the position and profile of power diffraction lines. In Robert L. Snyder, Jaroslav Fiala, and Hans J. Bunge, editors, *Defect and Microstructure Analysis by Diffraction*. Oxford University Press, Oxford, 1999.

[90] Alfred Deschanvres and Bernard Raveau. *Revue de Chinie minerale*, 5:201–251, 1968.

[91] J. M. McHale, A. Auroux, A. J. Perrotta, and A. Navrotsky. *Science*, 277:788 – 791, 1997.

Appendix A

Important notes on diamond cell alignment

These notes are specifically for Diacell membrane driven cells.

All screws are M1.6 and are turned using an 1.5 mm Allen key unless otherwise noted. Alignment should be done using a stereo-zoom microscope with a maximum magnification of at least $100\times$, preferably $150–200\times$, and an apochromatic objective.

The initial alignment of diamonds in the cell is the most dangerous part of the process and the easiest in which to break, chip or scratch one or both diamonds. Extreme care is needed.

Make sure first that the diamonds are properly seated. Push on each on a little with your finger or the wooden end of a cotton swab. If not, retighten the screws holding the diamonds in place. Check to make sure the plate which holds the cylinder

diamond is properly flat against the back of the cylinder. If it is not the diamonds will never reach cylindrical symmetry, i.e., the translational alignment will depend on the distance between the two diamonds.

Bring the diamonds into close proximity slowly while watching from one of the side viewing ports under the alignment microscope. This is tricky to do, especially if you stop and then try to start again. If the piston motion is difficult or not smooth make sure that the piston and cylinder are both clean of any residue, including finger prints. When the diamonds are about a culet's width apart, begin aligning them with the four (or three) set screws on the side of the cylinder. This is a bit tedious at first because you have to keep setting the diamond cell down flat to perform the adjustments (if you do not, the plate holding the cylinder diamond may fall out or become tilted). View the cell from two perpendicular directions each time you make an adjustment.

Once the diamonds are within about 1/2 culet length of being correct, place the cell on its back and look through the diamonds along the optical axis. In transmitted light with the diamonds close together you see the culet of the cylinder diamond illuminated. The alignment is a little easier now because you can see directly where the diamonds are relative to one another. It can be helpful now to use reflected as well as transmitted light. The reflected light picks out the edges of the piston diamond a little better, which is especially useful if the diamonds are not perfectly matched. Continue adjusting the positions until the culets match up quite closely.

Test for cylindrical symmetry by bringing the diamonds apart and then back together in transmitted light. The culet of the cylinder diamond should appear to shrink towards the center. If it severely appears to move to one side when you pull the diamonds apart, re-check that the cylinder diamond is flat in its plate and against the cylinder.

Next come tilt alignment. The tilt of the diamonds is controlled by three screws on the back of the piston which control the tilt of this diamond which is mounted on a hemispherical rocker. Check from the side first to see that the tilt alignment is not severe and adjust and check if necessary. Just make sure that a diamond edge is not going to gouge the culet of the other diamond.

Once the tilt alignment if reasonably close, observe under transmitted light and bring the diamonds into contact. If there is any dirt or grease on the diamonds it will become obvious now and it is necessary to clean the diamonds before proceeding.

You should see rainbow lines form. These are essentially an interference pattern as a result of the diamonds being titled to one another on the scale of the wavelength (or multiples of the wavelength) of the color observed. The goal then is to make the rainbows go away and observe a single steady color change across the entire culet as the diamonds are moved apart. Put an M3 screw in one of the settings on the piston and use an Allen key as a lever to lift the piston out of the cylinder. The rainbow lines will appear to move in one direction. The screws in the direction that they move should be tightened (pneumonic: towards, tighten). However, the same alignment can

be accomplished equally by loosening the opposite screws or, equivalently, the screws from which the lines appear to move away. *Loosing screws should always be your first inclination during the tilt alignment.* The screws strip very easily and during the course of the alignment you will likely have to replace them a number of times (more below). The stripping can be minimized by limiting the number of times you apply a large amount of forward torque to each screw.

On the very first tilt alignment following translational alignment you need not get a perfect tilt alignment. Get it close (to the point where there is a blue line along one side), then place a gasket between the diamonds and screw the cell together very tightly using the combination of a strap wrench and a second wrench, as would be done under normal use. Take the cell apart and check the alignment again, first from the side, then down the optical axis. Often the translational alignment will change significantly, hence the lack of need for a perfect tilt alignment. Iterate until the both translational and tilt alignment is steady.

Then it is necessary to pressure condition the diamond cell and the alignment. Again, place a gasket between the diamonds, tighten as you would for regular use, then apply gas load incrementally, starting at 10 bar, then in 10 bar increments up. After each application of load, check the alignment as above and adjust. If the alignment requires serious adjustment, start over at 10 bar. Eventually the alignment will become stable. The translational alignment tends to become stable first, but will occasionally change significantly at high (> 50 bar) gas loads suddenly after being

stable for the previous two or three loads.

Because of the repetitive nature of this task, it is necessary to check yourself often along the way. It is good practice, for example, to optically check before tightening the cell to ensure that a gasket is between the diamonds.

The alignment has some tolerance that can be allowed. In general, 1% is sufficiently good for going to 60 GPa with 300 mm culet diamonds. For tilt this means 300 nm across 300 μm, which means that one line of blue would be visible at the edge of the diamonds when in contact.